UNIVERSITÀ
DEGLI STUDI
DI PADOVA

Università degli Studi di Padova

Dipartimento di
INGEGNERIA INDUSTRIALE

CORSO DI DOTTORATO DI RICERCA IN:
INGEGNERIA DELL'ENERGIA
CICLO XXIX

EVALUATION OF THERMAL HEAT FLUXES IN BUILDINGS WITH INFRARED THERMOGRAPHY

Coordinatore: Ch.mo Prof. Paolo Colombo
Supervisore: Ch.mo Prof. Michele De Carli
Co-Supervisore: Dott. Paolo Bison

Dottorando : Giovanni Ferrarini

INDEX

1 INTRODUCTION

Buildings are the place where people spend the vast majority of their time [1] and are accounting for the 40% of global energy consumption [2]. The research is therefore constantly trying to improve the thermal comfort for people while decreasing the required energy to obtain it. To succeed in this challenge, it is firstly necessary to have a deep knowledge of the energy transfer mechanisms between the building and the environment. This basic knowledge must be applied to the individual study of each single building, as multiple variables make each edifice unique.

The following work, after an introduction part, describes traditional and innovative thermographic methods and procedures aimed to determine the heat exchanges between the building and the surrounding environment. The proposed techniques are then applied to different case studies, both in laboratory and on-site, and also compared and integrated with analytical and numerical modeling.

The goal is extending the use of thermographic analysis during building surveys, overcoming practical limitations and improving the completeness and accuracy of building investigations.

The initial part of this work introduces the concept of building and stresses the importance of its energy performance, as current laws and regulations are getting more and more strict and challenging.

In the following third chapter infrared thermography is presented as a powerful investigation technique for non-destructive testing and evaluation.

The fourth chapter describes the post-processing phase of infrared image sequences. After the description of the most common methods, new algorithms based on the Partial Least Squares approach are introduced. The techniques are applied to the study of damaged frescoes, both in laboratory and inside an ancient church.

In the fifth chapter, several case studies of building surveys are described in details. For each investigation the traditional techniques were accompanied by innovative thermographic systems (aIRview and IRpano) that extended the measured parameters and improved the speed and accuracy of the survey procedure. A special focus is dedicated to the individuation and quantification of moisture inside the structures, always applying infrared based measuring techniques.

The following sixth chapter continues the previous analyses, introducing new methods for the laboratory and on-site evaluation of the main characteristics of the building envelope such as thermal bridges, thermal transmittance, dynamic behavior of the walls. The investigation is extended also to HVAC systems, with the measurement of radiant ceiling systems performance.

The seventh chapter describes the integration of thermographic methods with numerical modeling and also proposes some design tools both for the building envelope and for the radiant systems.

The final chapter summarizes and discusses the results obtained in the previous sections and provides a preview on the future works.

Several sections of this work are based on scientific articles published on national and international journals and conference proceedings, as described at the beginning of each chapter.

1 INTRODUZIONE

Gli edifici sono il luogo in cui le persone trascorrono la maggior parte della giornata [1] e sono responsabili del 40% del consumo energetico globale [2]. La ricerca è quindi costantemente indirizzata al miglioramento delle condizioni di benessere termico per le persone cercando al tempo stesso di diminuire l'energia necessaria per ottenerlo. Per vincere questa sfida, è in primo luogo necessaria una profonda conoscenza dei meccanismi di scambio energetico tra l'edificio e l'ambiente Questa conoscenza di base deve essere poi applicata allo studio individuale di ogni edificio, poiché molteplici variabili tendono a far diventare ogni edificio unico.

Il presente lavoro, dopo una parte introduttiva, descrive procedure e metodi termografici tradizionali ed innovativi mirati a determinare gli scambi termici tra l'edificio e l'ambiente circostante. Le tecniche proposte sono successivamente applicate a diversi casi studio, sia in laboratorio che in situ, e confrontate e integrate con modelli numerici e analitici.

L'obiettivo è estendere l'uso del metodo di analisi termografico durante l'ispezione degli edifici, superando limitazioni pratiche e migliorando la completezza e accuratezza delle indagini.

La parte iniziale di questo lavoro introduce il concetto di edificio ed evidenzia l'importanza della sua prestazione energetica, visto che le attuali leggi e normative sono sempre più stringenti.

Nel successivo terzo capitolo la termografia infrarossa è presentata come una valida tecnica di indagine per la diagnostica non distruttiva.

Il quarto capitolo descriva la fase di elaborazione di sequenze di immagini termiche. Dopo la descrizione dei metodi più comuni vengono introdotti nuovi algoritmi basati sull'approccio Partial Least Squares. Le tecniche sono applicate allo studio di affreschi che mostrano segni di degrado, sia in laboratorio che in situ in una antica chiesa.

Nel quinto capitolo sono descritti in dettaglio diversi casi studio di indagine su edifici reali. Per ogni indagine le tecniche tradizionali sono accompagnate da sistemi termografici innovativi (aIRview e IRpano) che estendono i parametri misurabili e migliorano la velocità e accuratezza delle procedure di ispezione. Una speciale

attenzione è dedicata all'individuazione e quantificazione dell'umidità all'interno delle strutture murarie, sempre applicando metodi basati sulla termografia infrarossa.

Il seguente sesto capitolo prosegue l'analisi precedente, introducendo nuovi metodi per la valutazione in laboratorio e in situ delle caratteristiche principali dell'involucro termico quali ponti termici, trasmittanza, risposta dinamica delle murature. L'indagine è inoltre estesa ai sistemi di climatizzazione, con la misura delle prestazioni di sistemi radianti a soffitto.

Il settimo capitolo descrive l'integrazione dei metodi termografici con la modellazione numerica e propone inoltre alcuni strumenti per lo studio sia dell'involucro edilizio che dei sistemi radianti.

Il capitolo finale riassume e discute i risultati ottenuti nelle sezioni precedenti e fornisce un'anticipazione dei lavori futuri.

Diverse sezioni di questo lavoro sono basate su articoli scientifici pubblicati su riviste ed atti di convegno nazionali ed internazionali, come evidenziato all'inizio di ogni capitolo.

1.1 References

[1] N.E. Klepeis, W.C. Nelson, W.R. Ott, J.P. Robinson, A.M. Tsang, P. Switzer, J.V. Behar, S.C. Hern, W.H. Engelmann, The National Human Activity Pattern Survey (NHAPS): a resource for assessing exposure to environmental pollutants, Journal of Exposure Analysis and Environmental Epidemiology. 11 (2001) 231–252. doi:10.1038/sj.jea.7500165.

[2] European Commission, COM/2016/051 final - An EU Strategy on Heating and Cooling, (2016).

2 Buildings: a potential source of energy savings

Buildings are a cornerstone of human civilization, and since ancient times codes are regulating building construction and use and sanctioning builders in case of misconducts [1]. The term building (Italiano *Edificio*; Deutsch *Gebäude*; Français *Bâtiment*) and its synonyms construction and edifice generically indicate the concept of creating an entity that can give home and shelter. Therefore an extremely wide range of entities fall into the definition of buildings, while being extremely different among each other under different standpoints such as structure, scope, occupation, size, value. The European Union, inside its 2010/31/EU directive, defines a building as a roofed construction having walls, for which energy is used to condition the indoor climate [2]. A brief list of building, organized in categories, is presented in the following Table 2.1 to further underline the vast number of constructions that fall under the definition of building.

Building category	**Example**
Agricultural	Farmhouse Shed
Commercial	Hotel Shopping mall
Educational	School Museum
Government	Parliament Police station
Industrial	Factory Power plant
Military	Arsenal Barracks
Parking and storage	Garage Warehouse

Religious	Church Temple
Residential	House Condominium
Recreational	Theater Theme park
Sport	Gym Stadium
Transport	Airport Railway station

Table 2.1: List of building categories with examples of typical constructions

The Italian law (D.P.R. 412/93) organizes buildings into eight categories: residential buildings, office buildings, hospitals, recreational or religious buildings, commercial buildings, sport buildings, educational buildings, industrial buildings.

Another noteworthy category, present in almost every national regulation, is listed buildings: edifices of special interest, usually from an architectural or historical point of view, that belong to cultural heritage and are preserved with special care. Typical parameters to define listed buildings are age and rarity, aesthetic merits, selectivity, national interest [3].

The broad range of structure that falls under the building definition implies that also several different performance criteria are expected to meet, such as guaranteeing the comfort of people, ensuring the conservation of goods, securing the assets that are stored. This is an intrinsically multidisciplinary work, involving experts in filed such as structures, architecture, energy, psychology, planning. However, in recent years the energy saving issue was going under the spotlight, due to its impact on the entire society.

The research is more and more interested in the analysis of buildings, especially from an energetic standpoint. Figure 2.1 shows the data of the 8 main journals primarily dedicated to this field (Advances in Building Energy Research, Building Research and Information, Building Simulation, Building and Environment, Construction and Building

Materials, Energy and Buildings, Journal of Building Performance Simulation, Journal of Building Physics) according to SCOPUS database and the SCImago Journal Rank. The increasing trend of these publications is notable and steeper than the general increasing trend of scientific production.

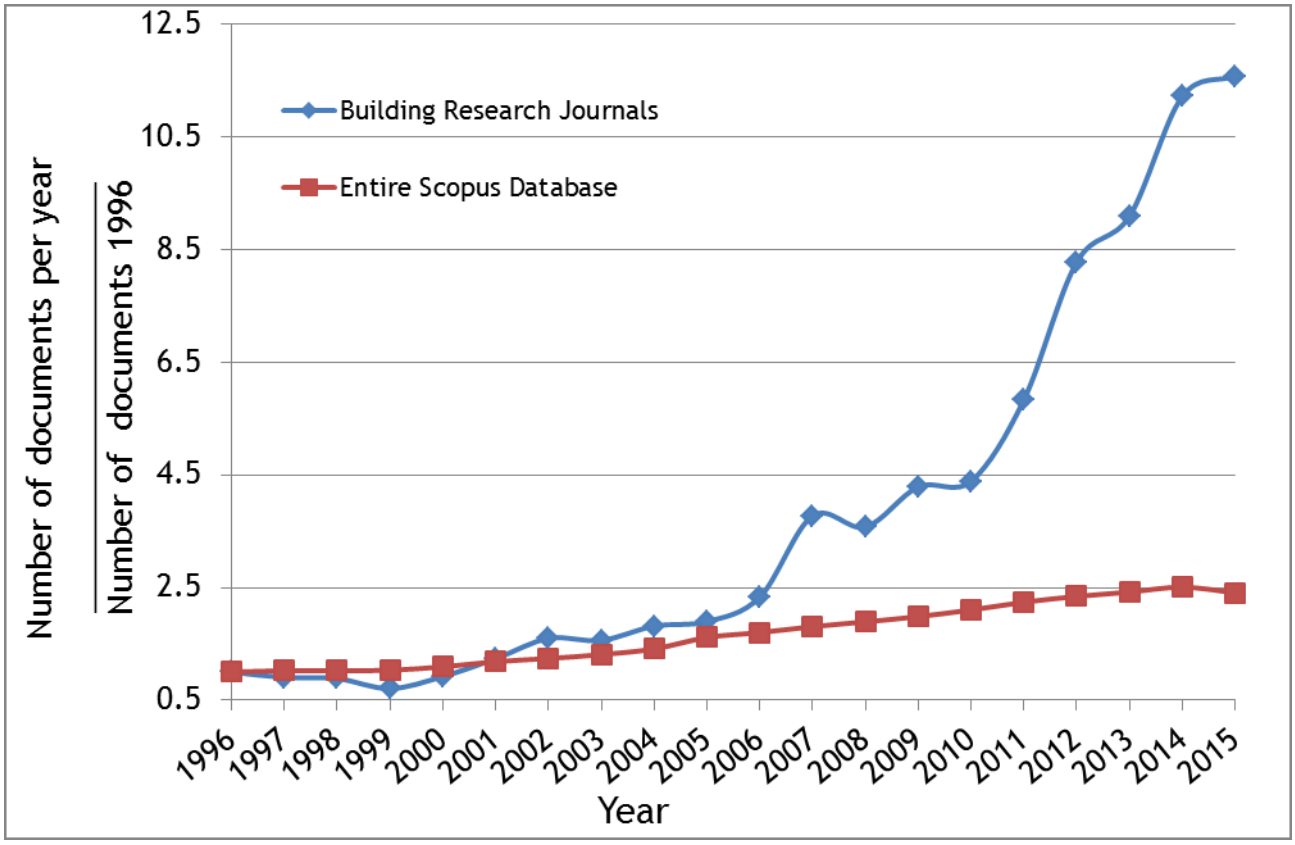

Figure 2.1: Comparison of trends in scientific production over the last 20 years according to SCOPUS database showing the contribute of the 8 main building research journals (blue line) against the overall scientific works of the database (red line). Both trends are calculated by the ratio of number of documents per year over the number of documents of the baseline year (1996). The production increase in building research, especially in the last ten years, is remarkable.

2.1 The need for energy savings

A functioning building requires a certain amount of energy, depending on several parameters. The energy performance of a building is defined as “the calculated or measured amount of energy needed to meet the energy demand associated with a typical use of the building, which includes, inter alia, energy used for heating, cooling, ventilation, hot water and lighting” [2]. To improve the energy performance of a building, the first element that is usually analyzed is the building envelope, that means the integrated elements of a building which separate its interior from the outdoor environment [2]. A well designed building envelope could reduce dramatically the

heating and cooling demand, but the overall goal should be the correct integration between the building envelope and the HVAC systems. This is stressed by the policymakers, that provide several regulations on the theme of energy efficiency in buildings.

2.1.1 Italian regulations: current framework

The current legislative Italian framework is mainly derived from European directives. The most important step in recent years was the 192/2005 regulation [4] that implemented the European Directive 2002/91/EC (Energy Performance Building Directive) [5] regarding the energy efficiency of buildings. This regulation established the Energy Performance Certificate and compliance targets for energy demand and envelope performance for new buildings. It has been modified and corrected by the 311/2006 [6] which established stricter compliance targets for building envelope performances and the Energy Performance Certificate obligation for real estate trade. Other modifications were introduced by means of the 59/2009 decree [7]. The ministerial implementation law 26/06/2009 [8] introduced the Energy Performance Certificate guidelines. The 63/2013 law [9], amended by the 90/2013 law [10], regards the implementation of the European Directive 2010/31/EU (EPBD recast) [2]. This law established that all new public buildings, which will be constructed after 01/01/2019, must be "Nearly Zero Energy Buildings" (NZEB), that is they must have very little energy consumption, which have to be mainly covered by renewable energy sources. Regarding the private buildings, they must be NZEB if made after 01/01/2021. Furthermore, 90/2013 law established the Energy Performance Certificate obligation for real estate rental. In 2015, the 26/06/2015 decree [11] introduced new regulations on energy performance of the buildings. Such law implemented the 90/2013 and eventually gave the Italian definition of NZEB. In 2016, the UNI 10349 standard [12] that provides the climatic data for each Italian city has been updated.

2.1.2 Italian regulations: compliance targets

The Italian land has been divided into several climatic zones according to the values of "degrees day" (*dd*), which is defined by the following formula:

$$dd = \sum_{i=1}^{n} (T_I - T_{Oi}) \tag{2.1}$$

where:

- T_I is the conventional inside temperature (usually 20°C);

- T_{Oi} is the outside mean daily temperature;

- n is the number of the days of the conventional period of heating.

In the following figure the map of the climatic zones in which Italy is divided is shown.

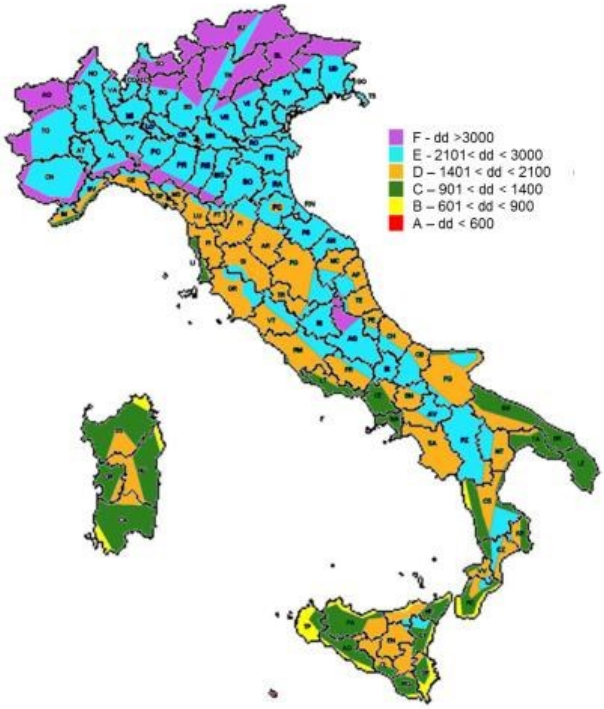

Figure 1: Map of the climatic zones in Italy from A to F

The 26/06/2015 law considers different kind of building refurbishment, which have to reach different compliance targets.

- first level refurbishment: retrofit of more than 50% building envelope and HVAC system;

- second level refurbishment: retrofit of more than 25% building envelope and/or HVAC system;

- third level refurbishment, retrofit of less than 25% building envelope or HVAC system.

The 26/06/2015 law created the concept of reference building, which is a building with the same layout, position, orientation, use, boundary conditions as the real building with envelope thermal parameters shown in the next Table 2.2.

Thermal transmittance of the reference building envelope elements [W/m^{2}K]								
Climate Zone	Walls		Roofs		Floors		Windows	
	Before 31/12/2020 (31/12/2018 for public buildings)	After 01/01/2021 (01/01/2019 for public buildings)	Before 31/12/2020 (31/12/2018 for public buildings)	After 01/01/2021 (01/01/2019 for public buildings)	Before 31/12/2020 (31/12/2018 for public buildings)	After 01/01/2021 (01/01/2019 for public buildings)	Before 31/12/2020 (31/12/2018 for public buildings)	After 01/01/2021 (01/01/2019 for public buildings)
A-B	0.45	0.43	0.38	0.35	0.46	0.44	3.20	3.00
C	0.38	0.34	0.36	0.33	0.40	0.38	2.40	2.20
D	0.34	0.29	0.30	0.26	0.32	0.29	2.00	1.80
E	0.30	0.26	0.25	0.22	0.30	0.26	1.80	1.40
F	0.28	0.24	0.23	0.20	0.28	0.24	1.50	1.10

Table 2.2: Limit values for the thermal transmittance of the reference building [11].

The reference building HVAC system is the same as the real building, with efficiencies shown in the following Table 2.3.

Distribution	η_u		
	Heating	Cooling	Hot water
Water distribution	0.81	0.81	0.7
Air distribution	0.83	0.83	-
Mixed air-water distribution	0.82	0.82	-
$\eta_u = \eta_d * \eta_r * \eta_e$ where η_d is the distribution efficiency, η_r is the control efficiency, and η_e is the emission efficiency.			

Heat production system	η_g (generation efficiency)		
	Heating	Cooling	Hot water
Liquid fuel boiler	0.82	-	0.80
Gas fuel boiler	0.95	-	0.85
Solid fuel boiler	0.72	-	0.70
Solid biomass boiler	0.72	-	0.65
Liquid biomass boiler	0.82	-	0.75
Electric compression heat pump	3.00	3.00	2.50
Absorption heat pump	1.20	1.20	
CHP (Combined Heat and Power) plant	0.60		0.60
District heating	0.97	-	-
District cooling	-	0.97	-

Table 2.3: Distribution (upper table) and generation (lower table) efficiencies of the thermal system of the reference building [11].

In the cases of new buildings or first level refurbishments of buildings, the energy demand (expressed in kWh m^{-2}) must be calculated separately for each use, e.g. heating, cooling, ventilation (if present), and lighting. Moreover the global energy demand, as the sum of all contributions, must be calculated. Heating, cooling and global energy demand (respectively *EPH*, *EPC*, EP_{gl}) of the building must be lower than the values calculated for the reference building.

26/06/2015 law introduces two new parameters to assess the performance of the building envelope both in heating and in cooling: H'_T and A_{sol}/A_{tot}.

H'_T is a weighted average of the thermal transmittance of the building envelope element and is expressed by the following equation:

$$H'_T = \frac{\sum_k U_k A_k}{\sum_k A_k} \tag{2.2}$$

where U_k is the thermal transmittance of each building envelope element and A_k is its area.

A_{sol} is a parameter that depends on the area of the windows, the presence of shading systems, the solar radiation. It should be as low as possible in such a way to decrease the cooling demand of the building. A_{tot} is the floor area of the building.

In the cases of new buildings or first level refurbishments of buildings, H'_T and A_{sol}/A_{tot} must be lower than the value shown in the following Table 2.4.

H'_T					
Form factor (S/V)	Climate zone				
	A-B	C	D	E	F
S/V≥0.7	0.58	0.55	0.53	0.5	0.48
0.7>S/V≥0.4	0.63	0.6	0.58	0.55	0.53
S/V<0.4	0.6	0.8	0.8	0.75	0.7
Form factor S/V is the ratio between the surface in contact with the external environment and the volume of the building.					

Building category	A_{sol}/A_{tot}
Residential building	≤ 0.03
Other buildings	≤ 0.04
The limit values of A_{sol}/A_{tot} are valid for all the climate zones.	

Table 2.4: Limit values for the building envelope in case of a first level refurbishment [11].

In the case of second level refurbishments, the building must respect the value of H'_T shown above and the thermal transmittance of the envelope elements must be lower than the values shown in the following Table 2.5.

Thermal transmittance limits for building envelope elements [W/m^{2}K]								
Climate Zone	Walls		Roofs		Floors		Windows	
	Before 31/12/2020 (31/12/2018 for public buildings)	After 01/01/2021 (01/01/2019 for public buildings)	Before 31/12/2020 (31/12/2018 for public buildings)	After 01/01/2021 (01/01/2019 for public buildings)	Before 31/12/2020 (31/12/2018 for public buildings)	After 01/01/2021 (01/01/2019 for public buildings)	Before 31/12/2020 (31/12/2018 for public buildings)	After 01/01/2021 (01/01/2019 for public buildings)
A-B	0.45	0.40	0.34	0.32	0.48	0.42	3.20	3.00
C	0.40	0.36	0.34	0.32	0.42	0.38	2.40	2.00
D	0.36	0.32	0.28	0.26	0.36	0.32	2.10	1.80
E	0.30	0.28	0.26	0.24	0.31	0.29	1.90	1.40
F	0.28	0.26	0.24	0.22	0.30	0.28	1.70	1.00

Table 2.5: Limit values for the building envelope in case of a second level refurbishment [11].

In the case of third level refurbishments, the building envelope elements must be lower than the values shown above. The definition of periodic thermal transmittance, as the predisposition to phase shift and mitigate the heat transfer by an opaque surface, is introduced: this parameter must be calculated according to the standard UNI EN ISO 13786 [13]. The maximum allowed values of periodic thermal transmittance are:

- 0.1 W m^{-2} K^{-1} for the walls;

- 0.18 W m^{-2} K^{-1} for the roofs.

Furthermore, in climate zone A,B,C,D, E or where the monthly average of the solar irradiance is equal or greater than 290 W m^{-2}, the superficial mass of walls and ceilings must be greater than 230 Kg m^{-2}.

2.2 References

[1] The code of Hammurabi King of Babylon, 18th century BC. http://avalon.law.yale.edu/ancient/hamframe.asp.

[2] Official Journal of the European Union, Directive 2010/31/EU of the European Parliament and of the Council of 19 May 2010 on the energy performance of buildings, 2010.

[3] UK Department for Culture, Media and Sport, Principles of Selection for Listing Buildings, (2010).

[4] Decreto Legislativo 19 agosto 2005, n. 192 Attuazione della direttiva 2002/91/CE relativa al rendimento energetico nell'edilizia, 2005.

[5] Directive 2002/91/EC of the European Parliament and of the Council of 16 December 2002 on the energy performance of buildings, 2002.

[6] Decreto legislativo 29 dicembre 2006, n. 311 Disposizioni correttive ed integrative al decreto legislativo n. 192 del 2005, recante attuazione della direttiva 2002/91/CE, relativa al rendimento energetico nell'edilizia, 2006.

[7] Decreto del Presidente della Repubblica 2 aprile 2009, n. 59 Regolamento di attuazione dell'articolo 4, comma 1, lettere a) e b), del decreto legislativo 19agosto 2005, n. 192, concernente attuazione della direttiva 2002/91/CE sul rendimento energetico in edilizia, 2009.

[8] Decreto Ministeriale 26/6/2009 – Ministero dello Sviluppo Economico Linee guida nazionali per la certificazione energetica degli edifici, 2009.
[9] D.L. 4 giugno 2013, n. 63 Disposizioni urgenti per il recepimento della Direttiva 2010/31/UE del Parlamento europeo e del Consiglio del 19 maggio 2010, 2013.
[10] LEGGE 3 agosto 2013, n. 90 Conversione, con modificazioni, del decreto-legge 4 giugno 2013, n. 63, 2013.
[11] Decreto interministeriale 26 giugno 2015 - Applicazione delle metodologie di calcolo delle prestazioni energetiche e definizione delle prescrizioni e dei requisiti minimi degli edifici, 2015.
[12] UNI 10349:2016 Riscaldamento e raffrescamento degli edifici - Dati climatici, 2016.
[13] ISO 13786:2007, Thermal performance of building components -- Dynamic thermal characteristics -- Calculation methods, (2007).

3 Infrared thermography: measurement and applications

Infrared thermography (IRT) is nowadays a classical technique for the non-destructive testing and evaluation (NDT&E) of materials and structures [1]. Within the terms infrared thermography are included the methods and devices that allow the measurement of the infrared radiation emitted by a body and its conversion to a temperature value. Another common way to describe this science is thermal imaging, that highlights the fact that the typical sensors are cameras that are able to produce images (called thermograms) of the observed objects. A quite comprehensive and formal definition is the following: Infrared thermography is a nondestructive, nonintrusive, noncontact technique that allows the mapping of thermal patterns, i.e., thermograms, on the surface of objects, bodies or systems through the use of an infrared imaging instrument, such as an infrared camera [2].

The fundamentals of this research field date back to the beginning of the XXIX century, with the studies of the British astronomer Sir William Herschel that discovered the infrared radiation in sunlight, followed by his son John that firstly promoted the term thermogram [3]. Other notable pioneers in the same century were the Italian physicists Macedonio Melloni, credited for the invention of the first thermopile, and the American Samuel Pierpont Langley, inventor of the bolometer. At the beginning of the XX century several authors such as Einstein, Golitzyn, Kirchhoff, Planck, Wien, defined and validated the basic laws of thermal radiation [3].

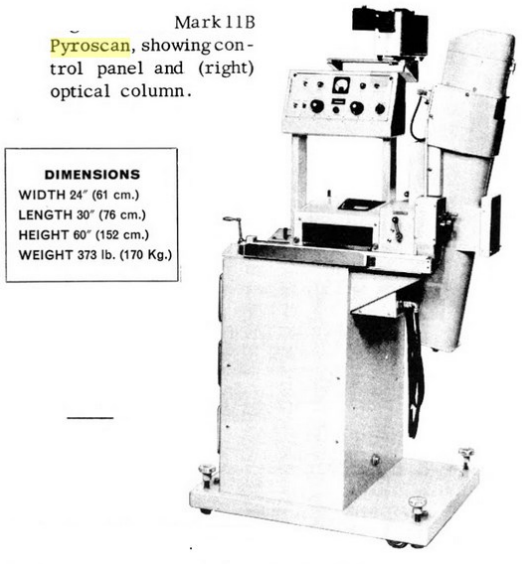

Figure 3.1: The first commercial thermal imaging devices like the Pyroscan MkII appeared on the market around 1960.

Anyway it was only around 1960 that the first commercial thermal system began to appear on the market, such as the AGA cameras or the Pyroscan depicted in Figure 3.1. Another great boost to the diffusion of thermal imagers happened in the last decade of the XX century with the introduction of uncooled microbolometric cameras and digital image storing and processing. These factors increased dramatically the compactness and portability of thermographic devices. Thanks to the great advances of electronic and computer science it is nowadays possible to work with extra small cameras (mounted on smartphones or drones) with always increasing performances and decreasing costs.

These innovations have a positive impact on the research that, similarly to the trend regarding buildings showed in the previous chapter, is showing an increased interest in infrared thermography. Figure 3.2 shows the data regarding the number of scientific articles that contain the term *thermography* inside their title, abstract, or keywords list, according to SCOPUS database. As for the building case, the research trend in thermography is steeper than the general increasing trend of scientific production.

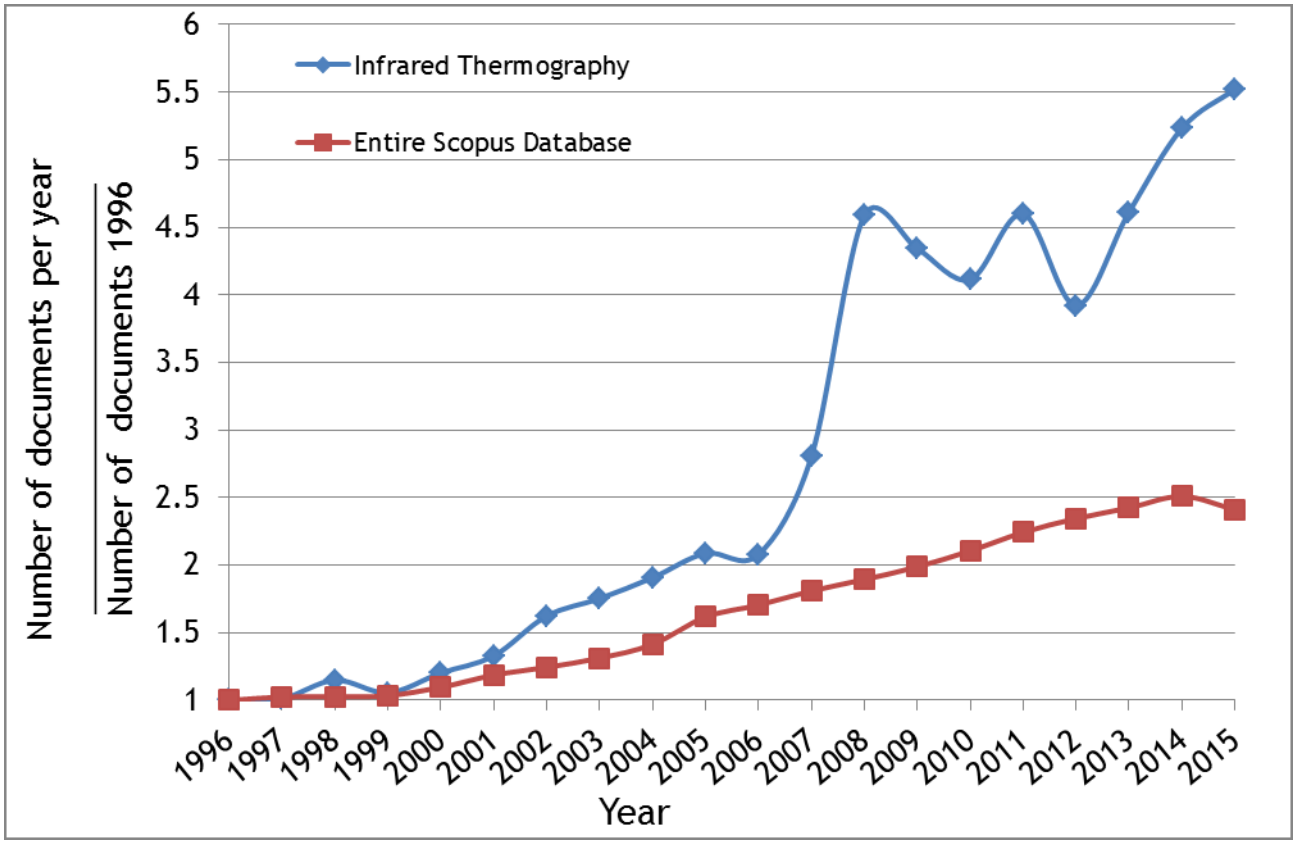

Figure 3.2: Comparison of trends in scientific production over the last 20 years according to SCOPUS database showing the contribute of the documents containing the term *thermography* inside their title, abstract, or keywords list (blue line) against the overall scientific works of the database (red line). Both trends are calculated by the ratio of number of documents per year over the number of documents of the baseline year (1996). The production increase in thermography is evident, especially in the last ten years.

3.1 Infrared thermography fundamentals

3.1.1 Physical laws

It is well known that matter emits electromagnetic radiation, that can be described either as a propagation of electromagnetic waves or as a transportation of particles (photons). The Planck-Einstein relation states that the energy *E* of a photon is proportional to its frequency *f* as in the following Equation 3.1:

$$E = hf = \frac{hc}{\lambda} \tag{3.1}$$

where:

- *h* is the Planck constant, approximately equal to 6.626 x 10^{-34} [J s];

- *f* is the frequency [s^{-1}];

- *c* is the speed of light in a vacuum, approximately equal to 3 x 10^{8} [m s^{-1}];

- *λ* is the wavelength [m].

The relation is used to describe the electromagnetic spectrum across different regions that are commonly divided into different subcategories, as shown in the next Figure 3.3.

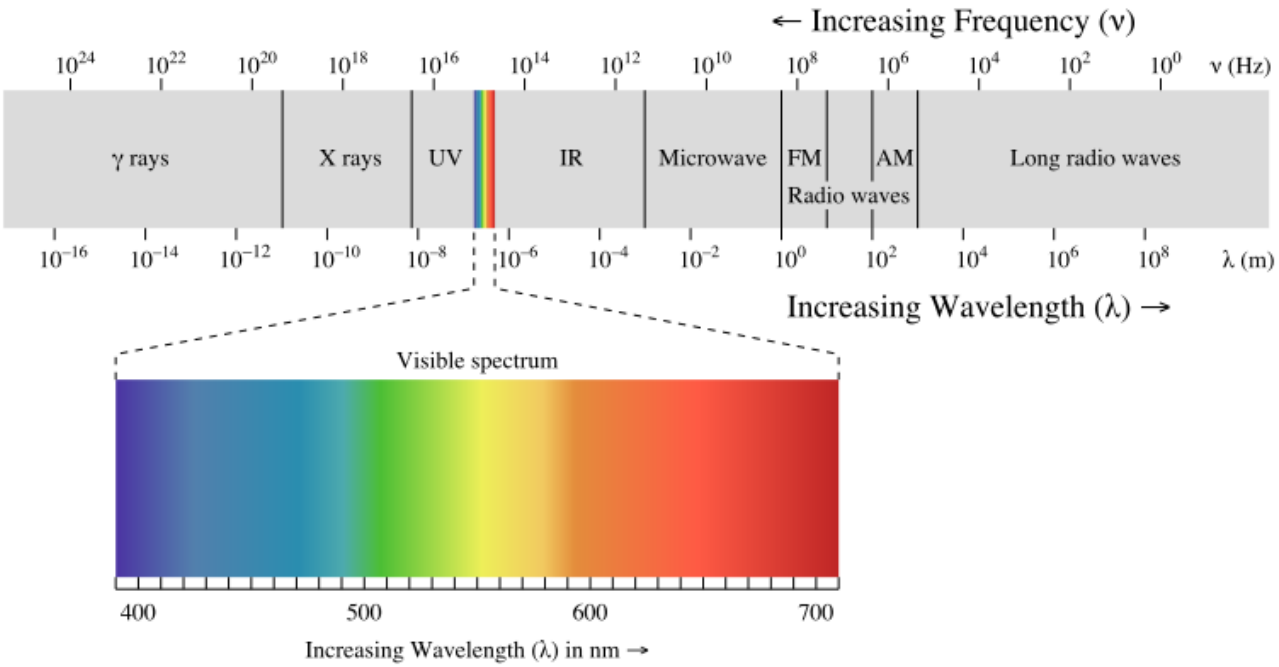

Figure 3.3: Electromagnetic spectrum divided in different categories across the range of wavelengths and frequencies [4].

From a thermographic standpoint, the most important part of the electromagnetic spectrum is the infrared range, that is located between 0.74 and 1000 μm. The infrared

spectrum is further divided into five categories, with slightly different limits according to the selected source and the application field. The following Table 3.1 collects the definitions according to different literature sources

Spectral bands	Range [μm]	Common detector materials*	Applications
Near InfraRed (NIR)	0.74-1	Si	Telecommunications
Short Wave InfraRed (SWIR)	1-3	InGaAs, PbS	Remote sensing
Middle Wave InfraRed (MWIR)	3-5	InSb, PbSe, PtSi, HgCdTe	High temperature inspection (indoors, scientific research)
Long Wave InfraRed (LWIR)	8-14	HgCdTe	Ambient temperature (outdoor, industrial inspection)
Very Long Wave InfraRed (VLWIR)	14-1000		Spectrometry, astronomy
*Si: silicon; In: Indium; Ga: gallium; As: arsenic; Pb: lead; S: sulfur; Sb: antimony; Se: selenium; Pt:platinum; Hg: mercury; Cd: Cadmium; Te: tellurium.			

Table 3.1: Spectral bands of the infrared regions, including nomenclature and typical applications [5].

To study the radiant heat transfer, Kirchhoff introduced the notion of blackbody as in idealized body that completely absorb all incident rays, and neither reflect nor transmit any [6]. Moreover a blackbody is an ideal and diffuse emitter, meaning that emits the maximum amount of energy of any other body at an equal temperature and that the emitted radiation does not depend from the direction. The spectral distribution of the radiation intensity from a blackbody was defined by Planck with the following Equation 3.2:

$$E_{\lambda,b}(\lambda,T) = \frac{C_1}{\lambda^5}\frac{1}{\exp\left(\frac{C_2}{\lambda T}\right)-1} \qquad (3.2)$$

where:

- C_1 is the first radiation constant, approximately equal to 3.74 x 10^8 [W μm^4 m^{-2}];

- C_2 is the second radiation constant, approximately equal 1.4389 x 10^4 [μm K].

Relying on the above Planck's law it is possible to determine the total radiant emission from a blackbody E_b, that according to the following Stefan-Boltzmann law is equal to:

$$E_b = \sigma T^4 \tag{3.3}$$

where σ is the Stefan-Boltzmann constant, equal to 5.67 x 10^8 [W m^{-2} K^4]. It is possible to note that Stefan-Boltzmann's law comes from the integration of Planck's law on the whole spectrum. The frequency λ_{max} where Planck's Law shows the maximum intensity is given by the following Wien's displacement Law:

$$\lambda_{max} = \frac{C_3}{T} \tag{3.4}$$

where C_3 is the third radiation constant, approximately equal to 2.89 x 10^3 [μm K]. These three laws are the basis of thermal imaging, as they define the boundary of the energy emitted by a body as a function of its temperature. The measurement performed with a thermal camera needs further definitions, as the measured energy is dependent also by the surface properties of the object. The main parameter of interest is the emissivity ε, that is defined by the following Equation 3.5:

$$\epsilon(\lambda, T_s) = \frac{E_{obj}(T_s)}{E_b(T_s)} \tag{3.5}$$

where:

- $E(T_s)$ is the thermal radiation emitted by the surface of a real object at a defined temperature (T_s);

- $E_b(T_s)$ is the thermal radiation emitted by a blackbody at the same temperature (T_s) and wavelength λ.

Using Equation 3.5 it is possible to define four kinds of objects:

- a blackbody, or perfect radiator, with an emissivity value equal to 1;

- a graybody, with a constant emissivity value ranging between 0 and 1;

- a whitebody, or perfect reflector, with an emissivity value equal to 0;

- a selective radiator, with an emissivity value ranging between 0 and 1 that depends on the wavelength λ.

The emissivity allows a quantification of the energy emitted by the object, taking care that the energy balance of a semitransparent medium depends on different parameters, as shown in Figure 3.4.

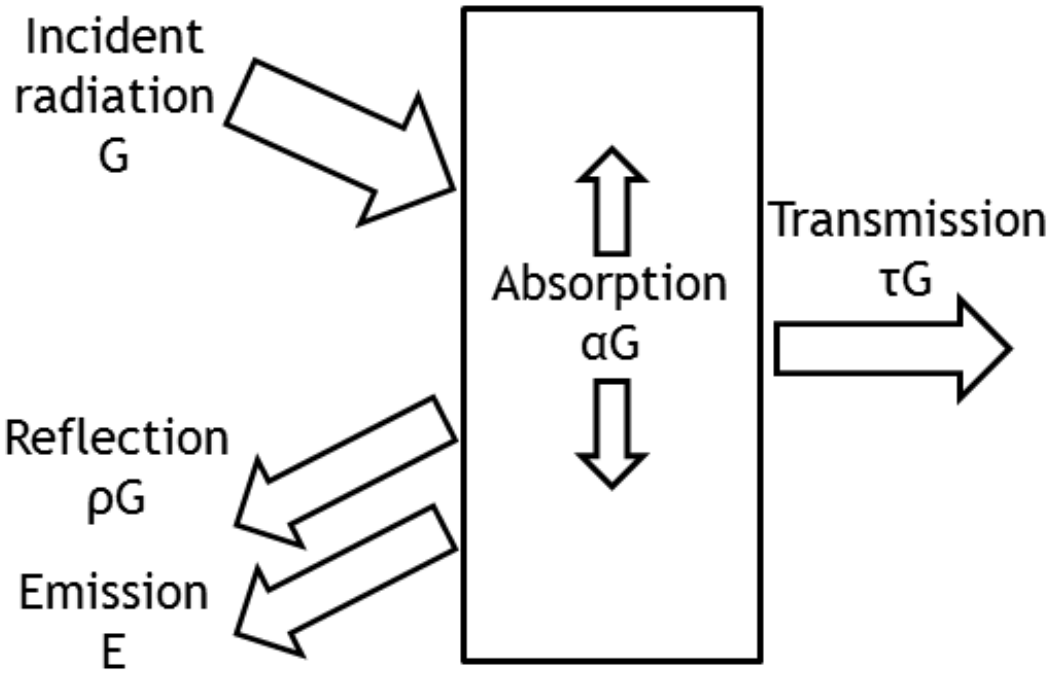

Figure 3.4: Energy balance of a semitransparent medium stimulated by an incident radiation *G*. Different parts of the energy are respectively absorbed, transmitted, or reflected.

The energy balance of Figure 3.4 is described by the following equation:

$$G = \alpha G + \rho G + \tau G \tag{3.6}$$

where:

- α is the absorptivity, that is the fraction of incident radiation absorbed by the surface;

- ρ is the reflectivity, that is the fraction of incident radiation reflected by the surface;

- τ is the transmissivity, that is the fraction of incident radiation transmitted by the surface. In case of an opaque material, the transmissivity value is 0.

This leads to next Equation3.7:

$$\alpha + \rho + \tau = 1 \tag{3.7}$$

and to Kirchhoff's law of thermal radiation, that states that for an arbitrary body emitting and absorbing thermal radiation in thermodynamic equilibrium, the emissivity is equal to the absorptivity.

A thermal camera is therefore able to measure the received radiation with the following Equation 3.8:

$$E_{tot} = (1 - \tau)E_{obj} + (1 - \epsilon)\,\tau\,E_{amb} + (1 - \tau)E_{atm} \tag{3.8}$$

where:

- the first term $(1-\tau)\,E_{obj}$ is the emission from the object, τ is the transmittance of the atmosphere;

- the second term $(1-\epsilon)\,\tau\,E_{amb}$ is the reflected emission from the ambient, assuming a constant value of ambient temperature for the surfaces seen by the object;

- the third term $(1-\tau)\,E_{atm}$ is the contribution of the atmosphere.

An accurate measurement requires therefore the knowledge of the emissivity of the observed object, of the attenuation due to the atmosphere, and of the temperature of the ambient surrounding the object (usually called reflected temperature) [7].

3.2 Infrared thermography techniques and applications

The number of thermographic techniques and their field of applications are constantly increasing over the years [3,8,9] thanks to the advances in research and instrumentation. Cataloguing all the material in a complete and detailed way would result in an extremely challenging task, that could easily become obsolete. Several authors proposed schematic classifications and amongst them a straightforward and powerful tool for the categorization of thermographic methods was proposed by Castanedo et al. [2]. When planning a thermographic measurement few questions are needed to describe quite accurately the selected procedure, taking into account the most important elements of the experimental layout: the thermal camera, the observed

object and the source of the thermal signal. The scheme proposed by the authors is shown in Figure 3.5.

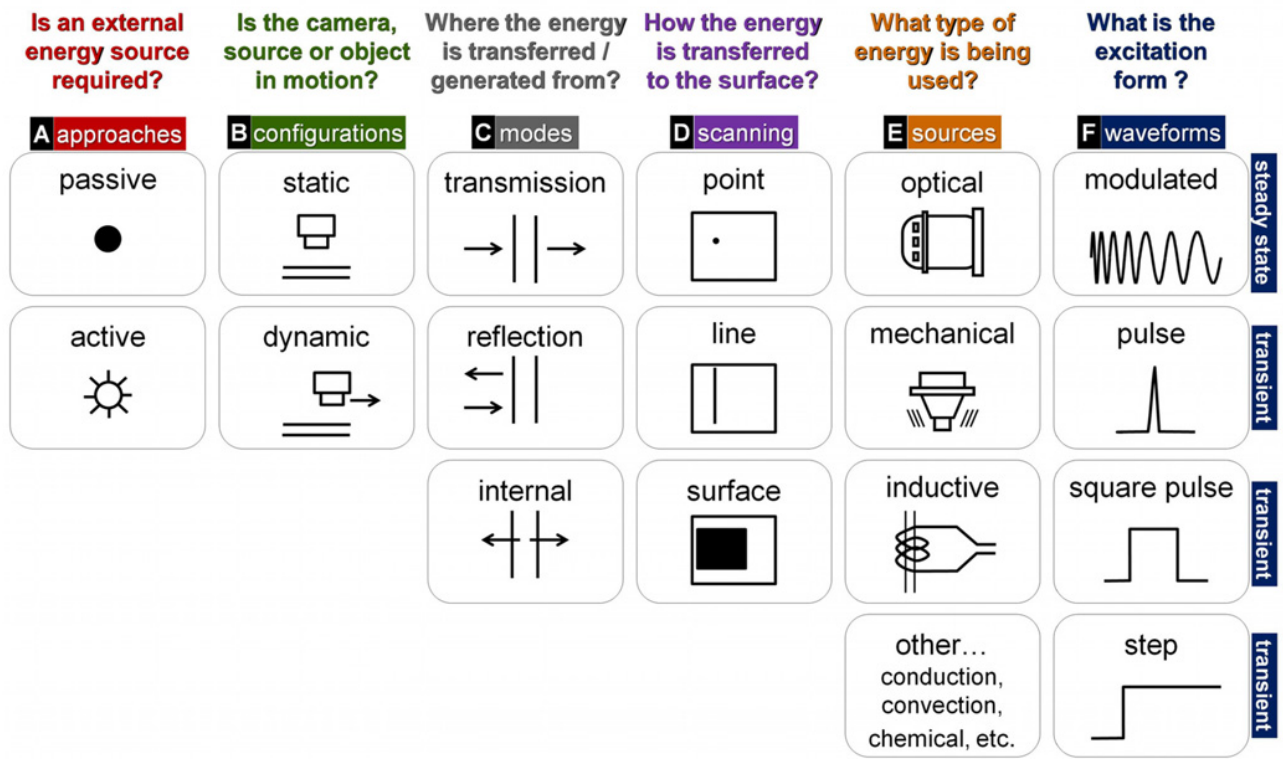

Figure 3.5: Elements to consider in a thermography inspection scenario [2]

The first question is always whether the approach is active or passive. In active thermography the observed object is stimulated by an artificial external source to create an interesting thermal signal. A typical example is the inspection of a mechanical component with defects, performed submitting the sample to an external thermal stimulus, such as a flash heating. In this case moving the component from the thermal equilibrium with its surrounding environment to a different thermal configuration gives the possibility to discover hidden defects. On the other side, passive thermography is chosen when the observed object has by itself a detectable thermal signal. This leads usually to a qualitative analysis (defect detection) rather than a quantitative one (defect quantification in size and depth, measurement of thermal properties), that is facilitated by the choice of an active approach. A typical example is the measurement of the human body, such as in medical screening.

The second question investigates whether the camera, the heating source or the object are in motion. These three basic elements, that are common to every thermographic investigation, are usually placed statically during an experiment to facilitate the data acquisition and processing. However in some cases it is not possible to investigate the

observed object from a single viewpoint, such as wide or complex objects, therefore either the camera or the object itself should be moved. In other cases it also convenient to move the thermal source [10].

The third question further defines the layout of the experiment, as the energy source that provides the thermal signal could be on the opposite side of the object (transmission), on the same side (reflection), or inside the object (internal). The choice is again related to the shape and size of the specimen but it is mainly based on the type of the stimulation source.

The remaining questions analyze more in details the energy source. The fourth one distinguishes three energy transfer modes: point, line and surface. The first two are typical of laser sources in dynamic configuration, while the latter one is the most common for static ones.

The fifth question describes the source of the energy signal, that usually consists in heating the observed object. Optical sources (flashes or lamps) are the most traditional heating mediums; convection is also frequently used typically by forced ventilation with air heaters or heat guns. Other sources include mechanical stimulation (e.g. sound or ultrasound [11]), inductive heating (e.g. eddy currents [12]) and more peculiar techniques, such as conduction heating and cooling using Peltier cells [13] or chemical cooling with liquid nitrogen.

The final question regards the temporal variation of the energetic stimulus [14], that could be modulated (thermal waves), a pulse (when using rapid thermal sources), a square pulse or a step when using slower thermal sources, such as air heating. The overall duration of the source depends anyway on the thermophysical properties of the observed object.

The aforementioned thermographic procedures have a wide range of applications in different fields:

- civil engineering and buildings. IRT is frequently used to diagnosis the building status [15], investigating the building envelope and the HVAC system for energy or moisture related issues [16,17]. IRT is also applied to the structural monitoring of civil engineering infrastructures [18];

- non-destructive testing and evaluation (NDT&E) of components, such as the testing of parts for the aerospace industry [19] made with composite materials [20], the

determination of the fatigue limit of mechanical components [21], or the evaluation of electronic components [22];

- study of heat transfer and fluid dynamics. IRT is applied in several layouts, including the study of heat exchangers[23] and in the measurement of heat transfer coefficients [24];

- microscale thermography, applied the study of biological [25] or organic materials [26];

- measurement of material properties, such as thermal diffusivity [13] or thermal conductivity [27];

- maintenance monitoring, checking both in laboratory or in field components such as electrical switches [28] or fluid pipelines [29];

- surveillance and recognition, aiming at target detection of trespasser [30] or face recognition [31];

- environmental monitoring, such as investigation of waste-disposal sites [32], volcanoes monitoring [33], or vegetation evaluation [34] also with the application of airborne or drone platforms;

- industrial processes, ranging from food quality evaluation [35] to welding and steel making [36];

- biomedical, ranging from fever scanning [37] to the investigation a vast number of diseases [38,39] also in athletes [40]. IRT has several applications also in veterinary, ranging from equine diagnostics [41] to the detection of wild animals [42];

- works of art, for conservation purposes [43], also in combination with other investigation techniques [44];

A wide number of scientific documents describing thermographic applications of the last 20 years are available in open access web repositories, such as the ndt.net database [45] or the QIRT Conference archive [46].

3.3 References

[1] X. Maldague, Theory and practice of infrared technology for nondestructive testing, Wiley, 2001.
[2] C. Ibarra-Castanedo, J.R. Tarpani, X.P.V. Maldague, Nondestructive testing with thermography, Eur. J. Phys. 34 (2013) S91. doi:10.1088/0143-0807/34/6/S91.

[3] V. Vavilov, Thermal NDT: historical milestones, state-of-the-art and trends, Quantitative InfraRed Thermography Journal. 11 (2014) 66–83. doi:10.1080/17686733.2014.897016.
[4] P. Ronan, Electromagnetic spectrum File:Electromagnetic spectrum c.svg, 2009. https://commons.wikimedia.org/wiki/File:EM-Spektrum.svg.
[5] C.I. Castanedo, Quantitative subsurface defect evaluation by pulsed phase thermography: depth retrieval with the phase, Université Laval, 2005. http://www.theses.ulaval.ca/2005/23016/23016.pdf.
[6] G. Kirchhoff, On the relation between the radiating and absorbing powers of different bodies for light and heat, in: The London, Edinburgh and Dublin Philosophical Magazine and Journal of Science, Taylor & Francis, 1860.
[7] W. Minkina, S. Dudzik, Infrared Thermography: Errors and Uncertainties, John Wiley & Sons, Ltd, Chichester, UK, 2009. http://doi.wiley.com/10.1002/9780470682234 (accessed December 11, 2016).
[8] M. Vollmer, K.-P. Möllmann, Infrared Thermal Imaging: Fundamentals, Research and Applications, Wiley, 2010.
[9] C. Meola, ed., Infrared Thermography Recent Advances and Future Trends, BENTHAM SCIENCE PUBLISHERS, 2012. http://www.eurekaselect.com/101682/volume/1 (accessed December 9, 2016).
[10] T. Li, D.P. Almond, D.A.S. Rees, Crack imaging by scanning laser-line thermography and laser-spot thermography, Measurement Science and Technology. 22 (2011) 035701. doi:10.1088/0957-0233/22/3/035701.
[11] S.M. Shepard, T. Ahmed, J.R. Lhota, Experimental considerations in vibrothermography, in: D.D. Burleigh, K.E. Cramer, G.R. Peacock (Eds.), 2004: p. 332. doi:10.1117/12.546599.
[12] G. Riegert, T. Zweschper, G. Busse, Lockin thermography with eddy current excitation, Quantitative InfraRed Thermography Journal. 1 (2004) 21–32. doi:10.3166/qirt.1.21-32.
[13] P.G. Bison, S. Marinetti, A. Mazzoldi, E. Grinzato, C. Bressan, Cross-comparison of thermal diffusivity measurements by thermal methods, Infrared Physics & Technology. 43 (2002) 127–132. doi:10.1016/S1350-4495(02)00130-5.
[14] K. Chatterjee, S. Tuli, S.G. Pickering, D.P. Almond, A comparison of the pulsed, lock-in and frequency modulated thermography nondestructive evaluation techniques, NDT & E International. 44 (2011) 655–667. doi:10.1016/j.ndteint.2011.06.008.
[15] C.A. Balaras, A.A. Argiriou, Infrared thermography for building diagnostics, Energy and Buildings. 34 (2002) 171–183. doi:10.1016/S0378-7788(01)00105-0.
[16] G. Dall'O', L. Sarto, A. Panza, Infrared Screening of Residential Buildings for Energy Audit Purposes: Results of a Field Test, Energies. 6 (2013) 3859–3878. doi:10.3390/en6083859.
[17] E. Grinzato, V. Vavilov, T. Kauppinen, Quantitative infrared thermography in buildings, Energy and Buildings. 29 (1998) 1–9. doi:10.1016/S0378-7788(97)00039-X.
[18] M.. Clark, D.. McCann, M.. Forde, Application of infrared thermography to the non-destructive testing of concrete and masonry bridges, NDT & E International. 36 (2003) 265–275. doi:10.1016/S0963-8695(02)00060-9.
[19] C. Meola, G.M. Carlomagno, A. Squillace, A. Vitiello, Non-destructive evaluation of aerospace materials with lock-in thermography, Engineering Failure Analysis. 13 (2006) 380–388. doi:10.1016/j.engfailanal.2005.02.007.
[20] N.P. Avdelidis, D.P. Almond, A. Dobbinson, B.C. Hawtin, C. Ibarra-Castanedo, X. Maldague, Aircraft composites assessment by means of transient thermal NDT,

Progress in Aerospace Sciences. 40 (2004) 143–162. doi:10.1016/j.paerosci.2004.03.001.
[21] G. La Rosa, Thermographic methodology for rapid determination of the fatigue limit of materials and mechanical components, International Journal of Fatigue. 22 (2000) 65–73. doi:10.1016/S0142-1123(99)00088-2.
[22] O. Breitenstein, M. Langenkamp, Lock-in Thermography: Basics and Use for Functional Diagnostics of Electronic Components, Springer Science & Business Media, 2003.
[23] H. Ay, J. Jang, J.-N. Yeh, Local heat transfer measurements of plate finned-tube heat exchangers by infrared thermography, International Journal of Heat and Mass Transfer. 45 (2002) 4069–4078. doi:10.1016/S0017-9310(02)00132-1.
[24] G.M. Carlomagno, G. Cardone, Infrared thermography for convective heat transfer measurements, Experiments in Fluids. 49 (2010) 1187–1218. doi:10.1007/s00348-010-0912-2.
[25] C. Pradere, J. Morikawa, J. Toutain, J.-C. Batsale, E. Hayakawa, T. Hashimoto, Microscale thermography of freezing biological cells in view of cryopreservation, Quantitative InfraRed Thermography Journal. 6 (2009) 37–61. doi:10.3166/qirt.6.37-61.
[26] J. Morikawa, E. Hayakawa, T. Hashimoto, Application of micro-scale thermography to the thermal analysis of polymeric and organic materials, in: M. Safai, J.R. Brown (Eds.), 2011: p. 801319. doi:10.1117/12.884943.
[27] P. Bison, E. Grinzato, Fast estimate of solid materials thermal conductivity by IR thermography, Quantitative InfraRed Thermography Journal. 7 (2010) 17–34. doi:10.3166/qirt.7.17-34.
[28] A.S.N. Huda, S. Taib, Application of infrared thermography for predictive/preventive maintenance of thermal defect in electrical equipment, Applied Thermal Engineering. 61 (2013) 220–227. doi:10.1016/j.applthermaleng.2013.07.028.
[29] G. Cadelano, A. Bortolin, G. Ferrarini, B. Molinas, D. Giantin, P. Zonta, P. Bison, Corrosion Detection in Pipelines Using Infrared Thermography: Experiments and Data Processing Methods, Journal of Nondestructive Evaluation. 35 (2016). doi:10.1007/s10921-016-0365-5.
[30] W.K. Wong, P.N. Tan, C.K. Loo, W.S. Lim, An Effective Surveillance System Using Thermal Camera, in: IEEE, 2009: pp. 13–17. doi:10.1109/ICSAP.2009.12.
[31] F.J. Prokoski, R.B. Riedel, J.S. Coffin, Identification of individuals by means of facial thermography, in: IEEE, 1992: pp. 120–125. doi:10.1109/CCST.1992.253768.
[32] E. Zilioli, M.A. Gomarasca, R. Tomasoni, Application of terrestrial thermography to the detection of waste-disposal sites, Remote Sensing of Environment. 40 (1992) 153–160. doi:10.1016/0034-4257(92)90012-9.
[33] L. Spampinato, S. Calvari, C. Oppenheimer, E. Boschi, Volcano surveillance using infrared cameras, Earth-Science Reviews. 106 (2011) 63–91. doi:10.1016/j.earscirev.2011.01.003.
[34] J.M. Costa, O.M. Grant, M.M. Chaves, Thermography to explore plant-environment interactions, Journal of Experimental Botany. 64 (2013) 3937–3949. doi:10.1093/jxb/ert029.
[35] A.A. Gowen, B.K. Tiwari, P.J. Cullen, K. McDonnell, C.P. O'Donnell, Applications of thermal imaging in food quality and safety assessment, Trends in Food Science & Technology. 21 (2010) 190–200. doi:10.1016/j.tifs.2009.12.002.
[36] M. Viale, O. Martin, F. Muratori, U. Bertezzolo, J. Perez, J. Usart, Application of on-line infrared thermography in steel making industry, in: 2007: p. 65410H. doi:10.1117/12.721225.

[37] L.-S. Chan, G.T.Y. Cheung, I.J. Lauder, C.R. Kumana, I.J. Lauder, Screening for fever by remote-sensing infrared thermographic camera, J Travel Med. 11 (2004) 273–279.
[38] B.B. Lahiri, S. Bagavathiappan, T. Jayakumar, J. Philip, Medical applications of infrared thermography: A review, Infrared Physics & Technology. 55 (2012) 221–235. doi:10.1016/j.infrared.2012.03.007.
[39] E.F.J. Ring, K. Ammer, Infrared thermal imaging in medicine, Physiol. Meas. 33 (2012) R33. doi:10.1088/0967-3334/33/3/R33.
[40] C. Hildebrandt, C. Raschner, K. Ammer, An Overview of Recent Application of Medical Infrared Thermography in Sports Medicine in Austria, Sensors. 10 (2010) 4700–4715. doi:10.3390/s100504700.
[41] A.L. Eddy, L.M. Van Hoogmoed, J.R. Snyder, The Role of Thermography in the Management of Equine Lameness, The Veterinary Journal. 162 (2001) 172–181. doi:10.1053/tvjl.2001.0618.
[42] J. Cilulko, P. Janiszewski, M. Bogdaszewski, E. Szczygielska, Infrared thermal imaging in studies of wild animals, European Journal of Wildlife Research. 59 (2013) 17–23. doi:10.1007/s10344-012-0688-1.
[43] D. Gavrilov, R.G. Maev, D.P. Almond, A review of imaging methods in analysis of works of art: Thermographic imaging method in art analysis, Canadian Journal of Physics. 92 (2014) 341–364. doi:10.1139/cjp-2013-0128.
[44] C. Ibarra-Castanedo, S. Sfarra, D. Ambrosini, D. Paoletti, A. Bendada, X. Maldague, Diagnostics of panel paintings using holographic interferometry and pulsed thermography, Quantitative InfraRed Thermography Journal. 7 (2010) 85–114. doi:10.3166/qirt.7.85-114.
[45] NDT Database & Journal of Nondestructive Testing - NDT, Ultrasonic Testing, X-Ray, Radiography, Eddy Current and all NDT Methods, (2016). http://www.ndt.net.
[46] QIRT Conference Open Archives, (2016). http://qirt.gel.ulaval.ca/dynamique/index.php?idM=38.

4 Infrared thermography as an imaging technique: image processing methods

The performance of a thermographic measurement is not limited to the acquisition of a signal. The raw thermal data coming from a thermographic measurement must be processed, whether the analysis is focused on single thermograms or on thermal sequences. In this chapter, based on published works [1–4], traditional image processing method are described and compared to innovative ones, derived from the Partial Least Squares (PLS) method. The proposed techniques are applied to the thermographic analysis of works of art, that are recently built or ancient frescoes. The image processing is performed in Matlab environment, using the IR-View tool [5] or custom routines.

4.1 Analysis of thermal images

When analyzing thermal images, either single frames or thermal sequences, it is possible to distinguish two steps: a preliminary phase, where several corrections are performed, and a calculation phase, where image processing algorithms are applied to the corrected images.

Method	**Based on**	**Improves**
Emissivity correction	Knowledge of the materials or measurement	Absolute temperature measurement
Environmental parameters	Ancillary measurement	Absolute temperature measurement
Temperature correction	Reference target (with or without embedded sensor)	Temperature measurement
Geometrical correction	Reference targets or known geometry	Temperature and heat flux measurement
Application of algorithms	Stimulation technique or specimen characteristics	Signal to Noise Ratio

Table 4.1: Activities that are typically executed on thermal images after a measurement to improve the results.

During the preliminary phase, the focus is on two key aspects: temperature and geometry. The first activity described in Table 4.1 is the emissivity correction. For a correct absolute temperature measurement, this is in several cases the most important parameter. The emissivity value could be known, from literature [6] or from material datasheet (e.g. for high emissive tapes or varnishes), or measured on the object under testing [7]. Other factors that influence the temperature measurement are environmental parameters such as reflected temperature, atmospheric temperature, relative humidity, and distance from the object. For building applications (especially indoor ones) dealing with low-emissive or polished materials, the main parameter that can significantly influence the measurement is the reflected temperature. This value is obtained from auxiliary temperature probes, such as resistance temperature detectors.

When dealing with long-term surveys, thermal camera may suffer from thermal drift or temperature oscillations around the mean value. This issues could be solved with the use of a reference target, that may have an embedded temperature sensor. The easiest strategy is positioning in the camera field of view an object that has an high thermal inertia and that is not subjected to any thermal stimulus. The observed temperature on this object could then be subtracted to the entire thermal image, shaving the valleys and peaks due to fluctuations. If the target has an embedded temperature probe and it is arranged as a blackbody [8], the measured temperature value could be used as an absolute temperature reference, allowing a real-time temperature calibration.

The geometrical correction, set aside the vignetting or distortion issues that are intrinsic to the camera system and that should be corrected with a preliminary camera calibration [9], may be implemented using reference targets or taking advantage of the knowledge of the observed object. In both cases, some control points on the thermal image (usually at least four on a single plane) should be found and matched to the known coordinates of the targets or of the object. This procedure enhances the accuracy of the spatial averaging of temperatures and also the calculation of heat fluxes referred to a known surface. The correction is usually applied to a two dimensional plane, even if more complex three dimensional corrections may be performed.

After the correction of temperature and geometrical factors it is possible to apply several algorithms to thermal data, especially on thermal sequences. It is common to call this step image processing, as thermographic data are *de facto* images, and their analysis could be conducted starting from this paradigm. The aim is obviously the

enhancement of the original thermal signal, that is seen as an increase of the Signal-to-Noise Ratio. A detailed list of the available techniques and the obtainable results is proposed in the next sections.

4.2 Traditional image processing methods

A wide set of image processing methods has been applied and evaluated in the field of thermographic analysis. Some algorithms are currently a standard option for thermal data processing, and are included in post-processing software [5]. The traditional methods that were applied on the case studies described in 4.5 are listed in the following Table 4.2, along with few basic characteristics.

Method	**Characteristics**	**Reference**
Correlated contrast	Based on correlation algorithm Compression of thermal sequence in one image	[10]
Principal Component Thermography	Based on Principal Component Analysis Great data compression and noise reduction Thermal sequence is reduced to few images	[11,12]
Fourier Transform	Based on Fourier Transform Especially fitted for the analysis of periodic phenomena Thermal sequence is reduced to few Amplitude or Phase images	[13]
Multiple Sum Average	Based on contrast method Compression of thermal sequences in one image Good noise reduction	[1]
Thermographic signal reconstruction	Based on heat equation Especially fitted for the analysis of pulsed heating Thermal sequence is reduced to few images	[14,15]

Table 4.2: List of image processing algorithms that are typically applied to the analysis of thermal sequences.

Other methods that are not described in this work but are frequently applied to the analysis of infrared images are Differential Absolute Contrast[16], High-Order Statistics [3] and Wavelet [13].

4.2.1 Correlated contrast

When dealing with thermal sequences of images, defects cannot always be observed directly on a single infrared image. For this reason some algorithms try to compress all the information into a single image, for example computing a correlation image [10]. In Statistics correlation is interpreted as a relationship between two random variables such that to each value of the first corresponds with some regularity a value of the second one. Correlation should be applied very carefully, as it does not necessarily imply causation. Experience has shown that it is nevertheless a powerful tool for the enhancement of small subsurface defects. As stated before, correlation needs a reference variable: for thermographic sequences the easiest solution is to choose the average of the temperature evolution of all the pixels, as this choice removes any human decision. The observed variables are the temperature values of each pixel in the sequence. The calculation of the correlation coefficients leads to a matrix with a wide range of values: to avoid this issue it is possible to compute the m-th root of the coefficients to lower the dynamic.

4.2.2 Principal Component Thermography

Principal component analysis (PCA) is a statistical procedure widely used for image processing. This technique uses orthogonal transformations to convert a set of observations of possibly correlated variables into observations of a set of linearly uncorrelated variables. The latter are called principal components and their number is less than or equal to the number of original variables. Principal component thermography (PCT) [11,12,17] works like PCA and is based on the singular value decomposition (SVD), a method to extract spatial and temporal data from a matrix in a compact and simplified manner. The essence of SVD is to simultaneously provide the PCAs for both the row and column spaces [18]. The singular value decomposition of a matrix $X \in R^{pxq}$, with $p>q$, is based on the following Equation 4.1.

$$X = USV^T \tag{4.1}$$

where:

U is a *p x q* matrix with orthogonal columns;

S is a diagonal matrix (*q x q*) with the singular values of *X* on the diagonal

V^T is a (*q x q*) orthogonal matrix.

As this method works with two dimensional matrices, the original thermal sequence *T*, that has three dimensions (*a,b,n*), must be reshaped into a T_r matrix of size *pxq*. The new T_r matrix has *a x b* columns and n rows, meaning that the temperature profiles of each pixel are arranged vertically. In this case, the matrix *U* is a set of orthogonal statistical modes known as empirical orthogonal functions (EOF) describing the spatial variations of data, while the rows of the matrix V^T are the principal components, describing time variations. Each EOF represents a different part of the data variability and the matrix shows the EOFs in decreasing order: the first one contains the most part of variation, the following less. The great advantage of PCT is that all the data variations of a thermal sequence made by hundreds of images can be explained with only a few images, usually less than ten.

4.2.3 Fourier Transform

The data obtained from a thermographic experiment are temperature profiles in the time domain. Through the discrete Fourier transform (DFT) it is possible to analyze the data in the frequency domain, as in Equation 4.2:

$$F_n = \Delta t \sum_{k=0}^{N-1} T(k\Delta t) \exp^{-\left(\frac{i2\pi nk}{N}\right)} = Re(F_n) + iIm(F_n) \qquad (4.2)$$

where:

n is the frequency increment,

Δt is the sampling interval

Re and *Im* are respectively the real and imaginary part of the transform.

These are the basis for the estimation of the amplitude *A* and phase *P* as in the following Equation 4.3:

$$A_n = \sqrt{\mathrm{Re(F_n)}^2 + Im(F_n)^2} \qquad P_n = \tan^{-1}\left(\frac{Im(F_n)}{Re(F_n)}\right) \qquad (4.3)$$

The discrete Fourier transform is usually applied to a wide range of thermal testing and the analysis of the phase is of peculiar interest, as it is less influenced than the raw data by several parameters that could introduce undesired noise such as environmental reflections, emissivity variations, non-uniform heating [13].

4.2.4 Multiple Sum Average

The basic idea of the multiple sum average (MSA) algorithm is enhancing the temperature signal contained in the original thermal sequence, preserving the physical consistency. The first step is the creation of an averaged matrix *M*, where each pixel of each timed image is replaced with the average of its neighboring pixels of the same timed image. After that, it is possible to create a new image where each pixel is the sum, for every timed image *t*, of the difference between the original temperature value and the average value, as shown by the next Equation 4.4:

$$MSA_{i,j} = \sum_{t=1}^{n} X(t)_{i,j} - M(t)_{i,j} \qquad (4.4)$$

where *X* is the original thermal sequence composed by *n* frames having width and height equal to *a* and *b* pixels. An advantage of this method is the possibility, as in correlation, to compress the information of a sequence into a single image.

4.2.5 Thermographic signal reconstruction

Thermographic Signal Reconstruction (TSR) [14,15,19] is widely applied in Non-Destructive Testing and Evaluation. This method is based on the solution of the one dimensional heat conduction equation on a semi-infinite body that has been subjected to a pulsed thermal excitation. This procedure analyzes the data acquired with pulsed thermographic experiments, fitting the experimental data represented in log-log space polynomial function as in Equation 4.5:

$$\ln(\Delta T) = \mathrm{a}_0 + a_1 \ln(t) + a_2[\ln(t)]^2 + \cdots + a_n[\ln(t)]^n \quad (4.5)$$

where:

ΔT is the temperature profile of a single pixel during the experiment;

a_0, a_1,…, a_n are the coefficients of the polynomial fitting.

The fitting is calculated for every pixel of the thermal image, obtaining the corresponding maps of coefficients. As in PCT, it is therefore possible to compress the original three dimensional data matrix *T* into a smaller one that maintains the same width and height but changes its depth, that is equal to *n*, the degree of the polynomial fitting. The latter value is variable and in this works it has been set to 5.

4.3 Innovative image processing methods: the Partial Least Squares approach

The Partial Least Squares (PLS) [20] is a family of statistical procedures that is commonly applied in different fields, such as chemistry, economics and neuroscience. PLS methods include correlation, regression and path modelling techniques. One of the advantages of these techniques is the possibility of analyzing simultaneously two matrices X and Y, taking into account the relationship between each other. One of these matrices is necessarily the data matrix, the second one could be the time vector or a model matrix. After choosing a number of components c (usually similar to the useful components of PCA) PLS performs the simultaneous decomposition of both X and Y. Mathematically, PLS is expressed as in the following Equations 4.6 and 4.7:

$$X = TP^T + E \quad (4.6)$$

$$Y = TQ^T + F \quad (4.7)$$

where

P and *Q* are defined as loadings;

T is an orthonormal matrix defined as score;

E and *F* are residuals.

If $X \in R^{nxs}$ and $X \in R^{nxm}$, then the loading $P \in R^{sxc}$, the loading $Q \in R^{mxc}$ and the score $T \in R^{nxc}$. Different algorithms are available to calculate the PLS, in this work the SIMPLS algorithm has been applied [21]. The data matrix could be the X or the Y matrix, leading in the first case to the PLST approach [22] and in the second case to the PLSRT approach. With the former, the X matrix is the data matrix while the Y is a time vector with all the ordered acquisition time of the experiment or their corresponding frequencies. With the latter PLSRT approach, the Y matrix is the data matrix and the X matrix is a model matrix that can be connected by the following linear Equation 4.8:

$$Y = XB + E \tag{4.8}$$

where *B* is a coefficient matrix that with the utilized implementation of the SIMPLS algorithm has *s+1* rows and *m* columns. The choice of the model matrix *X* is related to the type of experiment; in this work a similarity with TSR has been investigated. For this reason the regression is executed in logarithmic scales, as in the next Equation 4.9:

$$\begin{bmatrix} \log(T_{1,1}) & \dots & \log(T_{p,1}) \\ \vdots & \ddots & \vdots \\ \log(T_{1,n}) & \dots & \log(T_{p,n}) \end{bmatrix} = \begin{bmatrix} 1 & \log(t_1) & \log^2(t_1) & \dots & \log^4(t_1) \\ \vdots & \vdots & \vdots & \ddots & \vdots \\ 1 & \log(t_n) & \log^2(t_n) & \dots & \log^4(t_n) \end{bmatrix} B + E \tag{4.9}$$

In this work the number of components c has been set to 5.

4.4 Tools for the comparison of different algorithms

Different methods are available to compare the application of multiple algorithms to the same thermal sequence. If the defect location and size are known it is then possible to create a defect map that could be compared pixel by pixel to the obtained results. This is the usual case of laboratory specimen. If the defect location and size are unknown, the knowledge of a sound area is needed to evaluate the strength of the signal, as the defect are expected to stand out against the background. This is the typical case of real applications. If also the sound area is unknown but the global size of the defects is very

small with respect to the image, the mean value of the image could be chosen as the reference value.

4.4.1 Signal based comparison

The most basic comparison tool are based on the knowledge of the defective areas and of a sound area that acts as a reference. The a-priori knowledge of the defects allows a precise quantification of the signal. The a-posteriori individuation of defective and sound areas is derived by the analysis of the results. This process is based on thresholding and user experience, that allow to make reasonable assumptions about on the expected defect size and locations. Obviously this case has an intrinsic uncertainty, especially in the definition of the defect size.

The preliminary step required to compare different algorithms is the equalization of different outputs. Typically the choice is converting each resulting image to a dimensionless value, as in greyscale image that have a unitary amplitude range. Then a first attempt to quantify the signal strength could be performed with Equation 4.10:

$$S = Def_{avg} - Snd_{avg} \tag{4.10}$$

where:

S is the signal [a.u.];

Def_{avg} is the average value of a defective area [a.u.];

Snd_{avg} is the average value of a sound area [a.u.].

If the algorithm shows defective values lower than the sound ones, the absolute value may be used. Another widespread method is the Signal-to-Noise Ratio (SNR), that is described by Equation 4.11:

$$SNR = 20\log_{10}\left(\frac{abs\left(Def_{avg} - Snd_{avg}\right)}{\sigma}\right) \tag{4.11}$$

where σ is the standard deviation of the sound area. The resulting value is expressed in dB.

4.4.2 Receiver operating characteristic (ROC) curves

Receiver operating characteristic (ROC) analysis arises from the theory of signal detection, as a model of how well the receiver can detect a signal in presence of noise. Its main feature is the discrimination between the hit rate (or true positive rate) and the rate of false positives as two separate performances [23].

		Condition (as determined by *Golden Standard*)		
		Condition positive	Condition negative	
Test Outcome	Test outcome positive	**True positive**	**False positive** (Type I error)	Precision Σ True positive/ Σ Test outcome positive
	Test outcome negative	**False negative** (Type II error)	**True negative**	Negative predictive value Σ True negative/ Σ Test outcome negative
		Sensitivity Σ True positive/ Σ Condition positive	Specificity Σ True negative/ Σ Condition negative	

Table 4.3: Confusion matrix that shows the possible outcomes of a binary classification test.

The sensitivity and specificity are statistical definitions that quantify the performance of a binary classification test. Sensitivity measures the share of actual positives that are correctly recognized as positives. Specificity represents the share of negatives, which are correctly recognized as negative. Ideal forecasting algorithm would feature a 100% sensitivity and 100% specificity. In this paper, the 2D ROC space analysis has been utilized to compare the performance of the algorithms, described in the previous sections, in a defect detection procedure. A Golden Standard binary map of defects is

available for the specimen. This map is the reference for the defect maps that could be obtained from the image processing setting a threshold. It is therefore possible to compare the Golden Standard and the defect maps with a variable value of threshold, from 0 to 1.

The ROC space analysis or ROC curve is a graph where for every threshold value the binary classifiers are mapped as points in the ROC space where the Cartesian coordinate X is the false positives rate (1 - Specificity) and the Y is the true positive rate (Sensitivity) as shown in the next image.

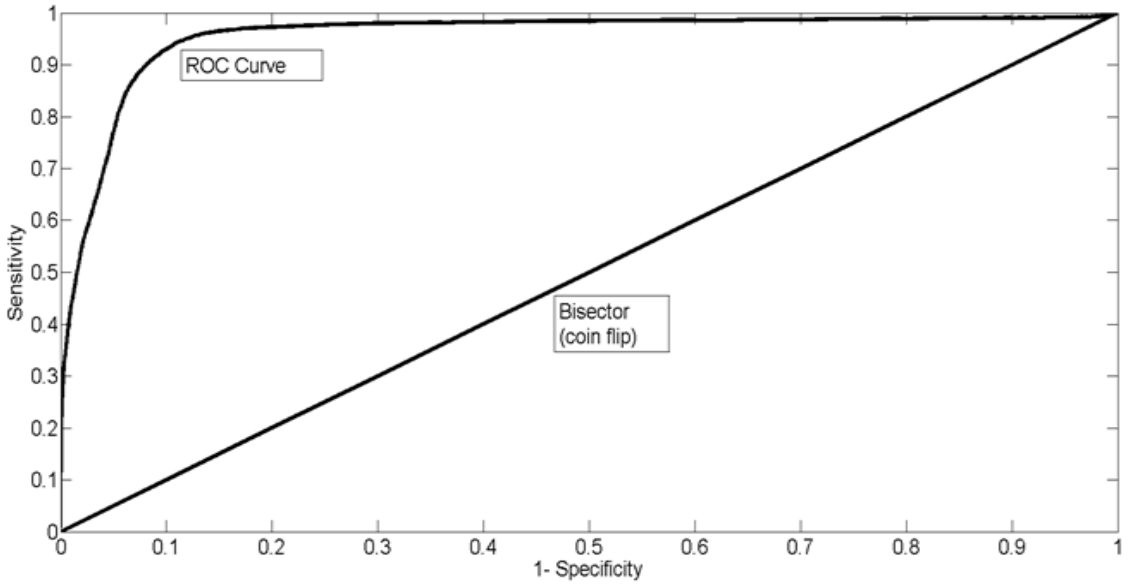

Figure 4.1: Typical ROC curve, obtained plotting the classifier values at different thresholds ranging from 0 to 1. The bisector is equal to a coin flip (random guess). The ROC curve should be in the upper triangle of the plot, as far as possible from the bisector.

Every single test procedure is represented as a point in the graph, between the boundaries position (0,1) that is the optimal classifier, and (1,0) that is a classifier that gets always wrong. The bisector (0,0)-(1,1) represents the random behavior. Points over the bisector represent classifiers that work better than random; the points below the bisector are tests performing worse than random.

4.5 Image processing applications: works of art

The algorithms described in the previous sections of this chapter may be applied to a wide range of infrared tests. The applications that are proposed in the next section regard frescoes, that are chosen as a challenging and valuable reference case.

Fresco is one of the oldest and most durable painting techniques, utilized since ancient times in buildings as a decorating element. Fresco is produced painting on a wall's wet plaster, using colors ground up in water or limewater. The Italian word "fresco", which can be translated as "wet", describes this technique. The typical stratigraphy has multiple layers: the substrate, made of bricks or stones, is covered with "arriccio", made of lime plaster and coarse sand, in order to create a uniform surface. The last layer, called "intonaco", made of lime plaster and fine sand, is the only visible layer and is the level where the pigments are applied. The total number of layers may change, in particular it is not uncommon that two or more layers of "intonaco" are present, one over the other, due to successive works.

The basic raw material for a fresco is limestone, that is made of calcium carbonate ($CaCO_3$) and forms a very hard and stable surface that traps the pigments. However frescoes are subject to deterioration due to several agents, such as biological patina or mechanical damages caused by water. By and large the most common cause of deterioration is efflorescence and subflorescence of new formed minerals. A common deterioration mechanism start from the formation of acids when water bonds with anhydrites such as SO_2. The resulting product H_2SO_4 can convert calcium carbonate to gypsum, that is partially soluble in water and forms larger crystals within the "intonaco" layer, causing the fresco to blister and flake off. The final result is the detachment of inner parts of the fresco that could present internal voids or cracks, invisible to the observer.

Infrared thermography has been widely used for the nondestructive testing of works of art, also for frescoes, thanks to its contactless nature. The proposed case studies are two laboratory samples and the investigation of the St. Gottardo Church, an ancient church located in Asolo, in the North-East of Italy. The laboratory samples have known defects located under the surface and are investigated using different heating sources. The inner walls of the St. Gottardo Church are decorated with frescoes depicting various religious themes and show, in some cases, detachments due to the ageing process.

4.5.1 Experimental setup: air heating

The experimental air heating setup has been firstly implemented in a laboratory testing of a fresco sample and then applied to the frescoes of the church. The fresco sample shown in Figure 4.2, named “Stripe” Sample, was manufactured according to the traditional techniques with special attention to the traditional recipes for the plaster preparation and the pigments used for painting. The size is 0.34 x 0.41 x 0.042 m^3. A long vertical crack was created underneath the surface.

Figure 4.2: Fresco specimen, named “Stripe”, made with traditional techniques. The specimen width and height are equal respectively to 0.34 and 0.41 m.

The equipment needed for the active survey consists in a handheld air heater and a thermal camera. The handheld air heater has a nominal power of 3 kW. The thermal camera is a FLIR SC3000, that works in the spectral range from 8 to 9 μm with a declared thermal sensitivity of 20 mK at 30°C, mounting a 20° lens. The spatial resolution is 320 x 240 pixels while the frequency of acquisition has been selected equal to 0.5 Hz.

The active thermography technique that has been applied is divided in three phases. During the first one the observed area, usually rectangular with a size approximately of 0.5 m^2, is delimited with four markers and the camera acquires some thermal images at ambient temperature. The markers allow the identification of the Region Of Interest (ROI) and the matching of the thermal and visible images. This phase is repeated multiple time for the on-site measurement. Inside the church, ten different frescoes of various sizes have been divided into 61 areas of approximately 1.5 m^2. The higher parts have required the use of scaffoldings, as shown in Figure 4.3.

Figure 4.3: The experimental setup includes a FLIR SC3000 thermal camera and one handheld heater having a nominal power of 3 kW.

The second phase consists in heating the area with a handheld air heather for a short time, between one and two minutes. The fan heating guarantees a lower temperature unevenness that can arise e.g. in photothermal heating due to the different absorption coefficient of different surface colours. Great care is taken to avoid the overheating of the materials: during the tests the surface temperature is never increased more than 5 K above the initial temperature. The last part is the recording of thermal images at 0.5 Hz frequency for few minutes after removing the heater, until the surface temperature variation over time is negligible. The last step has been the acquisition of the surface cooling for 5 minutes that are equivalent to 150 images. The final output is a three-dimensional matrix of thermal images, as shown in Figure 4.4.

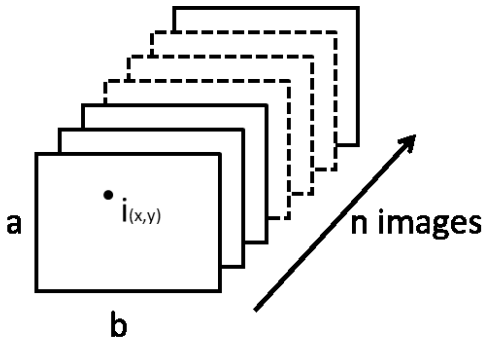

Figure 4.4: A thermal sequence of the cooling phase has size a*b*n pixels, where a*b pixels is the surface area under investigation and n is the number of images in time (typically 150). The temperature profile of the i-th pixel, located in x,y coordinates, runs through the n images.

4.5.2 Experimental setup: comparison of different heating sources

A different fresco sample was created in the laboratories of the Reims University. The specimen, named “Squares”, is a plaster panel sizing 68 x 50 x 5 cm, as shown in Figure 4.5. The sample is divided in twenty sectors, painted with different colors. Under the surface 32 defects have been created, inserting circular inclusions of polystyrene of diameter 1.5 cm and thickness equal to 1 mm. Two defects (#1 and #2) were chosen as a reference case for the comparison of the results.

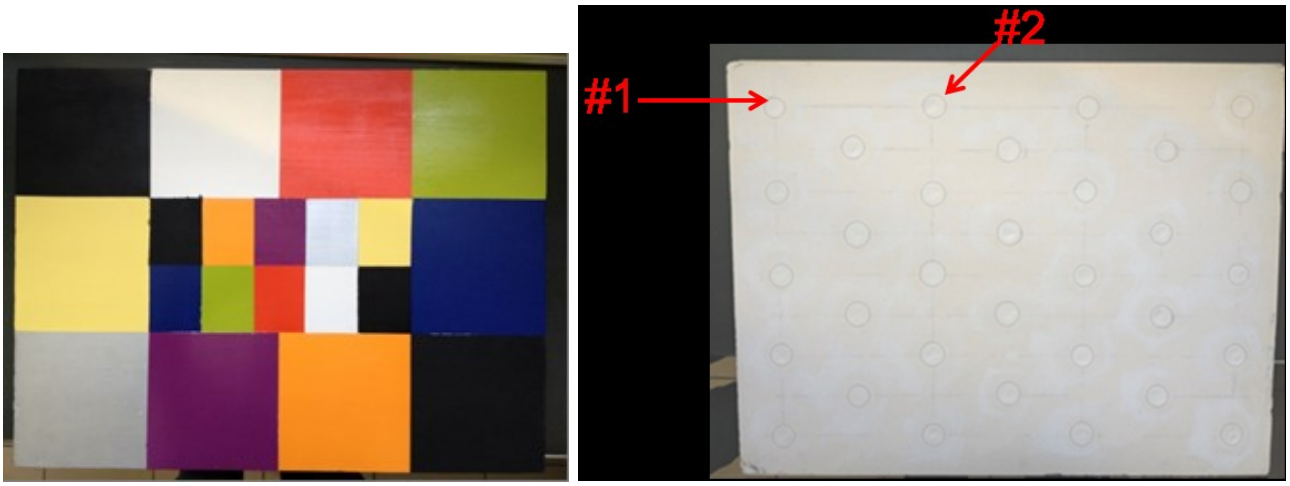

Figure 4.5: Fresco specimen, named “Squares”, painted with different colors (left image). Under the surface 32 circular defects were inserted (right image), two of them were named #1 and #2 respectively and taken as a reference.

Two different heating procedures were applied to the specimen. In the first one a traditional step heating (named Step), delivered by lamps, has been applied. In the second one, a Pseudo Random Binary Signal (PRBS) [24] was sent to the lamps that generated a series of short heating steps turning on and off the lamps. The effect of the heating methods on a reference pixel of the specimen are shown in Figure 4.6, that shows the different temperature increase.

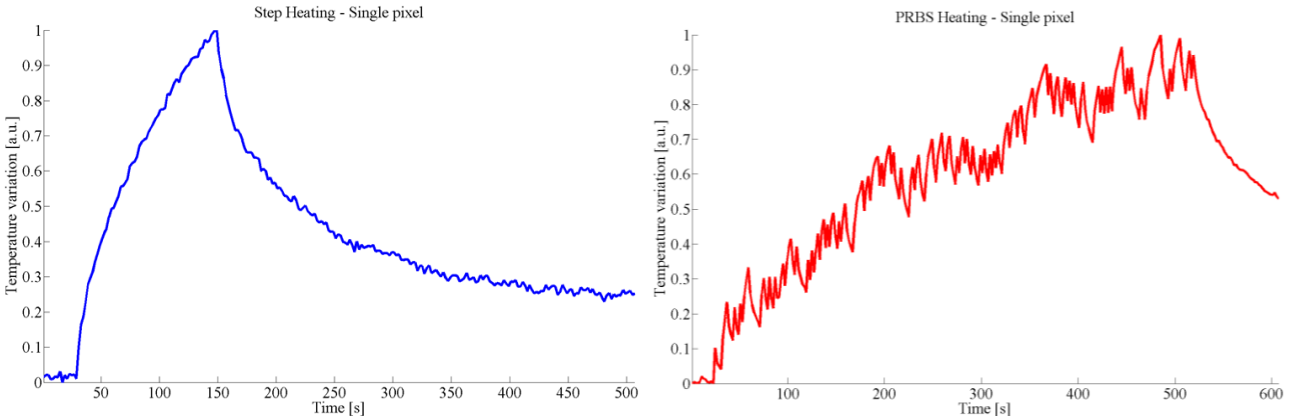

Figure 4.6: Temperature variation over time of a reference pixel submitted to a Step heating (left image) and to a PRBS heating (right image).

The PRBS method has a more difficult practical implementation. Its advantage is the slower and more limited absolute temperature increase, that further reduces the thermal stress on the measured specimen.

4.5.3 Results with air heating: known specimen

The "Stripe" sample was surveyed with the air heating technique. The defect map highlights the defective region (white) against the sound area (black). For each image processing technique, the best results is shown in Figure 4.7.

Defect map

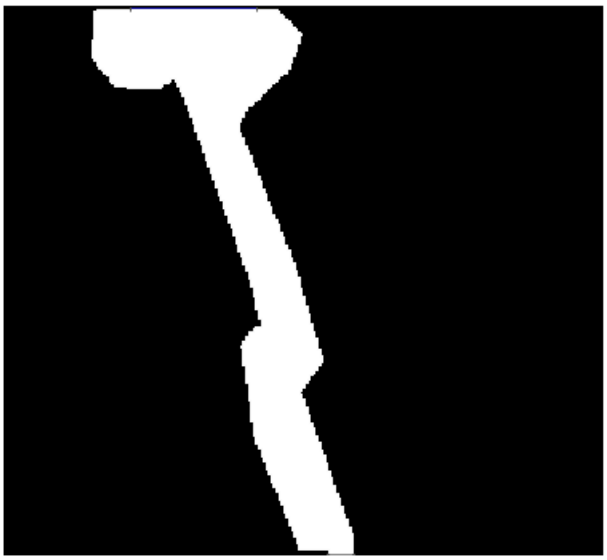

PCT 3rd component

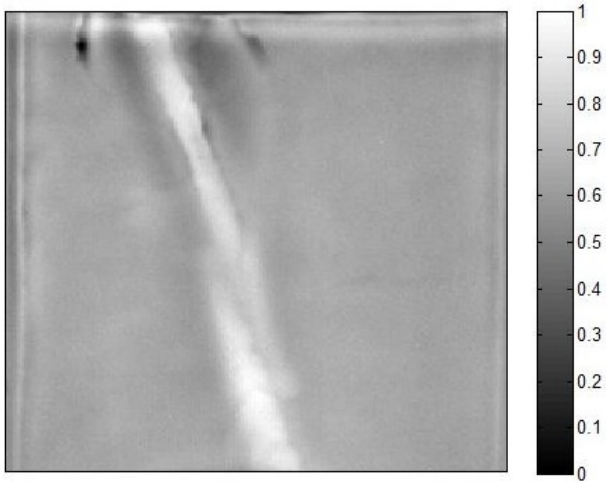

PLST 3rd component

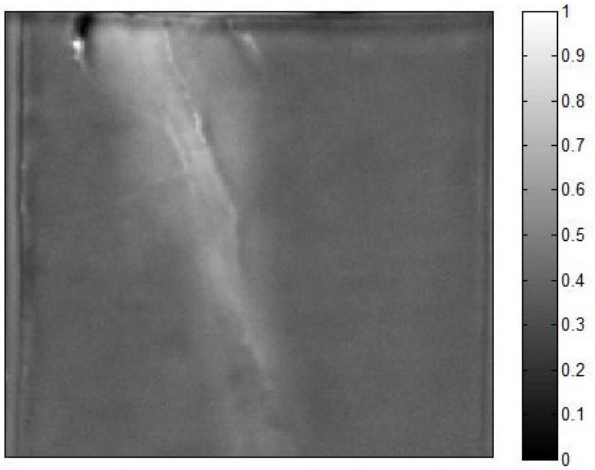

PLSRT 3rd component

TSR 3rd component

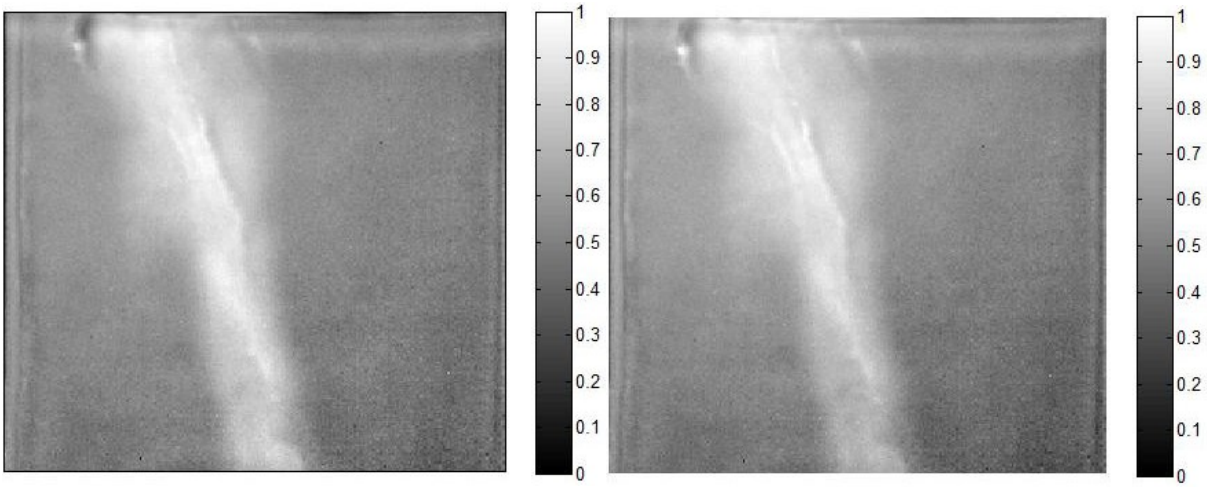

Figure 4.7: Defect map (first image) is white in the defective region and black in the sound one. Results (other images) of defect detection for different image processing algorithms applied to the thermal sequence of the "Stripes" fresco specimen.

To improve the possibility of a comparison between techniques that yield results with very different value scales, all the images have been converted into the same unitary interval and are shown with a grayscale colorbar. It is possible to verify that all the techniques are able to detect and locate correctly the presence of the defect. The best results are obtained with the 3rd component of each algorithm. The presence of different colored stripes does not seem to affect the evaluation; this is of paramount importance when dealing with painted surfaces. For these images also the ROC curves have been traced, showing the profiles of Figure 4.8.

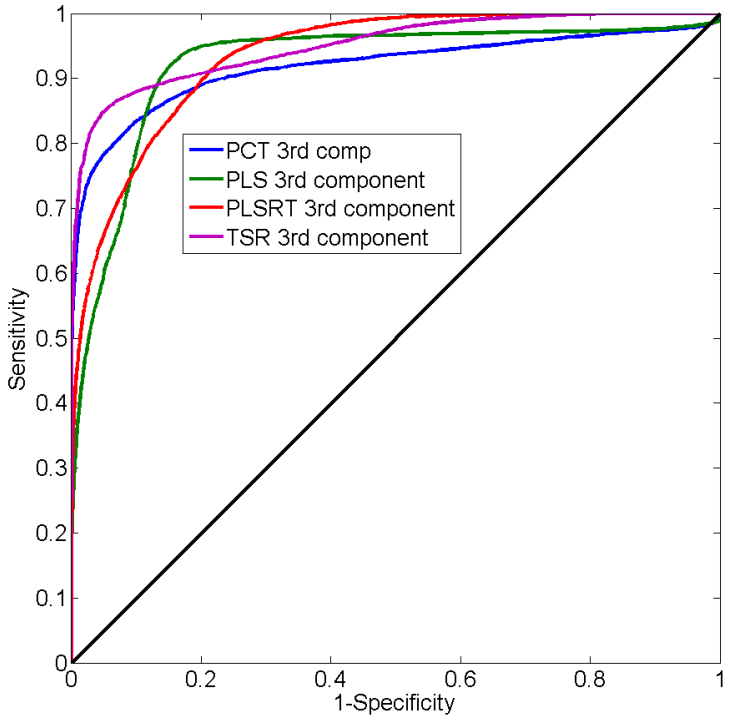

Figure 4.8: ROC curves for the algorithms shown in Figure 4.7.

The profiles of the TSR and PCT have the faster increase, suggesting that they should be more affected by the choice of the threshold. The PLSRT and the PLS profiles show instead higher values on the right side of the curves, implying a lower dependence from the thresholding process. Therefore these last two algorithms could be more suitable for applications where the Golden Standard is not available.

4.5.4 Results of different heating sources: known specimen

The results of different heating sources are shown in Figure 4.9, where the best image for the heating and cooling phase of the PRBS and Step method was selected.

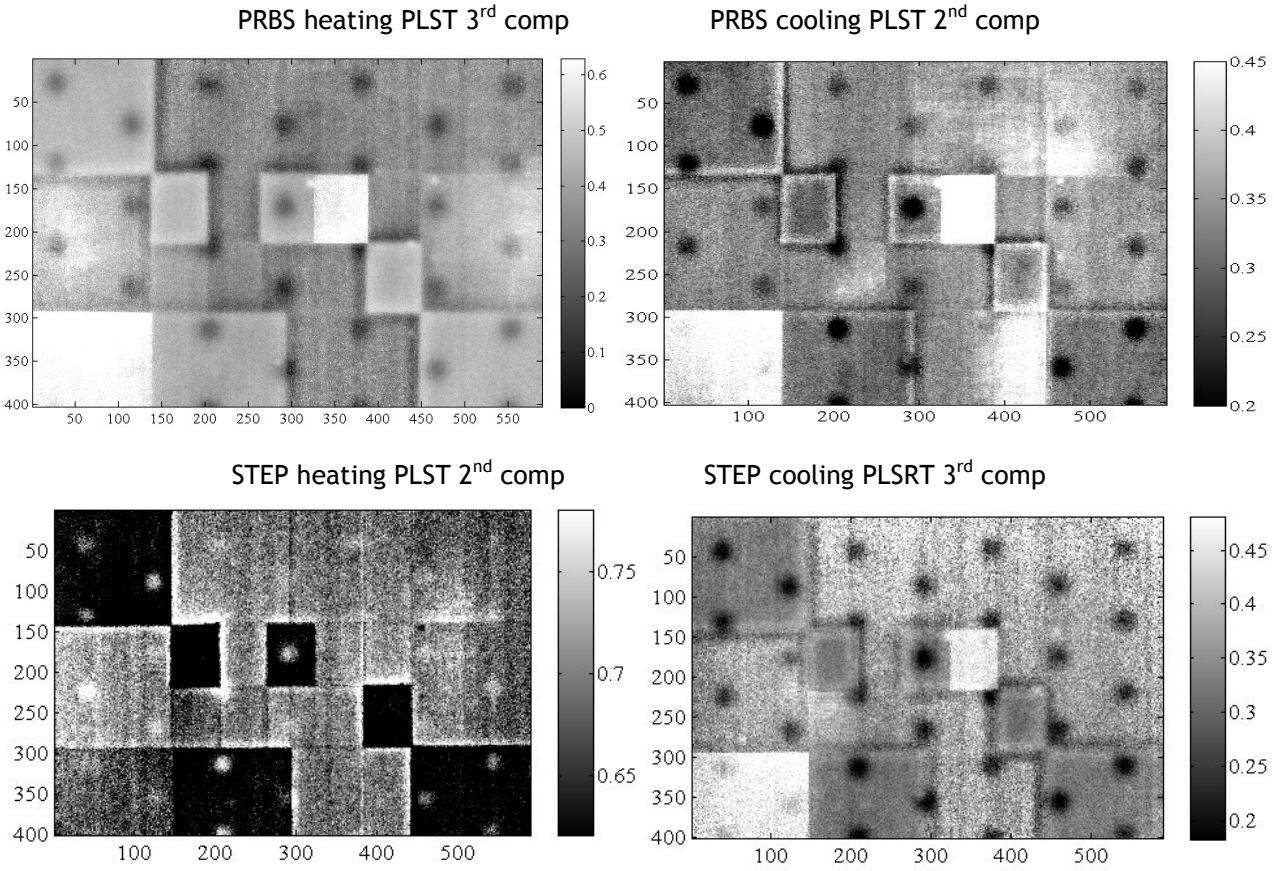

Figure 4.9: Results of the different image processing techniques applied to the "Squares" fresco specimen.

All images show a good defect detection, the most challenging area is the square in the lower left corner. The overall best results seems the one obtained during the cooling phase, and this is confirmed also by the ROC curves of Figure 4.10.

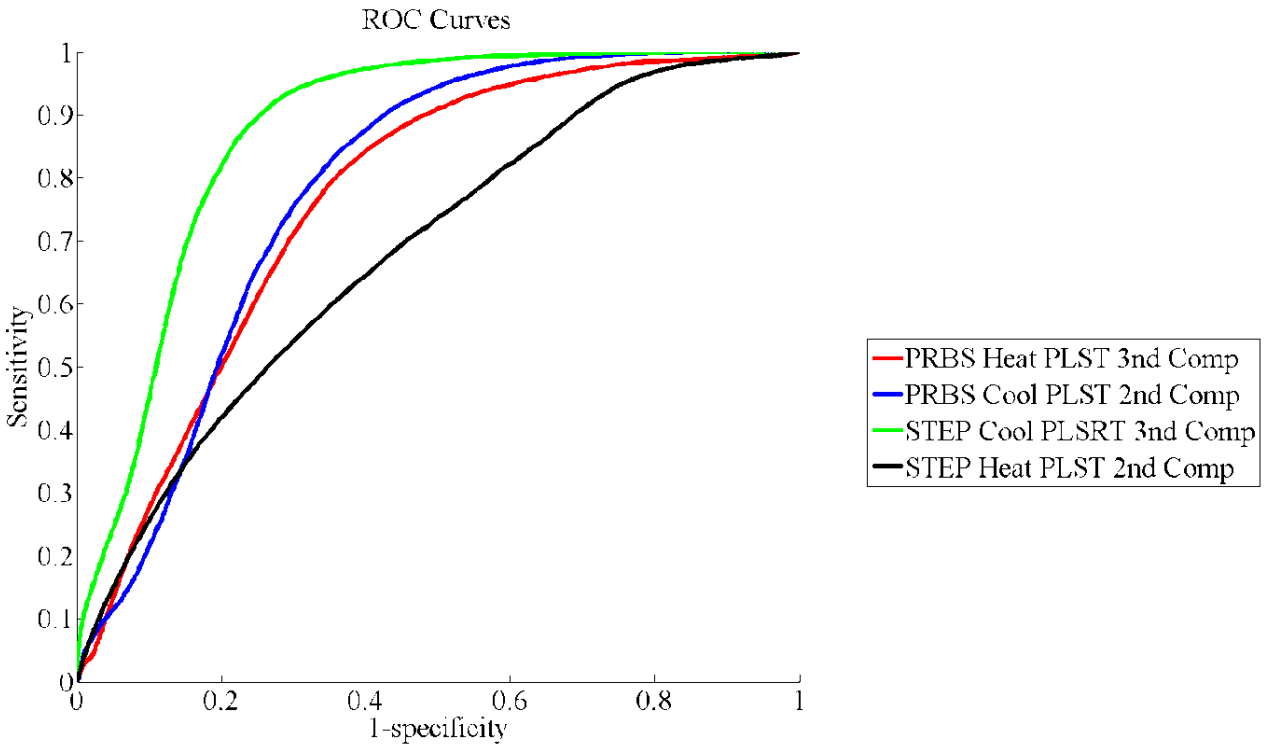

Figure 4.10: ROC curves for the algorithms shown in Figure 4.9.

The curves show the best result for Step cooling, and this is probably due to the rapid and steep temperature variation. While the Step heating seems quite weaker than the cooling one, the PRBS method shows good results both for the heating and cooling, as shown in Table 4.4.

Method	**SNR#1**	**SNR #2**
PRBS heat PLST 3rd comp	18.7	8.4
PRBS cool PLST 2nd comp	13.6	6.9
STEP heat PLST 2nd comp	7.7	-4
STEP cool PLSRT 3rd comp	14.7	8.2

Table 4.4: Signal-to-Noise Ratios for two reference defects (#1 and #2) of the algorithms shown in Figure 4.9.

The reference sound areas have the same size of a defect and are selected in the region between two defects on the same square. The best SNR is obtained with PRBS heating, that in spite of being slightly worse than Step cooling on an average basis, looking at some defects (such as #1) is better.

4.5.5 Results with air heating: on site measurement

The image processing techniques proposed for the specimen testing have been applied also to the thermal sequences acquired in the San Gottardo Church. The results of "Fresco #1" survey are presented in Figure 4.11.

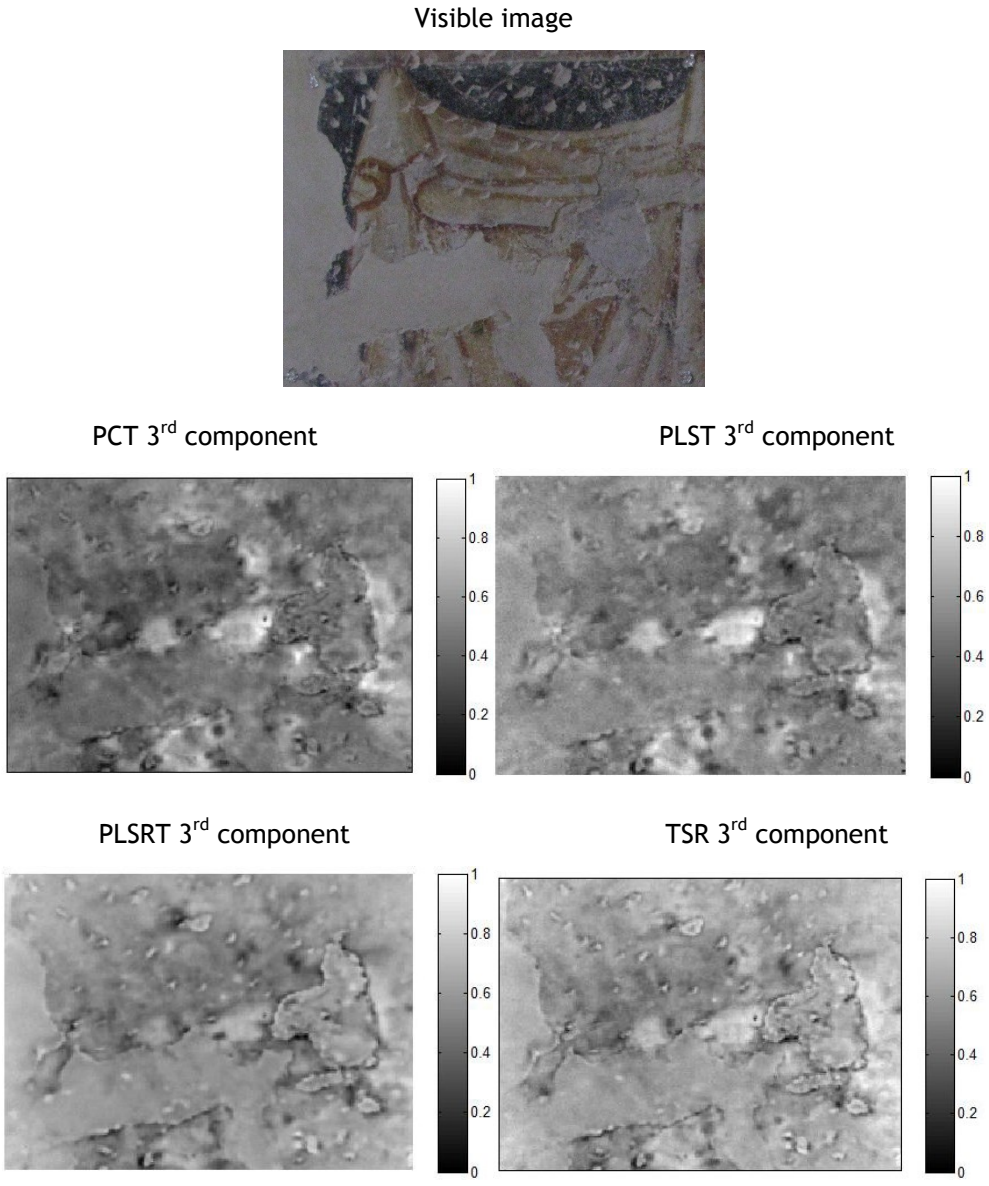

Figure 4.11: Results of defect detection for different image processing algorithms applied to the "Fresco #1" thermal sequence.

All the algorithms highlight different regions of possible detachments that are located mainly on the edges of the renovation interventions, showed in the visible image. It is possible to note that the location of the defect is the same for all the techniques. Multiple "picchiettature" (marks of hammer tapping) are present, denoting that another fresco layer that had been placed over the current fresco had been removed in the past.

These marks are visible in the thermal sequences but they are not indicating a defect. Five algorithms reviewed in the previous section have been applied to the fresco depicting San Gottardo and San Gregorio Magno is of particular interest. It presents, on the right side, a clearly defective area, that could be spotted also with the tapping technique used by professional restorers. At the opposite side of the fresco is present a sound area, that can be used as a reference.

Visible image

Correlated contrast

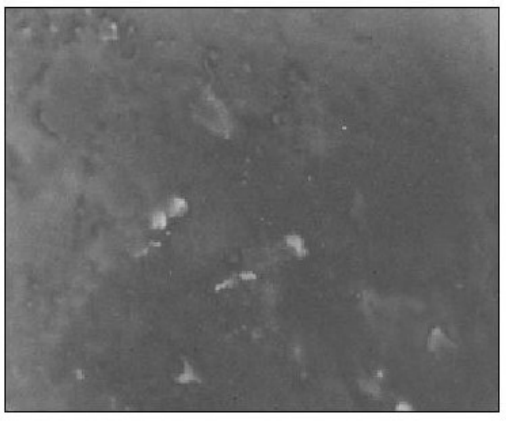

PCT 3rd component

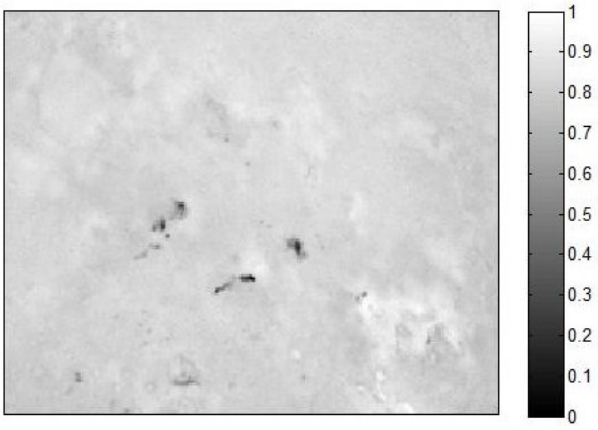

FT – Amplitude – 1st component

FT – Phase – 1st component

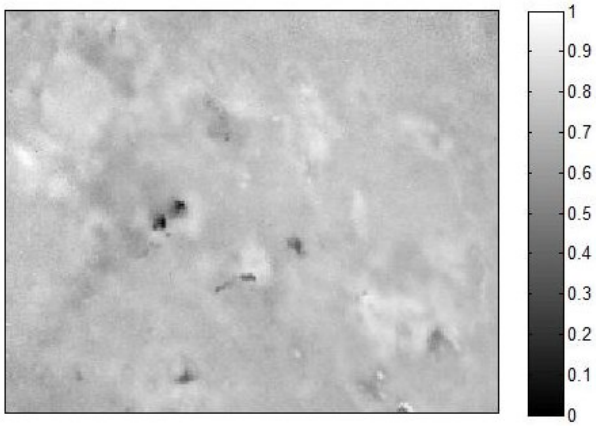

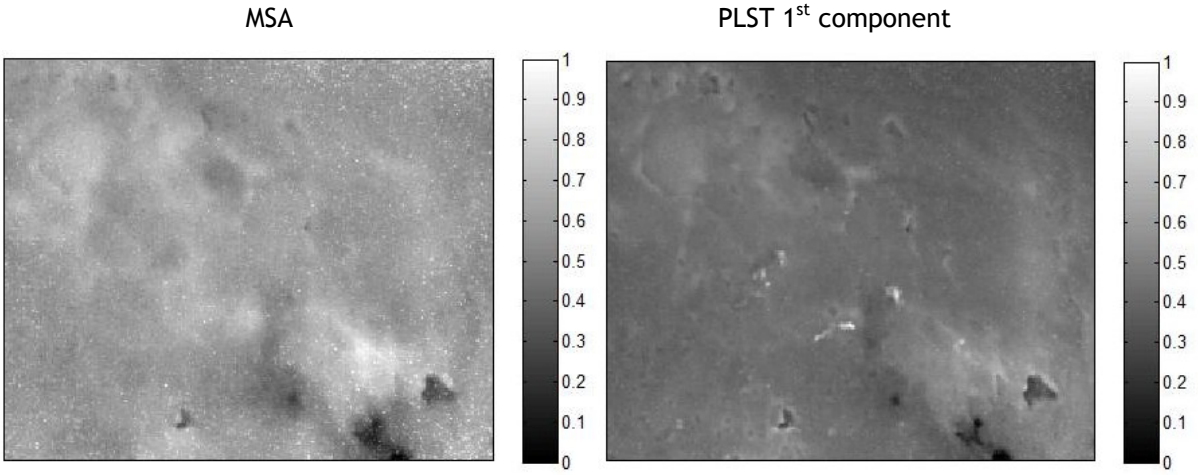

Figure 4.12: Results of the different image processing techniques applied to the San Gottardo and San Gregorio Magno fresco (first image). The region of interest is marked by a polygonal line. The sound area (on the left) is marked by a black circle. The defective area (on the right) is marked by a white circle. All the images show the region of interest highlighted in the visible image and have been converted to grayscale.

The processed images of the previous figure have been cropped and resized to the region of interest evidenced on the visible image with the help of four markers. In this way it is possible to locate correctly the defects within the fresco. One method to compare the algorithms is the calculation of the mean value of the defect and sound area. As shown in the following Table 4.5 the output values of different procedures have a wide oscillation, even after normalization, ranging from values closed to 1 for PCT, FT phase, and MSA, to values lower than 0.5 for correlation.

Algorithm	**Defect area average value**	**Sound area average value**	**Defect - Sound difference value**
Correlated contrast	0.440	0.350	0.090
PCT – 3rd component	0.960	0.851	0.109
FT – Amplitude – 1st component	0.644	0.402	0.242
FT – Phase – 1st component	0.909	0.781	0.128
MSA	0.936	0.648	0.288
PLST – 1st component	0.582	0.465	0.118

Table 4.5: Comparison of defect and sound area values for all the image processing techniques applied. The higher signal value is shown by PCT while the best ratio between defect and sound area is shown by the amplitude image of the 1st component of the Fourier Transform.

Interesting information could be obtained subtracting the average value of the sound area from the average value of the defect area. This is a measure of the detectability of defects, as higher values imply an higher image contrast. The higher differences are obtained with the MSA and with the FT amplitude algorithms, while all other techniques reach similar results.

4.6 References

[1] P. Bison, A. Bortolin, G. Cadelano, G. Ferrarini, F. López, X. Maldague, Comparison of image processing techniques for the on-site evaluation of damaged frescoes, in: Thermosense: Thermal Infrared Applications XXXVI, 2014. doi:10.1117/12.2053782.

[2] P. Bison, A. Bortolin, G. Cadelano, G. Ferrarini, L. Finesso, F. Lopez, X. Maldague, Evaluation of frescoes detachments by partial least square thermography, in: Bordeaux, 2014. doi:10.21611/qirt.2014.109.

[3] G. Cadelano, A. Bortolin, G. Ferrarini, B. Molinas, D. Giantin, P. Zonta, P. Bison, Corrosion Detection in Pipelines Using Infrared Thermography: Experiments and Data Processing Methods, Journal of Nondestructive Evaluation. 35 (2016). doi:10.1007/s10921-016-0365-5.

[4] P. Bison, A. Bortolin, G. Cadelano, G. Ferrarini, L. Finesso, K. Mouhoubi, J.L. Bodnar, Thermographic survey of frescoes with different thermal stimuli: a PLS-based analysis, in: Proceedings of the 2016 International Conference on Quantitative InfraRed Thermography, QIRT Council, 2016. doi:10.21611/qirt.2016.030.

[5] M.T. Klein, C. Ibarra-Castanedo, X.P. Maldague, A. Bendada, A straightforward graphical user interface for basic and advanced signal processing of thermographic infrared sequences, in: Proc. SPIE 6939, Thermosense XXX, 2008. doi:10.1117/12.776781.

[6] X. Maldague, Theory and Practice of Infrared Technology for Nondestructive Testing, 2001.

[7] R. Madding, Emissivity measurement and temperature correction accuracy considerations, in: Thermosense: Thermal Infrared Applications XXI, SPIE, Orlando, 1999.

[8] E. Grinzato, Humidity and air temperature measurement by quantitative infrared thermography, Quantitative InfraRed Thermography Journal. 7 (2010) 55–72. doi:10.3166/qirt.7.55-72.

[9] P. Bison, A. Bortolin, G. Cadelano, G. Ferrarini, K. Furlan, E. Grinzato, Geometrical correction and photogrammetric approach in thermographic inspection of buildings, in: 11th International Conference on Quantitative InfraRed Thermography, Naples, 2012. doi:10.21611/qirt.2012.285.

[10] M.T. Klein, C. Ibarra-Castanedo, A. Bendada, X.P. Maldague, Thermographic signal processing through correlation operators in pulsed thermography, in: Proc. SPIE 6939, Thermosense XXX, 2008. doi:10.1117/12.777002.

[11] N. Rajic, Principal component thermography for flaw contrast enhancement and flaw depth characterisation in composite structures, Composite Structures. 58 (2002) 521–528. doi:10.1016/S0263-8223(02)00161-7.

[12] S. Marinetti, E. Grinzato, P.G. Bison, E. Bozzi, M. Chimenti, G. Pieri, O. Salvetti, Statistical analysis of IR thermographic sequences by PCA, Infrared Physics & Technology. 46 (2004) 85–91. doi:10.1016/j.infrared.2004.03.012.
[13] X. Maldague, F. Galmiche, A. Ziadi, Advances in pulsed phase thermography, Infrared Physics & Technology. 43 (2002) 175–181. doi:10.1016/S1350-4495(02)00138-X.
[14] S.M. Shepard, J.R. Lhota, B.A. Rubadeux, D. Wang, T. Ahmed, Reconstruction and enhancement of active thermographic image sequences, Opt. Eng. 42 (2003) 1337–1342. doi:10.1117/1.1566969.
[15] S.M. Shepard, J. Hou, J.R. Lhota, J.M. Golden, Automated processing of thermographic derivatives for quality assurance, Opt. Eng. 46 (2007) 51008-51008–6. doi:10.1117/1.2741274.
[16] M. Pilla, M.T. Klein, X. Maldague, A. Salerno, New absolute contrast for pulsed thermography, in: Proceedings of the 6th Conference on Quantitative InfraRed Thermography, Zagreb, 2002.
[17] S. Marinetti, L. Finesso, E. Marsilio, Archetypes and principal components of an IR image sequence, Infrared Physics & Technology. 49 (2007) 272–276. doi:10.1016/j.infrared.2006.06.017.
[18] C. Ibarra-Castanedo, A. Bendada, X. Maldague, Thermographic image processing for NDT, in: 2007.
[19] D.L. Balageas, Defense and illustration of time-resolved pulsed thermography for NDE, Quantitative InfraRed Thermography Journal. 9 (2012) 3–32. doi:10.1080/17686733.2012.676902.
[20] H. Wold, Partial Least Squares, in: S. Kotz, N. Johnson (Eds.), Encyclopedia of Statistical Sciences, Wiley, New York, 1985.
[21] The MathWorks, Inc., MATLAB and Statistics Toolbox Release 2012b, The MathWorks, Inc., Natick, Massachusetts, United States., 2012. www.mathworks.com/help/stats/plsregress.html.
[22] F. López, N. Vicente, X. Maldague, C. Ibarra-Castanedo, Multivariate Infrared Signal Processing by Partial Least-Squares Thermography, in: Québec, Canada, 2013.
[23] T. Fawcett, An Introduction to ROC Analysis, Pattern Recogn. Lett. 27 (2006) 861–874. doi:10.1016/j.patrec.2005.10.010.
[24] J.L. Bodnar, J.C. Candorè, J.L. Nicolas, D. Caron, Random photothermal thermography: Principle and examples of applications, in: 10th International Conference on Quantitative InfraRed Thermography, Quèbec, 2010.

5 Measuring heat fluxes in buildings: a cultural heritage perspective

This section describes several devices and methods, based on infrared thermography, to investigate the heat fluxes exchanged through the building envelope and inside the building itself. The described methods and devices are applicable to different building typologies, but in this section a special attention is paid to cultural heritage buildings, that are chosen as a challenging test for this new instruments and procedures.

5.1 Traditional thermographic surveys

A basic thermographic survey of a building consists in an inspection of the building performed by an operator with a thermal camera. The key aspects of the survey are: the localization of building details that may contain interesting information, the collection of thermal images and ancillary measures, the data analysis, and the report creation. While the process may seem straightforward, a more in-depth examination unveils several phases with different activities that must be accomplished to obtain good results. Some basic recommendations are given by the EN 13187 standard [1], that is focused on the thermographic identification of thermal anomalies of the building envelope. A list of the tasks that are necessary to perform an infrared building survey is presented in the following Table 5.1, along with the phases where these task must be accomplished.

Phase	Activities
Planning	Examination of the building blueprints (plans, materials, HVAC system) Choice of the inspection timing Verification of the site availability Check of the climate data Decision on active or passive survey Choice of personnel and instrumentation setup Creation of a survey plan and of a checklist

Execution	Check plan or update with modification Image acquisition and saving Check and saving of places and scheduling of the work plan Acquisition and saving of ancillary data
Processing	Data download and synchronization Correction for environmental parameters Application of image processing algorithms Data storage
Analysis and reporting	Anomalies highlighting Report for trained or untrained people Optimization of the view - Virtual views

Table 5.1: Overview of the main phases and activities necessary to perform a building survey.

The first phase of a building inspection is preliminary to the on-site activities, but it is anyway of paramount importance. A good survey starts well before the executive phase, and mainly consists in collecting available data about the building in order to choose the correct inspection strategy. The building blueprints or any available document (sketches, photographs, models) that describe the building location, orientation, width, height, number of rooms, are the fundamental starting point to estimate the duration of the survey, the personnel required to perform it, and the instrumentation needed. All these parameters have a wide variation range: for instance a wide multi-story building may take up to several days or multiple operators for a complete analysis while a single house may be inspected in less than an hour by a single operator.

Blueprints may give information also about the construction materials of the envelope and on the HVAC system. Both have an impact on the feasibility of the survey and on the choice between a passive inspection and an active one. Thin and light envelopes have faster temperature variation and require a lower time to reach a steady state. An HVAC system may be used to create a difference between inner and outer condition, removing the need of other instrumentation for an active inspection. Its presence may impact on other investigation techniques that frequently are coupled with a thermographic measurement, such as the blower door test or the co-heating test.

Another aspect of the planning that may impact significantly the success of the survey is the availability of the site, both in space and in time terms. The ideal condition, where the operator has free access to the entire site at every hour of the day, is almost never encountered in practical applications. In real cases, two main situations may occur: in the first case the building is under construction or retrofit, so it has no occupants; in the second case the building is in use, so occupants may be present during survey. The presence of occupants is usually a strong limitation to the inspection, as active techniques may be precluded and the time slots for the survey may be significantly reduced. However, their knowledge of the building may be an asset for the localization of the most important issues, especially when they directly request for the survey. An unoccupied building is usually easier to inspect, if the person responsible for the site management is available during the measurements. In all cases, it is necessary to comply with national or local regulations about private property and inspection methods, as infrared thermography may be considered invasive [2].

The site availability in terms of time could need separate considerations for single-shot and for long-term measurement campaigns. In the first case, the analysis of a wall at a certain hour of the day must take into account its thermal inertia and the amount of solar radiation, that may enhance the results of the survey [3] or may limit the obtainable results [4], as described in the next Table 5.2. When planning a long-term campaign, multiple measurement must be taken at different times during the year. A good scheduling process helps to guarantee that the site is analyzed under appropriate environmental conditions. In all cases, flexibility about the inspection timing is a great asset. The freedom of surveying the building at different times can limit the influence of a complex and variable group of elements: the climate.

The interaction between the climate and the building is of paramount importance to determine the results of a thermographic inspection. Several authors investigated the importance of the meteorological conditions: Lehmann et al. [4] noted that the building is seldom (or never) in a steady-state condition and free of disturbing influences. Through measurement on a test building and a sensitivity study based on simulations, the authors investigated the impact of solar irradiation, wind, IR radiation of the environment, and the past outside air temperature, concluding that the behavior of an external wall surface is mainly driven by its structure (wall stratigraphy and materials) and by solar and IR radiation, as their perturbations dies out slowest. Moreover they

underline the importance of the building orientation. De Vijver et al. [5] analyzed several existing guidelines on the thermographic analysis of the building envelope and collected the recommendations in the following Table 5.2, finding in some cases contradicting and vague indications.

Construction type	Light	Medium	Heavy
Solar irradiation	No solar irradiation allowed during 3h prior to investigation [6]	No solar irradiation allowed during 8h prior to investigation [6]	n.d.
	IR possible several h after exposure [4,7]	IR possible 24 h after exposure [4,7]	IR possible 48 h after exposure [4,7]
	IR possible 2-3 h after exposure [8]	IR possible 4-6 h after exposure [8]	IR possible 8 h after exposure [8]
	Not allowed 12 h prior to IR [1,9,10]		
	Structures with high thermal mass need more attention [1,9]		
	Not allowed [11–17]		
Temperature gradient	$\Delta T_s = 0.5\ \Delta T_{e,grad}$ [4,7]	$\Delta T_s = 0.35\ \Delta T_{e,grad}$ [4,7]	$\Delta T_s = 0.2\ \Delta T_{e,grad}$ [4,7]
	$\Delta T_{e,grad}$ low and stable during IR [12]		
	$\Delta T_{e,grad} < 10^{\circ}C$ 24 h prior to IR, $< 5^{\circ}C$ during IR [1,9,14]		
	$\Delta T_{i,grad} < 2^{\circ}C$ during IR [1,9,18]		
	$\Delta T_{e,grad} < 5^{\circ}C$ during IR [1,9,18]		
Precipitation	To avoid [12,16]		
	No influence on IR from small distance [7,19]		
	Wet surface or with snow covered surface not allowed [6,7,19]		
	Makes it impossible to do an IR [17]		
	For roof inspection the roof surface has to be dry [11,12,20]		

Sky radiation	Ideal when fully overcast sky [11,16,19]	
	Covered surface = T_{obj} ~T_{omg} = ideal circumstances [4,13]	
	Important influence on T_{refl} [21]	
Temperature difference inside/outside (ΔT_{i-e})	Insulation defects	Air leakage spots
	ΔT_{i-e} >10°C during 4h prior to IR [22]	ΔT_{i-e} >1.7°C during 4h prior to IR [22]
	ΔT_{i-e} >10°C [12]	ΔT_{i-e} >3°C [12]
	ΔT_{i-e} >10°C [23]	ΔT_{i-e} >5°C [23]
	ΔT_{i-e} >10°C [13]	
	ΔT_{i-e} >3/U (min 5°C) during 24 h prior to IR [10,18]	
	ΔT_{i-e} >15°C during 24 h prior to IR [17,24]	
	ΔT_{i-e} >10-15°C [15,25]	
	ΔT_{i-e} >5°C during 24h prior to IR [1,9,14]	
	ΔT_{i-e} >10°C during 4h prior to IR [6,26]	
	ΔT_{i-e} >10°C (>20°C if possible for U-value determination) [21]	
Wind velocity	Qualitative inspection	Quantitative inspection
	2.7 m s^{-1} [15]	1 (ideal 0.2) m s^{-1} [15]
	5 m s^{-1} [11,23]	
	6.7 m s^{-1} [6,12]	
	3.6 m s^{-1} [22]	
	2 m s^{-1} [4,7,16,17]	

Table 5.2: Overview of the influencing environmental parameters and their limitations [5].

Excluding some major contradictions, it is possible to see that the ideal conditions are similar to a laboratory test: limited or absent impact of the environment and a high and stable temperature difference between the inside and the outside of the building. Obviously this conditions are rarely obtainable in a real case, therefore the authors tried to suggest wider ranges for environmental parameters.

These are general recommendations that should be checked every time on the real buildings, remembering that exceeding these limits may easily bring to unreliable results. In real cases it should be noted that:

- an excess of solar or sky radiation may easily lead, as an example, to a wrong estimation of the insulation properties of the wall, especially if the surface is partially shaded by trees or other buildings

- precipitation can cause thermal signals due to water evaporation, that coupled with an uneven drying process may lead to the individuation of apparent thermal anomalies that in fact are not an issue;

- strong winds may further enhance the phenomenon explained above

- a high temperature difference between outside and inside is instead a threshold level: if the thermal signal is too low, the risk is missing details or even not obtaining any result.

After the analysis of the building type, its availability, and its location, it is possible to choose whether an active, passive, or combined active and passive survey should be performed. In case of a long-term survey this choice may be changed during the course of the campaign, but for single-shot inspections the decision is definitive. When dealing with an active thermographic measurement the request of additional permissions may be necessary, particularly for heritage building, and the time needed to obtain this permissions should be taken into account.

The next step is the choice of the personnel and of the instrumentation setup. As already mentioned, a wide multi-story building may require an inspection team of different people, that is usually necessary also in the case of an active survey. It should be noted that while the operators that acquire the thermal images must be trained and preferably expert, the other components of the team may have little or any thermographic experience if they are only acting as a support to the principal inspector. Active surveys frequently require the use of bulky and heavy instruments, therefore their movement both from the laboratory to the site and between the different rooms of the site should be carefully planned. Moreover the thermographic inspection could be integrated with other building inspection activities, that may require specific personnel and dedicated instruments.

The last activity for the preliminary phase is the creation of a survey plan, accompanied by a checklist. The survey plan should include all the expected activities with their forecasted duration, detailing also the spaces of the inspection. It is also important to assign to each operator its role and its activities, in order to increase efficiency and accountability. The checklist is complimentary to the survey plan, and includes firstly a list of all the instruments that are used in the inspection. The presence of the correct instrumentation must be checked at least two times: before reaching the inspection site and before leaving it after the measurement. The other part of the checklist is the planned activity list, to avoid the risk of missing elements during the survey. The checklist could be combined with existing ones, dedicated for example to global building inspections [27] or blower door testing [28].

The execution of the survey should follow as much as possible the planned activity list. Obviously, in practical cases it is sometimes necessary to make some adjustments and adaptations to the original plan. Typical unforeseen events such as rapid changes in climatic conditions, malfunctioning of the instruments, temporary unavailability of the rooms, should be taken into account. All these occurrences may cause delays or changes of plan, and this issue must be tackled updating the survey plan and listing all the modifications adopted, to avoid misunderstandings during the successive analysis phase.

The basic activity during a thermographic inspection is the acquisition of thermal images. The correct localization of the acquired images is paramount for the analysis phase, therefore coupling a photograph to the thermal image is the best practice and should be done whenever possible. Another strategy to avoid ambiguities is writing on a building sketch the exact location where the image is taken. The time information could be retrieved by the electronic file containing the image. In case of measurement that collects a high number of thermograms, a backup of the acquired files should be performed at regular time intervals (e.g. few hours) to avoid any loss of data. Taking small breaks between the acquisition of images allows not only to backup data but also to verify if the survey plan is followed correctly. Another aspect of the inspection is the collection of ancillary data, i.e. ambient temperature, relative humidity, emissivity of the observed surfaces. These variables should be registered along with the thermal images, whenever necessary on the basis of the experience of the operator. If possible, the operator should set directly on-site the parameters on the thermal camera, saving time in the processing phase; in all cases, the values should be recorded. The best

recording mode should be chosen by the operator in order to facilitate the following data analysis; as a general recommendation it should be checked that all the instruments used for the survey are set to the same time and, in case of timed sequences, have a compatible framerate.

The data processing phase should be always performed briefly after the inspection. In case of long-term campaigns, multiple data analysis stages are executed but it is preferable to analyze the images as close as possible to their acquisition, to simplify the localization inside the building by the operator. The first step is the download of the data (thermal images and ancillary ones) and the synchronization of data coming from different sources. This allows to correct the thermal images with the environmental and emissivity data collected on-site, if this adjustment has not been applied during the measurement. The modification of thermal images is typically performed with the dedicated software given by the thermal camera manufacturer, that usually allows the user to save the corresponding temperature maps in a format compatible with the most common image analysis software. A common post-processing tool is Matlab, that includes dedicated routines and that allows the user to create specific algorithms, such as the IR-View software [29] that is a powerful instrument to analyze thermal images and sequences. All the image processing methods discussed in this document were performed in Matlab environment. The final part of the processing data is organizing the storage. This is crucial especially for long term campaigns, where data may be recalled months or even years after the on-site inspection: an ordered file system may save a great amount of time.

After the processing, the obtained data could be analyzed and disclosed into a report. The first goal is usually drawing attention to anomalous regions or details, that are highlighted by the processing phase. In this case the use of markers on the thermal image and the coupling of the thermal and visible images is the best strategy to underline the regions of interest. All the results should be included into a report, that should contain the building sketches, the survey plan, the applied data processing techniques, and the obtained results. A distinction should be made when reporting for trained or untrained people: in the last case a general introduction on infrared thermography and on the interpretation of thermal images should be included. Moreover the results should be discussed in a more detailed way, without leaving any possibility of misinterpretation due to a reduced knowledge of the subject. A great help is given by

the use of virtual views, such as the ones shown in Section 5.3, where the building model immediately identifies the geometrical elements of the thermal image. A more user friendly experience is given by embedding the thermal maps inside the most common virtual reality representations, such as Google Maps or YouTube 360 Videos, that allow an immersive view of the analyzed building.

5.2 Innovative thermographic surveys: the aIRview and IRpano systems

Some of the activities described in the previous section define some practical limits to the performance of building surveys. The physical limitations, such as climate condition or building structure and orientation, are intrinsic to the measurement technique and cannot be overcome. On the other side several data acquisition and processing activities, that are time consuming and prone to human errors due to the repetitiveness of the tasks, could be significantly improved. On this basis, a new thermographic device is proposed with the aim of reducing the survey and image process duration and complexity, decreasing the training level required to the operator, improving the overall accuracy, facilitating the dissemination of the obtained results. Both the IRpano system, described in Section 5.2.1 (description taken from [30]), and the aIRview system, described in Section 5.2.3, are aimed to automatically acquire and process thermal images, increase the measurement accuracy, facilitate the representation of the obtained results. Moreover, the systems make possible to perform time lapsed measurement, organizing campaign that could last multiple days [31] with the acquisition of thermal sequences.

5.2.1 IRpano system

The IRpano device was created to perform fast infrared building surveys with high spatial resolution and limited costs. Its main goal is the automatic creation of panoramic thermal images inside closed environments. IRpano is composed by different devices available on the market, having appropriate technical specifications. The main sensor is a thermal camera, having at least a sensor size of 320 x 240 pixels and a NETD value equal or lower than 50 mK. The first parameter was chosen to limit the costs of the camera while maintaining a sufficient level of spatial resolution. Also the thermal NETD value, that is a fundamental parameter while executing building surveys, was selected as a compromise between the lowest possible value and the cost parameter.

Moreover, the camera needs to be remotely controlled and to have a compact layout. These characteristics are required for the integration of the camera on a pan tilt unit. The chosen camera is FLIR A320, but the system is flexible enough to consider alternatives that have the minimum requirements. Another sensor is a compact photographic camera, embedded in an android based smartphone. Both cameras are connected through a router to a computer.

The cameras are mounted on a Pan Tilt unit, that is typically connected to the computer with a serial port. Several devices available on the market have been tested, analyzing spatial resolution, repeatability of positioning, payload, and compactness. The first choice was a Directed Perception D46 Pan Tilt Unit having a pan range of 318 degrees, a tilt range of 111 degrees, and a position resolution of 0.003 degrees. The revolution speed could be higher with other models but would be anyway limited by the infrared camera speed. The overall data acquisition speed is a fundamental parameter, that must be compatible with the investigated physical phenomena. In order to compete with a single shot thermographic image, a complete scan of a room should take a small enough time to validate the assumption of an instantaneous measurement. The choice of the Pan Tilt unit influences also the selection of the thermal camera lens. A slower Pan Tilt, that implies a small number of images to perform a fast scan, could be compensated choosing a wider lens. This choice has a negative impact on the final spatial resolution of the thermal image and implies also a more difficult correction of the lens distortion. On the other side, a closer lens increases the number of movements required for the Pan Tilt to complete a scan of the room, forcing the selection of a faster moving unit.

One of the main issues in infrared thermography is the measurement of absolute temperature. For this reason, IRpano is connected to the IRpsicro device [32] for a continuous temperature calibration. The IRpsicro device is a small cylinder open on one side, made with a low thickness metal. The choice of its material and shape are pointed to decrease the time needed by the device to reach the thermal equilibrium with the surrounding air. The exterior of IRpsicro is highly reflective and a reflective frame is placed around the open side. A calibrated platinum RTD sensor (accuracy ± 0.1 °C at 20°C) is embedded to the device and measures its temperature. The obtained value is communicated in real time to the central processing unit. When IRpsicro is focused by the thermal camera it could be considered as a blackbody reference: the temperature value obtained by the camera is compared to the one read by the RTD sensor, enhancing

the absolute temperature measurement. A scheme of the device with the connection between the different instruments is shown in Figure 5.1.

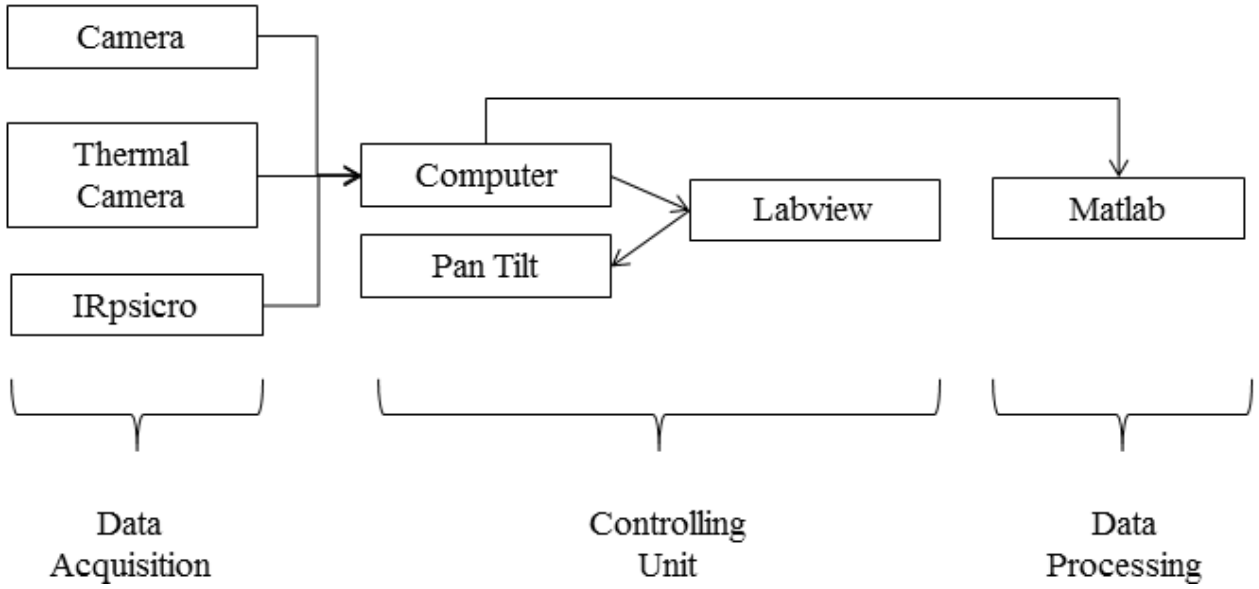

Figure 5.1: IRpano scheme and architecture. The data are acquired by the cameras and the IRpsicro device. A central processing unit is dedicated to synchronization between the pan tilt unit and the data acquisition devices. A custom software is designed to process the data and display the results in real time.

The computer is executing Matlab and Labview custom scripts. The Labview software is controlling the pan tilt unit, acquiring both the thermal and visible images with the possibility to modify the camera focus and the acquisition framerate. The Labview environment allows to synchronize and integrate the data coming from different sensors into a single acquisition framework. The Matlab script is executed at the end of each scan and creates the thermal and visible panoramic images that are sent to the webserver. Matlab was selected because it contains several basic routines for image processing and manipulations and it allows to create highly customizable scripts.

The computer is executing Matlab and Labview custom scripts. The Labview software is controlling the pan tilt unit, acquiring both the thermal and visible images with the possibility to modify the camera focus and the acquisition framerate. The Labview environment allows to synchronize and integrate the data coming from different sensors into a single acquisition framework. The Matlab script is executed at the end of each scan and creates the thermal and visible panoramic images that are sent to the webserver. Matlab was selected because it contains several basic routines for image processing and manipulations and it allows to create highly customizable scripts.

5.2.2 IRpano method

The goal of the IRpano device is performing a full thermographic and visible panoramic scan of a building in a short time. The devices commonly used to create panoramic photographs rely typically on the use of multiple cameras installed on a single mounting system [33]. This approach would be unpractical for thermographic cameras, not only for the cost of the devices but also for the difficulty of measuring temperatures accurately using different sensors. For these reasons the best option available to acquire multiple thermal images is using a single thermographic camera mounted on a pan-tilt unit. A simple technical solution to obtain also visible images is coupling a photographic camera on the same pan-tilt, taking care that photographs need an illuminated ambient, while the infrared camera could work also in dark environments.

The scanning procedure starts with the positioning of the IRpano device on a predetermined spot inside the ambient, usually in the middle of the room. For wide rooms, multiple positions could be required in order to cover all the surfaces. The horizontal and vertical alignment of the pan tilt head is manually checked with a level. When the starting command is sent through the Labview script, the thermal camera performs a non-uniformity correction. Then the pan-tilt unit moves the cameras along a sequence of presets, calculated to sweep the maximum area allowed by the pan-tilt constraints. The pan tilt head moves on a serpentine path, alternating vertical lines from top to bottom and vice versa. The preset positions on the tilt axis and on the pan axis depends on the system configuration, as described above. The total number of acquired images is the product of the presets on the tilt axis and on the pan axis. Typically the number of images exceeds 100, both for the visible and infrared range. In the basic procedure of building surveys, the correct temperature of every pixel is automatically calculated considering the surfaces as Lambertian emitters with emissivity equal to 0.90, typical of the investigated objects [34]. In advanced cases, an a posteriori emissivity correction could be implemented with information coming from the photographic panorama, as described below. At the end of the scan, all the images are sent from the Labview script to the Matlab environment in order to create panoramic views. The procedure workflow is schematized in the following Figure 5.2.

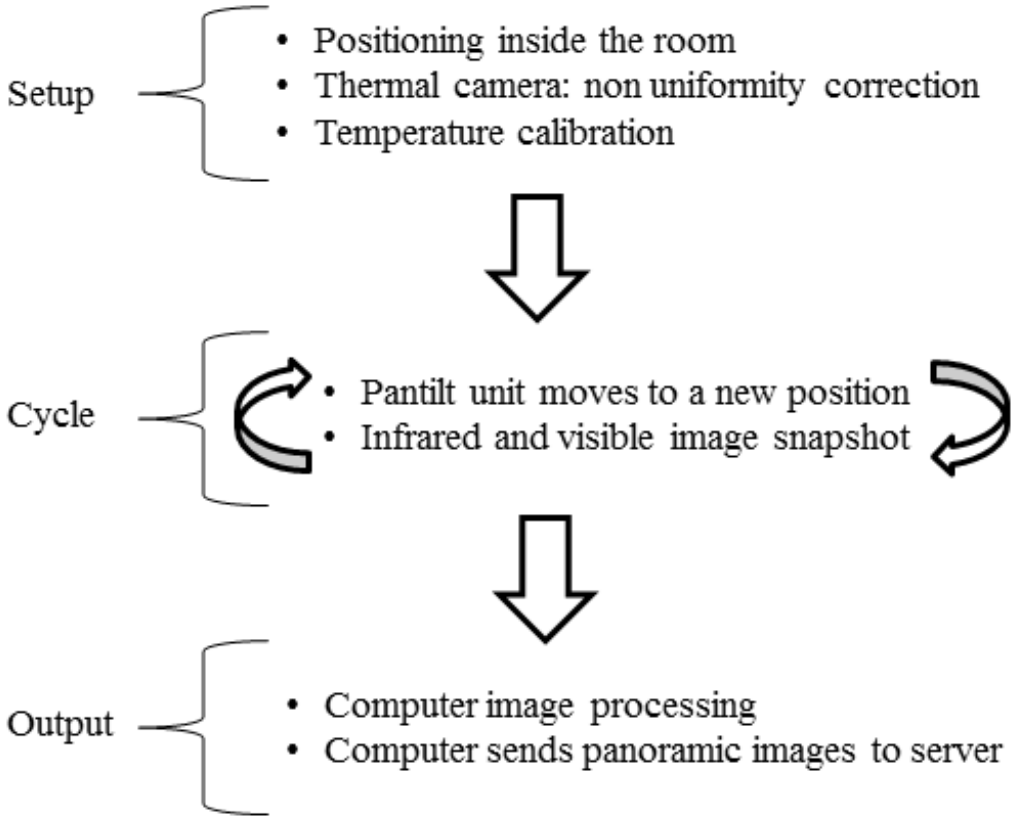

Figure 5.2: IRpano data acquisition and processing routine. After the preliminary setup, the pan tilt unit moves the cameras through all the programmed scanning positions. At the end, the multiple images are post-processed to obtain a mosaicked panorama that is available online.

Thermal images mosaicking has several technical and physical obstacles, if compared to photographs mosaicking: thermal cameras have very low spatial resolution and thermal images are frequently characterized by low contrast in case of isothermal conditions of the object in the scene. These factors make unfeasible the common mosaicking techniques based on segmentation and automatic features extraction. Therefore another methodology is chosen, based on the a priori knowledge of the pan and tilt angles and on the geometrical calibration of the camera [35] The repeatability of the image positioning is assured by the Pan Tilt specifications.

The blending of overlapping regions is handled with a weighted method, described as linear transition model [36]. When two images A and B are adjacent, analyzing at first the case of a row, the temperature value *T* of a *i-th* pixel having *X* coordinate is calculated with the following equation:

$$T_i = \frac{X_{max} - X_i}{X_{max} - X_{min}} * T_{Ai} + (1 - \frac{X_{max} - X_i}{X_{max} - X_{min}}) * T_{Bi} \qquad (5.12)$$

where X_{max} and X_{min} are respectively the highest and lowest X values in the overlapping region. The same applies, with vertical coordinates, when the vertical mosaicking is performed.

The final result is an equirectangular panorama, as shown in the next figure where the pixel height represents the tilt range while the width represents the pan range. In full equirectangular images, the width to height ratio is equal to 2.

The temperature scale of the image is automatically generated based on the image variance. The center of the scale is the mean value of the image while the maximum and the minimum are chosen as the mean value plus or minus one standard deviation.

The same mosaicking procedure is applied to the photographic images. Thanks to the application of the same procedure, the obtained panoramic image could be easily matched to the corresponding thermographic value. This makes possible to easily localize the thermal anomalies of the thermographic survey on the building structure. Moreover, it allows to trace surfaces with different optical characteristics and to consequently adjust the emissivity parameter over the selected area.

The raw data and the processed images are finally published on a web server, in order to make data easily available also to remote user. The original images could be integrated inside a virtual visit of the building through the Google Street View architecture. Another available option is the use of standalone web viewer panorama software [37]. An even more immersive view is given by the integration with the YouTube 360 video platform, where virtual reality devices (e.g. VR headsets coupled with smartphones) could be used.

5.2.3 aIRview system

The aim of the aIRview system is extending the number of physical parameters that can be measured by infrared thermography. The method relies on a vertical grid of special targets that are placed on a support structure with a free to choose spacing interval between each target (typically lower than 0.5 m). The total grid size may vary from 1 to 25 m^2, depending on the application, and the use of multiple small grids with a successive mosaicking operation may replace the larger ones. The grids are usually rectangular, but may have different layouts, when dealing with curved surfaces such as vaulted ceilings or niches.

The targets may act in two ways: as a geometrical reference or as a physical reference. In the first case, they facilitate the geometrical reconstruction process of the surface as the known spatial coordinates of the targets are exploited as control points of image transformations. In the second and most important case, they allow the estimation of thermophysical parameters such as air temperature, reflected temperature, and air velocity. Each target is divided in four different sections: a small piece of tissue, that is partially immersed in a small case containing distilled water; a thin plastic layer, covered with a reflective material; two thin plastic layers, respectively black and white colored. These sections are arranged in a checkerboard way as each part is placed on a quarter. The different parts are designed to accomplish a specific function. The black and white areas are able to reach quickly a thermal equilibrium with the surrounding air and therefore they allow the measurement of air temperature. The emissivity value of the target is known and high, also for different viewing angles, guaranteeing an accurate measurement. The reflective sector is made of multifaceted polished aluminum (very low emissivity value) enabling the measurement of the environmental reflected temperature on the grid plane. The wet tissue is a reference evaporating surface, that is used in coordination with another psychrometric device (IRpsicro [32]) that acts a wet bulb temperature reference. The known calibration of the materials allows, through the use of psychrometric functions [38], the measurement of the air velocity.

The measurement is performed placing the grid in the field of view of the IRpano device. Afterwards, the targets may be automatically or semi-automatically identified during the image processing phase, based on the knowledge of the grid location in the room. For each target, the value of each physical properties measured is stored along with its location and then reassembled through an interpolating process to create a map. The output is therefore a series of images, representing the distribution over the grid of the measured parameter.

The obtained results increase significantly the role of infrared thermography for microclimatic monitoring, allowing to measure multiple parameters with a single device. Moreover, the collected data are a valid support for numerical fluid dynamics models, both in the design and in the verification stage.

5.2.4 Case studies

The case studies described in this chapter are relative to cultural heritage buildings. The proposed survey techniques are not limited to this kind of building, as they could be applied with minimum adaptations to any typology of edifice. The cultural heritage building were chosen due to their particularly challenging nature, that could immediately highlight any weakness of the suggested methods. The complete list of the surveyed buildings is shown in the following Table 5.3.

Location	Building type	Survey techniques and objectives	Literature Reference
Saint Gottardo Church, Asolo (TV)	Medium size church	Passive thermography: anomalies, hidden structures, moisture Active thermography: anomalies, hidden structures, detachments, moisture Active thermography: works of art	[39–41]
Novalesa Abbey – Saint Eldrad's Chapel, Novalesa (TO)	Small church	Timed thermography: anomalies, moisture	[31]
St. Vito alla Rivera Church, L'Aquila (AQ)	Medium size church	Passive thermography: anomalies, structures, detachments, moisture, microclimatic analysis Active thermography: anomalies, hidden structures, detachments, moisture	[42,43]
Padri Serviti Convent, Koper (SLO)	Wide complex (church and cloister)	Active thermography: anomalies, hidden structures, brick detection, detachments	[30]

Table 5.3: List of heritage building surveyed with infrared thermography.

The Saint Gottardo Church (Figure 5.3) is located in Asolo, in the north-east of Italy, and was probably built during the XIII century. It is decorated with frescoes of medieval style

on large portions of the inner walls, unfortunately showing large problems of conservation and detachments.

Figure 5.3: Front view (left) and side wiev (right) of the San Gottardo Church in Asolo (TV).

The documents on the church are very poor and very few is known about its construction, therefore it was interesting to know as much as possible on the inner structure of the building, especially to drive the restoration activity of the structural part of the church.

The Saint Vito alla Rivera Church, that dates back to the XII century, is located in the historical center of L'Aquila, in front of the “Fontana delle 99 Cannelle”. The church has been damaged by the 2009 earthquake, especially in the facade and in the roof, as shown in Figure 5.4.

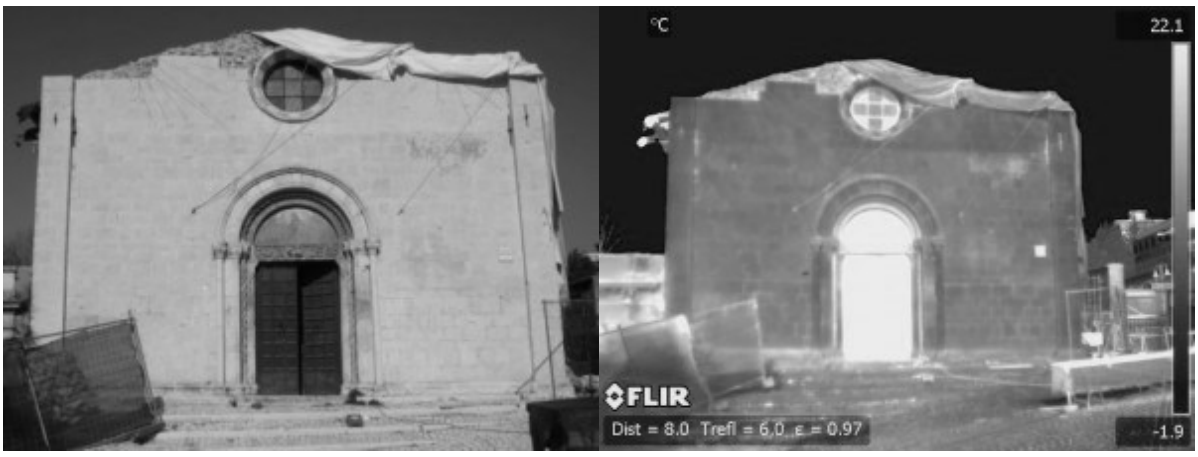

Figure 5.4: Photograph (left) and thermal image (right) of the San Vito alla Rivera Church (located in L’Aquila) during the restoration works after the 2009 earthquake.

The St. Eldrad’s Chapel dates back to the X or XI century, and it is part of the Abbey of Novalesa complex, located about 60 km West of Turin, on the Italian border with France. The structure is not easily accessible and measures 8x5.8x3 meters inside.

Figure 5.5: Front view (left) and interior view (right) of the St. Eldrad's Chapel in Novalesa (TO).

The interior walls and ceiling (Figure 5.5) are entirely adorned with mural paintings that go back to the second half of the XI century. The decorations were executed by means of the fresco technique, and portray religious themes and the story of St. Nicholas and St. Eldrad. It has been testified by art historians that these beautiful frescoes did not suffered any particular problem of conservation since their painting until modern times. Indeed, after recent works, severe damage began to appear, mainly on the lower side of the southern wall. Documents regarding latest years are not exhaustive and sketchy, but it is possible to deduce that some restoration occurred. The plaster layer of the outer wall has been removed from all the surfaces. Moreover a window on the South side that was closed in ancient times was opened. The hallmark shape of the boundaries of the ruined areas and the extensive presence of efflorescence could be related to wall moisture phenomena, but the source of the water and the reason why the wall facing south is the most damaged one are unknown.

The Padri Serviti Convent, shown in Figure 5.6, is located in the historical center of Koper (Slovenia). The construction of the building started in the XV century but several modifications were performed until the XVIII century.

Figure 5.6: Front view of the Padri Serviti convent located in Koper (SLO).

After being a convent, the structure was modified to became the city hospital in the XIX century. After its closing at the end of the XX century, the building was abandoned and it is now under study for a retrofit intervention.

5.3 Measurement of surface temperature distribution

The measurement of surface temperature distribution is the most common practical application of a thermal camera. It may be performed on the inner or the outer surfaces of the building, in a manual or automatic way, and during an active or passive survey. The main goals is finding thermal anomalies, that could indicate the presence of hidden or unknown structures, detachments, moisture. The images of the following subsections illustrate some findings. It is worth noting that, while an active survey is theoretically always better than a passive one due to signal enhancement, in several cases the passive inspection is sufficient to investigate the building status.

5.3.1 Passive thermography

The following two examples are taken from the indoor and outdoor investigation of the St. Gottardo Church. Figure 5.7 shows the vault of the apse and from the thermal image it is possible to determine the structure of the ceiling, that differs significantly from the other vaults of the church. The thermal signal due to different materials is clearly visible even under the plaster layer. This kind of images are useful to investigate hidden structures, assessing their integrity.

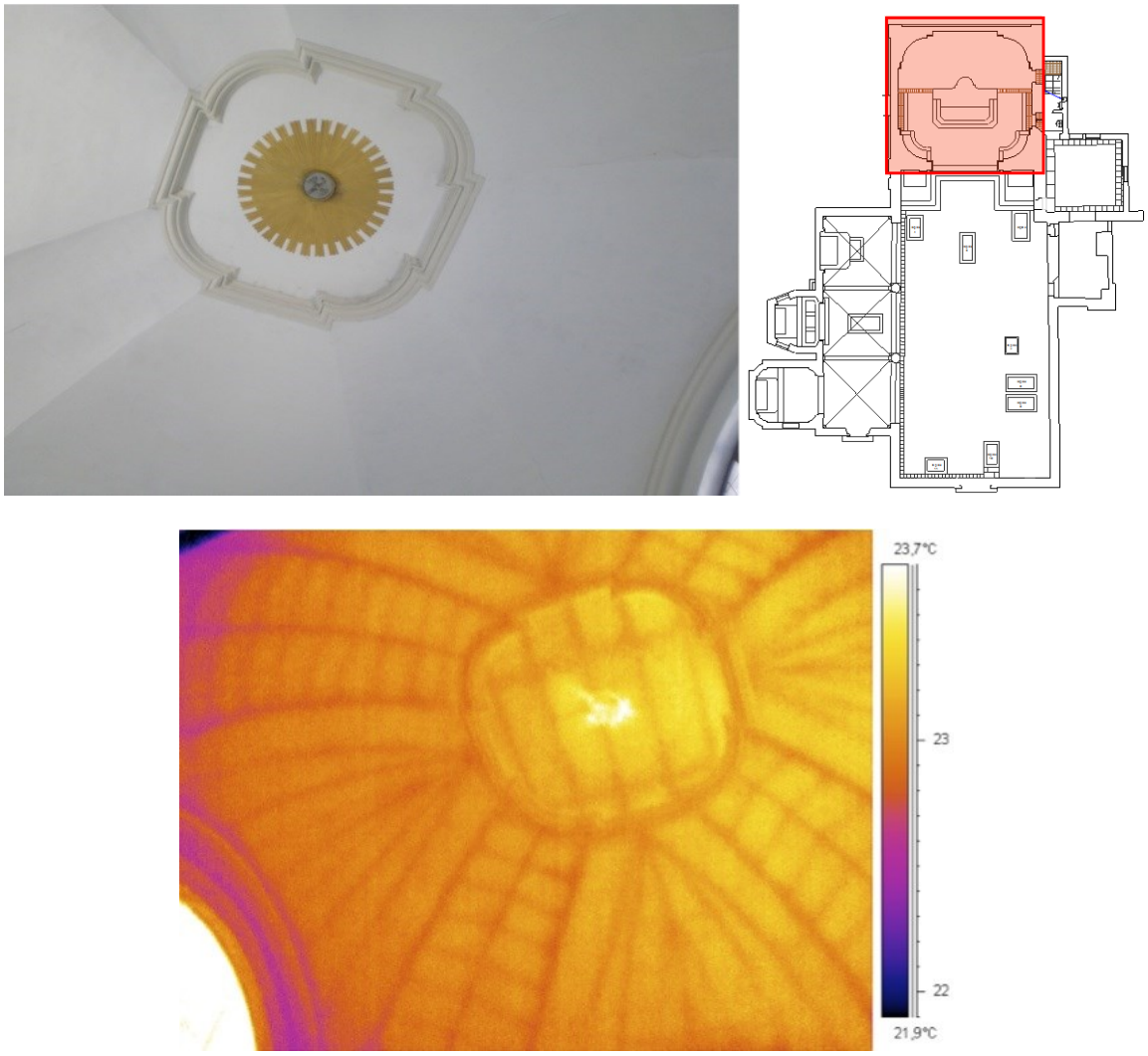

Figure 5.7: Photograph (left, top) of the ceiling vault of the St. Gottardo church apse. Drawing (right, top) of the church, where the apse is identified by the red square. Thermal image (bottom) showing the ribs system supporting the vault ceiling that appears as a lower temperature imprint.

The next Figure 5.8 displays the external wall of the church. Some false signals are given by the vegetation across the wall, but in the other regions it is possible to note the brick pattern below the plaster layer. Another noteworthy feature is an horizontal signal at the height of the walled up window. This suggests that the top end of the wall is a

raised part, and this is confirmed by historical notes on the building. Infrared thermography is very helpful in the process of checking the building structural integrity; this kind of images have demonstrated their usefulness not only in determining the building history but also in assessing seismic risk [44].

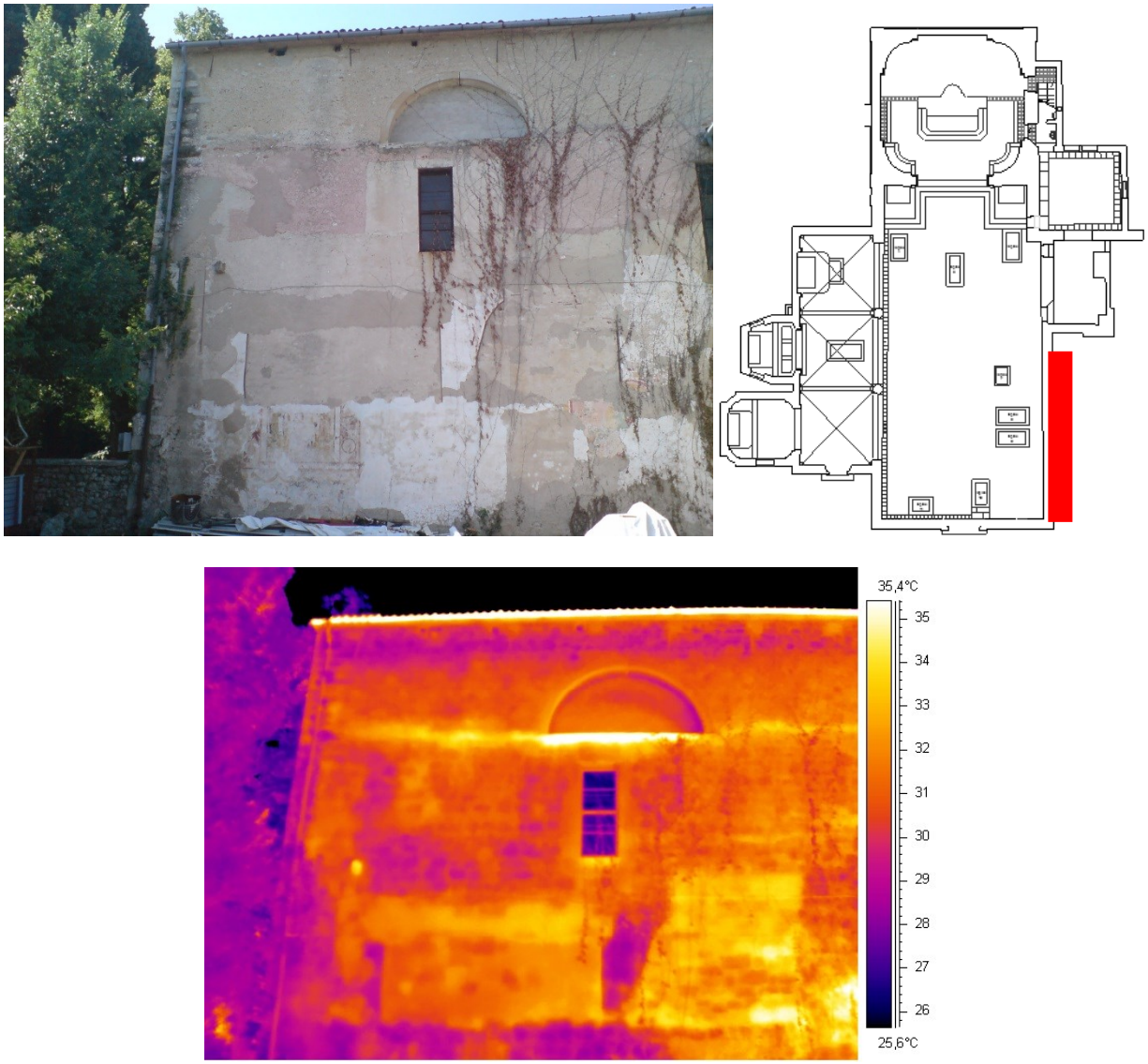

Figure 5.8: Photograph (left, top) of the lateral side of the St. Gottardo church. Drawing (right, top) of the church, where the investigated wall is identified by the red rectangle. Thermal image (bottom) showing the bricks underneath the finishing layer.

The automatic measurement, performed with IRpano system, allows to investigate a much wider number of surfaces in a smaller amount of time. The final output is still a map of surface temperature values, but the visualization is compatible with panoramic navigation interfaces. The interactive online view allows the user to navigate between different points of the building and zoom for details. A static image is presented in Figure 5.9, where a colder area is visible in the corner on the left side of the thermogram. The cause of the thermal signal, compatible with the presence of water,

was later confirmed as a leakage from a drainpipe. The panoramic image facilitates the localization and individuation of defects also during the stage that follows the on-site campaign, decreasing the risk of missing critical elements.

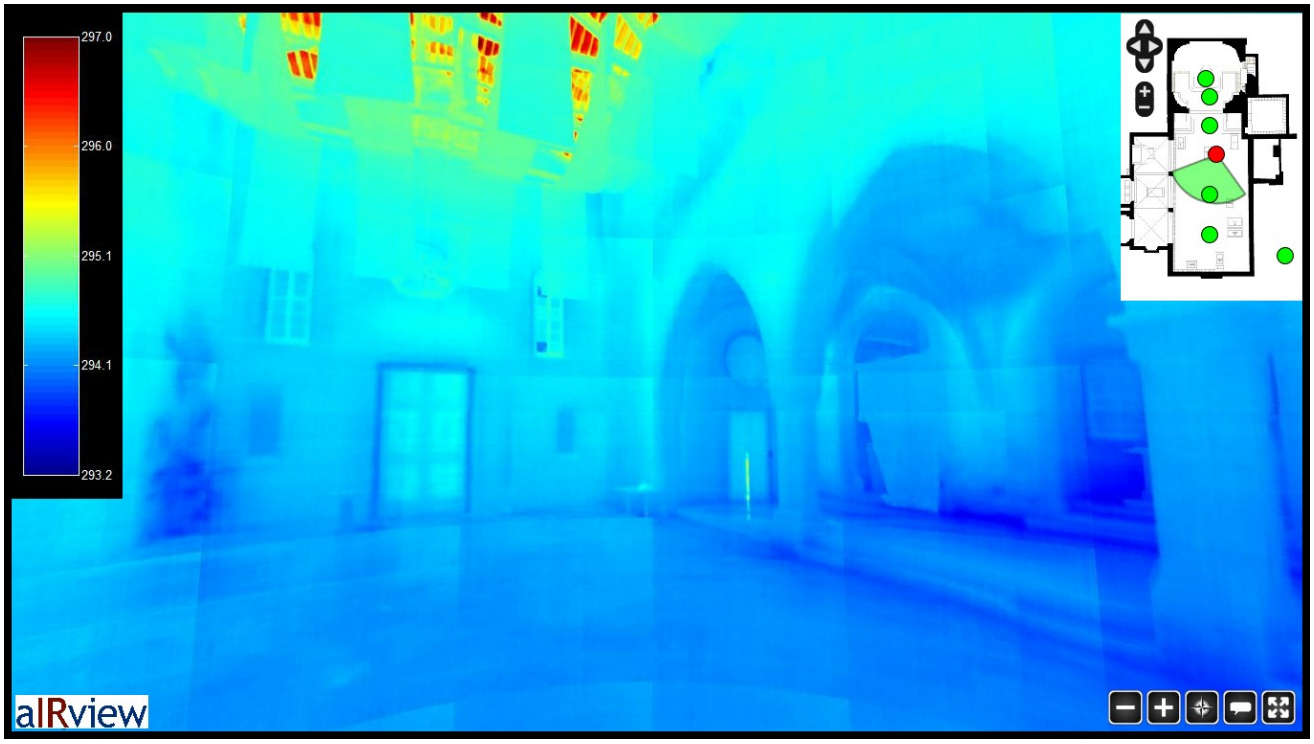

Figure 5.9: Output of an automatic surface temperature scan of the St. Gottardo church, embedded in an online panoramic viewer. An anomalous temperature signal is visible on the left corner.

5.3.2 Active thermography

The active thermographic survey may be focused on small parts of the walls or may be extended to a room or even to the entire building. The first example is Figure 5.10, where a small portable setup (1.5 kW lamp) is used to stimulate a portion of the vertical wall near the roof. In this case the passive image did not show any evidence of the wall structure, that becomes evident after the active survey.

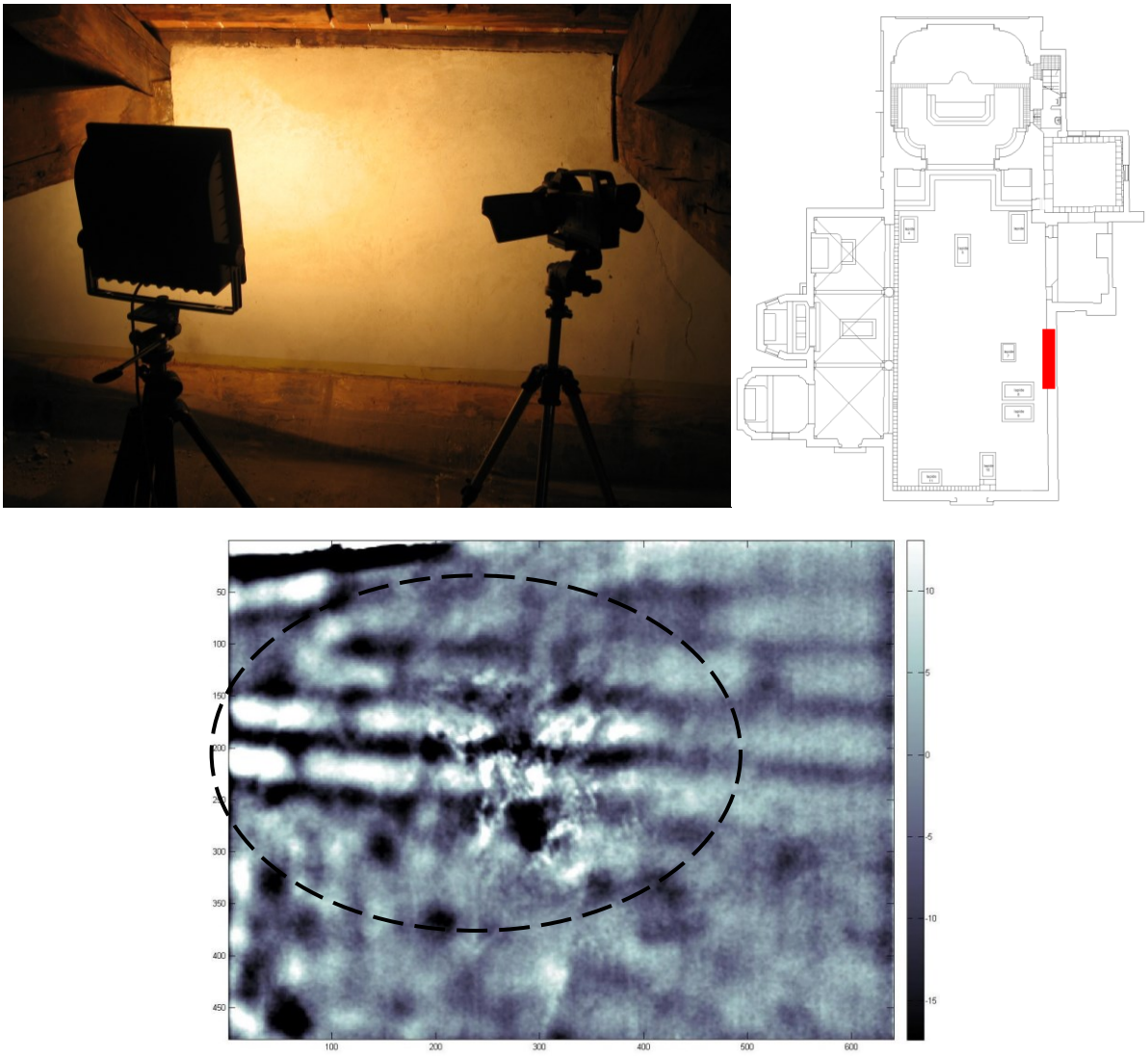

Figure 5.10: Photograph (left, top) of the investigated wall; the lamp is used as the thermal stimulus. Drawing (right, top) of the church, where the investigated wall is identified by the red rectangle. Processed image (bottom) showing the presence of different bricks (black circle) underneath the finishing layer (PCT algorithm).

The acquired images have been processed to further improve the original thermal signal. The use of a small portable setup allows a quick inspection (lasting few minutes) and could be executed in almost every part of the building, if scaffoldings are available. At the same time a compact lightweight thermal source limits significantly the area that could be scanned, that is typically lower than 2 m^2.

If possible, a good strategy is the use of high power air heaters, temporarily enclosing the region of interest with mobile partitioning if the room is extremely wide. Figure 5.11 shows the results of an investigation performed separating the side nave of the church from the main one. The wall structure is clearly visible and a small vertical detachment on the top is highlighted.

Figure 5.11: Photograph (left, top) of the investigated wall; air heaters are used as the thermal stimulus. Drawing (right, top) of the church, where the investigated wall is identified by the red rectangle. Thermal image (bottom) showing the wall structure and a small crack (black circle).

The eventual presence of cracks and detachments is always emphasized by an active survey, that is really useful also to compare neighboring zones. In Figure 5.12 a partially decorated wall was investigated with an active approach. The central region, that has a different finishing layer, shows a regular pattern while the side region and the decorated area have a different layout, due also to the presence of some detachments under the frescoes. This images are useful to the restorers that can plan the proper interventions on the decorated surfaces.

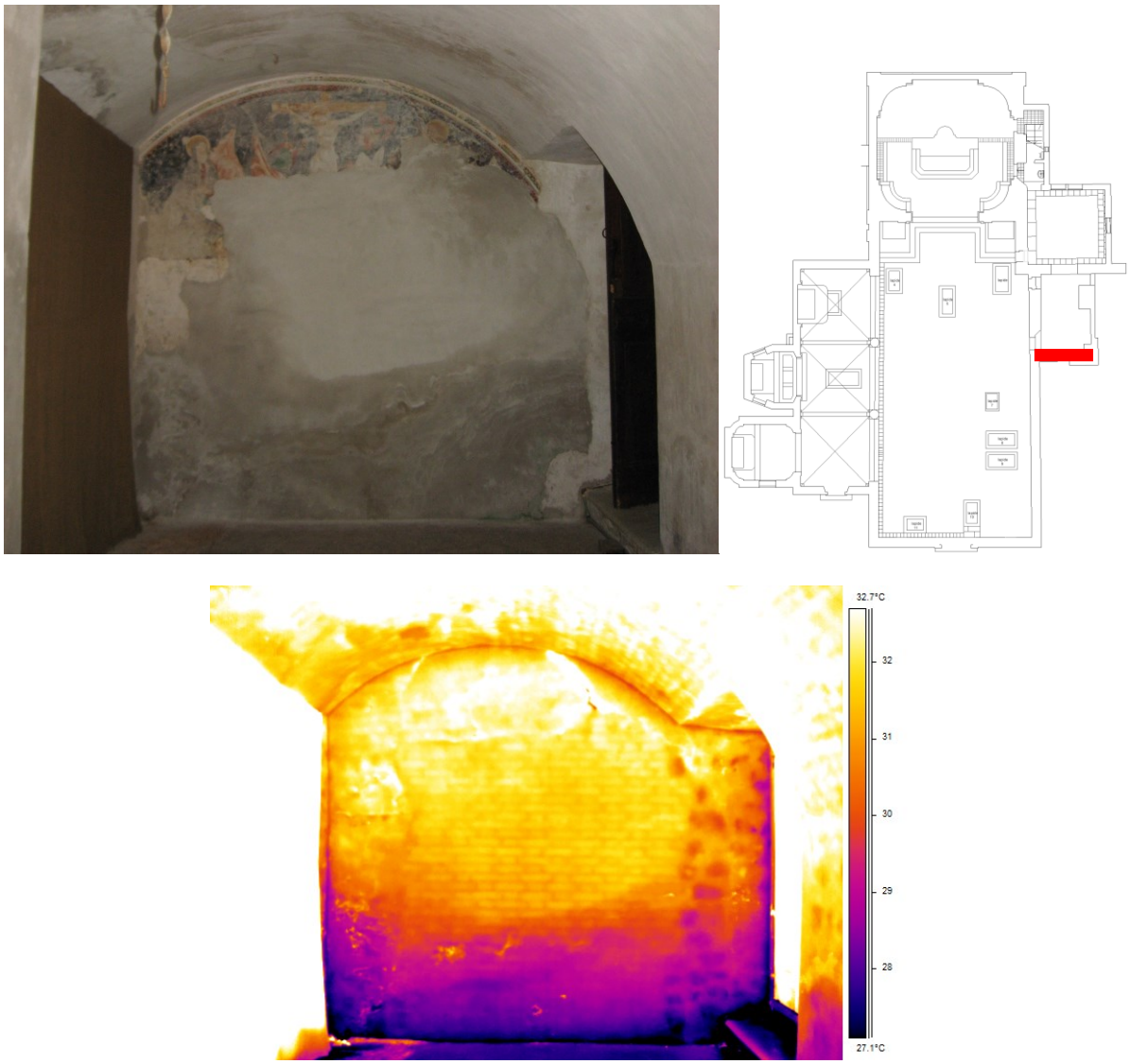

Figure 5.12: Photograph (left, top) of the investigated wall; air heaters are used as the thermal stimulus. Drawing (right, top) of the church, where the investigated wall is identified by the red rectangle. Thermal image (bottom) showing the different wall structure under the decorated wall and the other regions.

An active thermography may also lead to the discovery of hidden elements. The photograph of Figure 5.13 shows an apparently homogenous wall. The thermal image instead reveals the presence of a walled up door, where the lintel is clearly visible. This information are fundamental to evaluate the structural solidity of the edifice, especially during the retrofit process, where it is still possible to make corrections to the intervention plan.

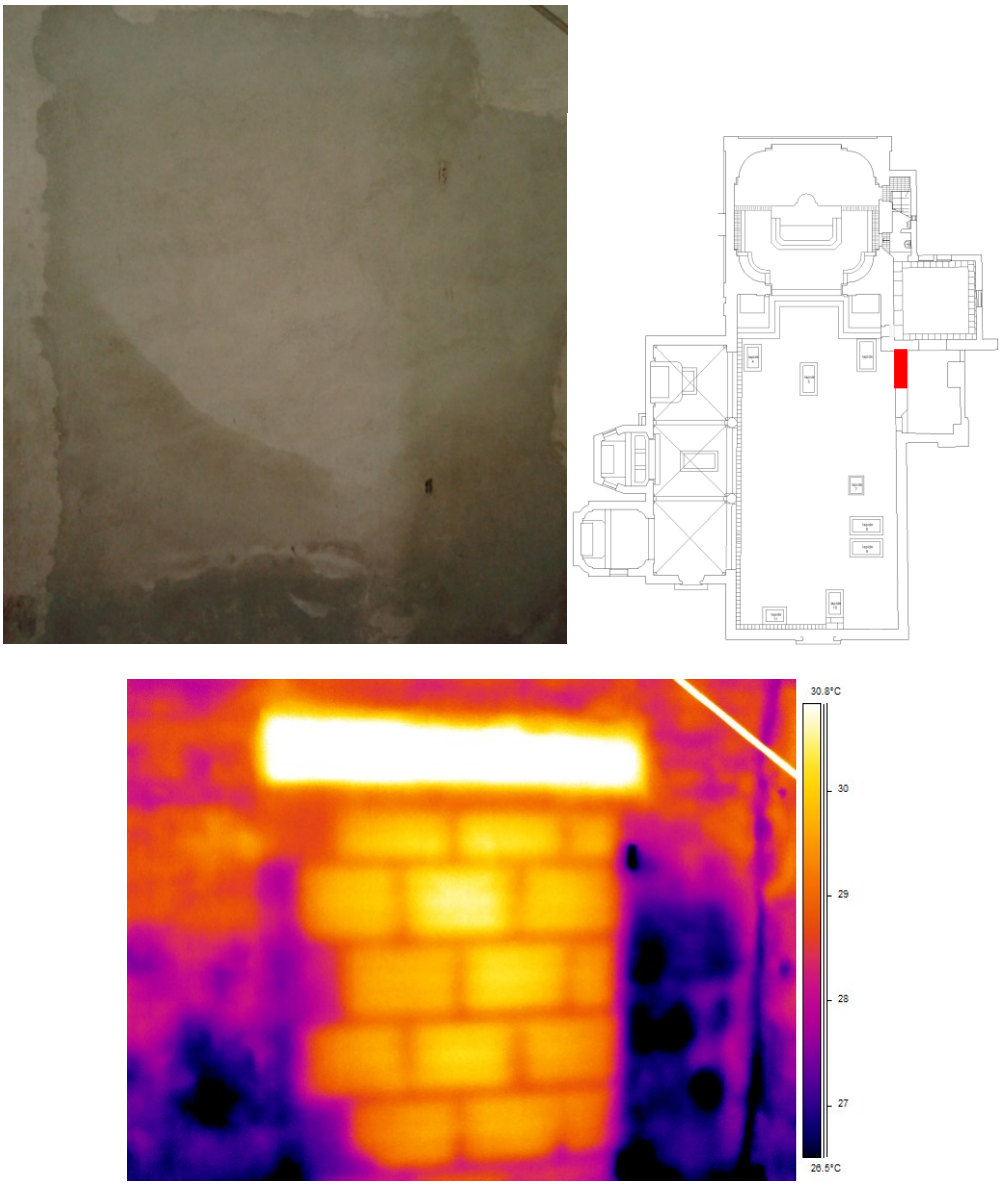

Figure 5.13: Photograph (left, top) of the investigated wall; air heaters are used as the thermal stimulus. Drawing (right, top) of the church, where the investigated wall is identified by the red rectangle. Thermal image (bottom) showing the an hidden walled up door.

Active thermography could be successfully coupled also to automatic survey. Figure 5.14 shows the results of an active survey at the Padri Serviti Convent, that highlights the wall structure under the plaster, allowing the verification of the supposed construction period. The output is embedded in a website that uses the Google Street View engine to create a virtual thermal map of the building. The survey was performed in multiple locations of the Convent, that are accessible from the navigation panel on the top right corner.

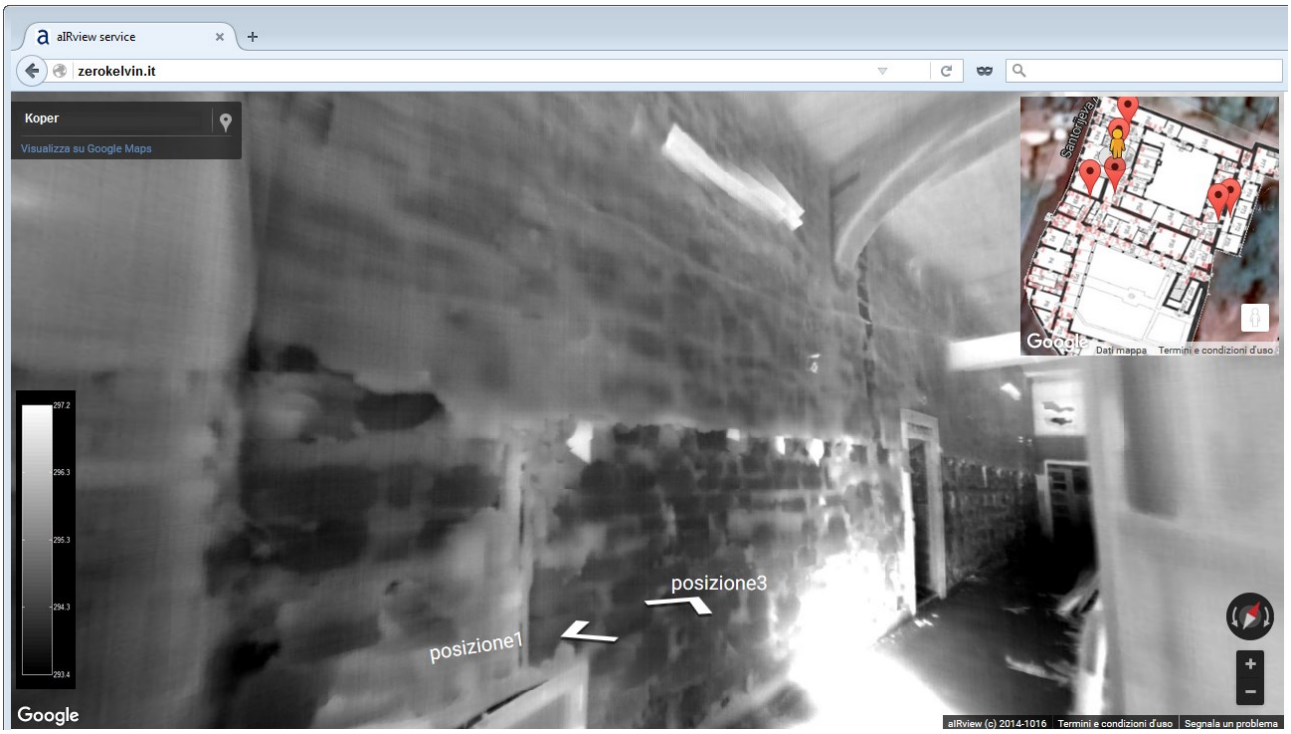

Figure 5.14: Output of an automatic surface temperature scan of the Padri Serviti Convent, embedded inside the Google Street View engine.

One of the main issue of an active thermographic measurement is keeping track of all the surfaces in a reduced amount of time, as the most useful indications are obtained during the transient phase. The automatic setup guarantees a fast acquisition rate of all the surface and allows the measurement of thermal sequences with a precise timing. This enables a post-processing analysis based on the temporal evolution of the thermal signal.

5.4 Air temperature distribution

As stated in Section 5.2.3, a noteworthy improvement given by the aIRview system is the possibility of measuring the air temperature distribution along a virtual surface. The following Figure 5.15 shows the air temperature distribution measured at the St. Vito Church. A vertical grid, sizing 25 m^2, was placed near the northeast wall, near the southeast walls, and before the presbytery of the church. The air temperature measurement was performed along with the air velocity and surface temperature ones. This data are useful in two ways: as a database to tune numerical simulations of the building and as a tool to perform microclimatic analysis.

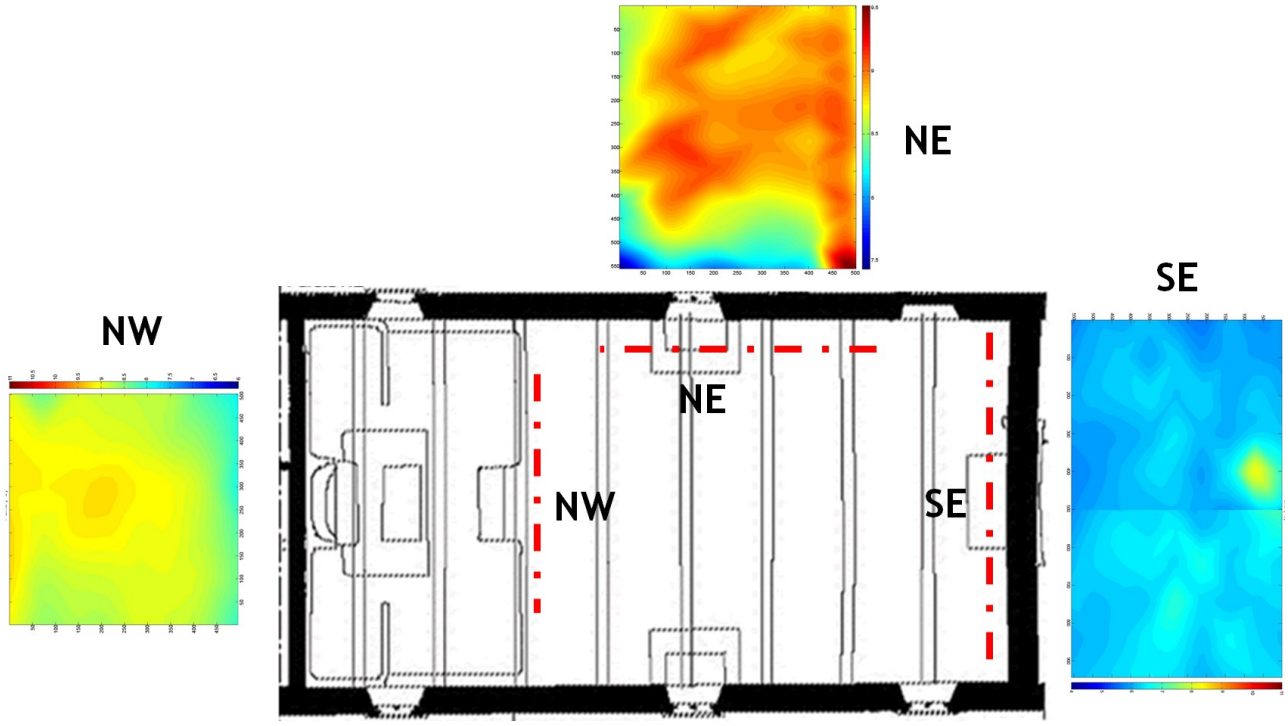

Figure 5.15: Air temperature measurement performed by the aIRview system inside the St. Vito Church on three surfaces of interest (red lines on the drawing).

As expected, the observed temperature distribution along the surfaces is quite homogenous, but it is possible to note a difference in the mean temperature levels, probably due to the church orientation and to the presence of the main entrance on the southeast side.

5.5 Air velocity distribution

Another peculiarity of the aIRview system is the possibility of measuring and visualizing the air velocity distribution on virtual vertical surfaces. Figure 5.16 shows the results obtain during the St. Vito Church survey. The same grid system of the air temperature measurement was used, oriented in the same way. As like as the air temperature distribution, the results are useful both to improve fluid dynamics models and to check the environmental conditions.

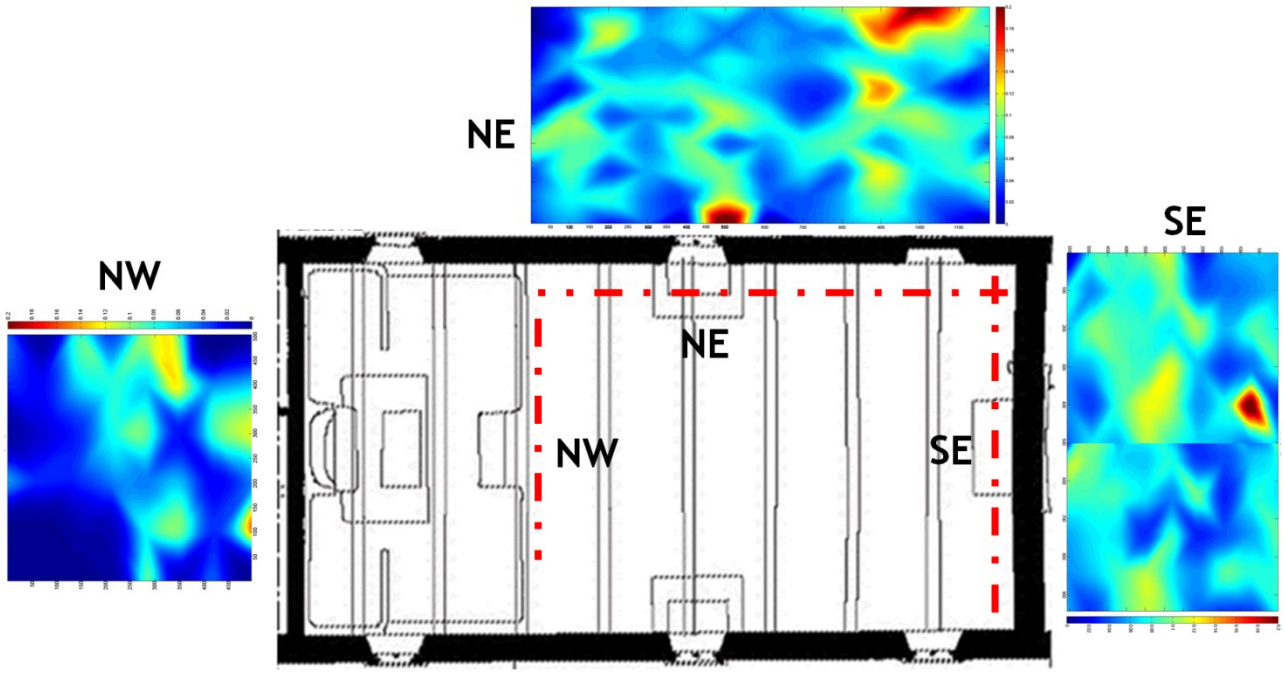

Figure 5.16: Air velocity measurement performed by the aIRview system inside the St. Vito Church on three surfaces of interest (red lines on the drawing).

It is possible to note that the air velocity is quite homogenous with few exceptions, probably caused by leakages from the fenestrations. In all cases, the absolute values are very low.

5.6 Moisture oriented measurements

The preservation of cultural heritage requires the knowledge of the phenomena involved in the process of decay of artworks. In the field of building conservation, the term efflorescence describes those mineral deposits that occur on the surface of stone masonry, bricks, plasters or other architectural elements. These crystals are generated as a result of evaporation of water in which salts were dissolved. The crystals can be formed both inside and outside of a surface, the latter are often related to conditions of fast water evaporation and are defined as subflorescence. Subflorescence is considered a much more dangerous phenomenon in respect to superficial efflorescence because the volume change of the salts can lead to mechanical damages inside the wall, causing the detachment of parts, such as the intonaco layer. Consequently it is paramount to detect the presence of water on the decorated surfaces and inside the walls before the decay mechanism starts. Moreover it is fundamental to discover the source and the behavior of the water over time, especially in relation to dynamic environmental conditions that may occur during the year. These can be sometimes predictable, as the effect of visiting people on the air moisture content, or unpredictable as seasonal weather changes [45–47].

Even though quantitative local methods, such as thermogravimetric analysis of wall samples [48], have proven to get precise information concerning the moisture content of the building materials, in most circumstances these methodologies are not appropriate, and often their application to artworks is not allowed due to their invasive or destructive characteristics. An alternative method to investigate the presence of water inside porous materials and artworks is observing its thermal effect by measuring the surface temperature with appropriated techniques such as infrared thermography. Literature shows that infrared thermography is also a valuable instrument for accurate thermal analysis of historical architectures in order to monitor indoor and outdoor surfaces and to evaluate the distribution of moisture [49,50].

The most basic building survey by infrared thermography is often restricted to the acquisition of single shot images taken in a limited range of time. Extending the examination in space and time makes it possible to get much more information. This can be achieved observing wider areas through the mosaicking technique commonly applied in photography for panorama views, as shown in the next Section 5.6.4. Moreover, the acquisition of multiple time lapsed images can easily increase the total observation

time, allowing to follow dynamically varying phenomena. These methods require a technical effort, since ordinary commercially available thermographic systems cannot perform these operations as the needed functions are not provided. The robotized system described in Section 5.2 is a solution to study buildings in transient conditions that was applied to the Novalesa Abbey, trying to take advantage of the periodic solar radiation due to the day/night cycle on the south facing wall. The aim of this study is to demonstrate the usefulness of an advanced infrared based acquisition system combined with active timed thermography technique, in pushing forward the knowledge of moisture related decay affecting the historical murals.

Another method was applied to the San Gottardo Church, where an active ventilation technique was implemented to survey areas under detachment risk, analyzing the surface temperature evolution over time. The aim of the work is providing detailed information on specific areas of the building.

5.6.1 Forced ventilation

The classification of the moisture content of a material is based on its Saturation Grade (*SG*), defined by the following relation:

$$SG = \frac{M_w - M_d}{M_s - M_d} \tag{5.13}$$

where:

M_w is the mass of the wet material [kg];

M_d is the mass of the dry material [kg];

M_s is the mass of the wet material at its saturation point [kg];

This measurement is obviously not feasible on-site on building walls, but it is possible to introduce a similar index, named Saturation Thermal Index (*STI*) [51]. The definition of *STI* is based on the *SG* concept, as shown by :

$$STI = \frac{T_w - T_d}{T_s - T_d} \tag{5.14}$$

where:

T_w is the temperature of the moist wall [T];

T_d is the temperature of the dry wall [T];

T_s is the temperature of the wall in saturation conditions [T];

These measurement could be performed on-site with an easy setup and a portable apparatus. *STI* is particularly sensitive to surface moisture, that is usually the most valuable part of the wall. The method is suitable for environmental condition that slow down the evaporation process (high relative humidity and low air velocities) that are typical of historical buildings. Another great advantage of these approach is measuring temperature differences instead of absolute temperatures, enhancing the performance of the thermal camera.

During the experimental procedure a part of the wall is moistened in such a way to reach a saturation conditions, while a second part is covered with a plastic film to inhibit any evaporation. The process of evaporation on the surface of the wall is successively enhanced by forced ventilation.

Figure 5.17: Experimental setup with the IR camera (on the left) and two air gun for forced ventilation (on the right).

During this stage, the IR camera records a sequence of images. Immediately after the switching on of the fan the saturated zone (artificially moistened) begins to decrease its temperature, while the zone with the plastic sheet remains at a constant value. The other zones change their values with a rate between these two extreme conditions. The

test continues until a steady condition is reached; in this case the test lasts about 5 minutes. A map of the severity of the humidity content (in percentage) is given according to the Saturation Thermal Index.

Figure 5.18 shows on the left a thermal image after reaching a steady state. It is clearly visible that the temperature has an increasing trend with the wall height. Three points at different heights from the floor are indicated. These are check points where the material has been sampled by means of a drill and measured for the humidity content by weighting technique [48]. On the right of Figure 5.18 the STI map is shown. The squared zone with the plastic sheet (low value of STI in blue color) is on the right top corner while the brown/red saturated zone with STI close to 100 % is on the right bottom corner. Also in this map the increasing trend is present.

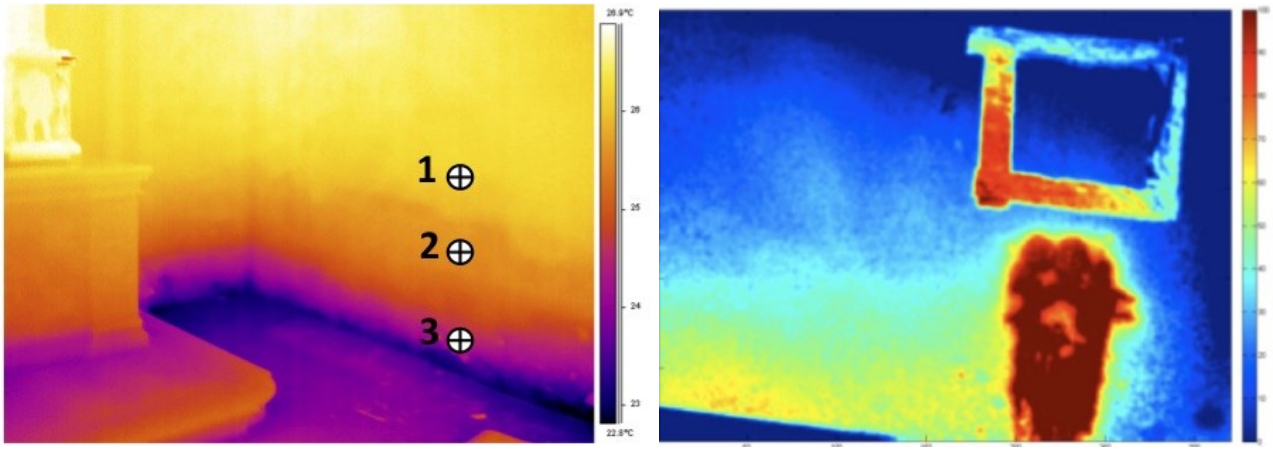

Figure 5.18: Thermal image (left) of the wall when the steady state is reached. The three comparison points, placed at different heights are highlighted. Map (right) of the STI index where it is clearly visible the squared zone with the plastic sheet (low value of STI in blue color) and the brown/red saturated zone with STI close to 100 %.

Table 5.4 confirms the validity of the thermographic approach, as the standard reference method shows the same trend of the proposed STI index.

Point	Height from floor [m]	Moisture content UNI 11085 [%]	Saturation Thermal Index (STI) [%]
1	1.1	2.7 %	15 %
2	0.7	6.2 %	30 %
3	0.2	11.4 %	60 %

Table 5.4: Comparison between moisture content and Saturation Thermal Index values for the three measurement points of Figure 5.18. Both methods show a proportional increase of the value at different heights.

5.6.2 Moisture timed images – modeling hypothesis

The goal of timed imaging is taking advantage of the periodic solar radiation due to the day/night cycle. The experiment is an active thermography procedure applied to the South wall of a building. Here the thermal source is the solar radiation that can be considered as a periodic stimulus $\cos(\omega t)$, where ω is the angular frequency ($2\pi/\tau$), t is the time, and τ is the period equal to 24 hours. As a consequence, a thermal wave propagates from the outer surface of the building to the inside of the chapel. Observing the wall from inside, assuming evenly space distributed solar radiation, constant thickness, and homogeneous properties of the wall, the water content is expected to have a key role in the observed thermal anomalies. Considering the thermal conductivity, the mass density, and the specific heat of the dry material (respectively λ_{dry}, ρ_{dry}, *and* c_{dry}) as reference values for wall materials taken from literature, the thermophysical properties (respectively λ_{eff}, ρ_{eff}, and c_{eff}) of the same wall in wet condition can be approximated [18, 19] taking into account the effect of water as a function of the ratio between the volume of moisture in the porosity otherwise filled by air and the total volume of the wall, as shown in Eq. 5.15 and 5.16:

$$\frac{\lambda_{dry}\lambda_{water}}{\lambda_{water} + \lambda_{dry} + \phi_{\frac{water}{total}}} \leq \lambda_{eff} \leq \lambda_{dry} + \lambda_{water}\phi_{\frac{water}{total}} \tag{5.15}$$

$$\begin{aligned} \rho_{eff}c_{eff} &= \frac{M_{total}}{V_{total}}\left[c_{dry}\frac{M_{dry}}{M_{tot}} + c_{water}\frac{M_{water}}{M_{total}}\right] \\ &= \mathrm{c_{dry}}\rho_{dry} + c_{water}\frac{M_{water}}{V_{water}}\frac{V_{water}}{V_{total}} \\ &= c_{dry}\rho_{dry} + c_{water}\rho_{water}\phi_{\frac{water}{total}} \end{aligned} \tag{5.16}$$

where:

$\phi_{\frac{water}{total}}$ is the ratio between the volume of moisture in the porosity otherwise filled by air and the total volume of the wall;

λ_{dry} is the thermal conductivity of the dry wall materials [W m^{-1} K^{-1}];

λ_{water} is the thermal conductivity of water [W m^{-1} K^{-1}];

ρ_{dry} is the mass density of the dry wall materials [kg m^{-3}];

ρ_{water} is the mass density of water [kg m^{-3}];

M_{dry} is the mass of the dry wall materials [kg];

M_{water} is the mass of the water in the wall [kg];

M_{total} is the mass of the wall [kg];

c_{dry} is the specific heat of the dry wall materials [J kg^{-1} K^{-1}];

c_{water} is the specific heat of water [J kg^{-1} K^{-1}];

V_{water} is the volume of the water in the wall [m^3];

V_{total} is the volume of the wall [m^3].

The inner surface temperature oscillates with the same period of the solar heat flux. The amplitude of the wave depends on the thermophysical properties of the wall; its phase as well, as schematized in Figure 5.19. After recording the inner surface temperature over several days, a Fast Fourier Transform of the temperature signal has been computed for every pixel [29], retrieving amplitude and phase at the frequency corresponding to a period equal to 24 hours [3].

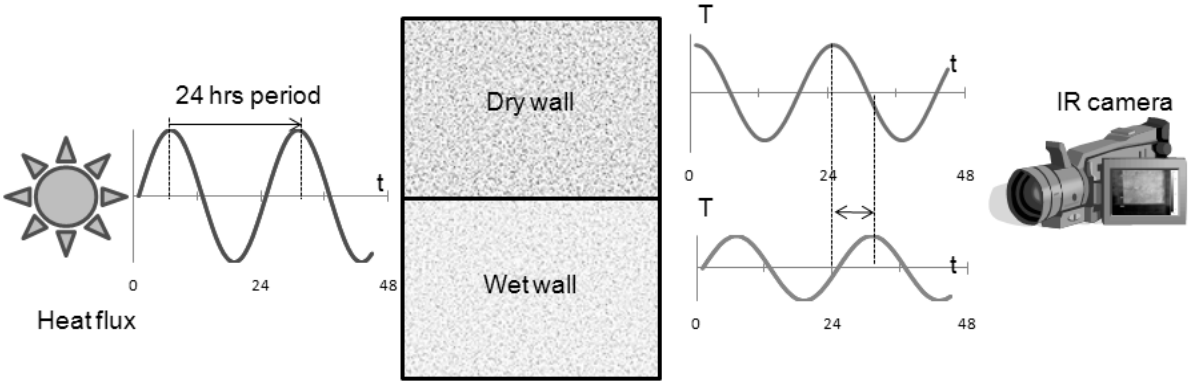

Figure 5.19: Experimental setup schematization. In order to collect information about the effect of dry and wet materials on the thermal waves behavior, temperature variation of the inside surface is recorded over time

By Eq. 5.15 and 5.16 it is possible to calculate the thermal diffusivity values for both dry (Eq. 5.17) and wet (Eq. 5.18) conditions and the expected penetration depth of thermal waves at a given time.

$$\alpha_{dry} = \frac{\lambda_{dry}}{\rho_{dry} c_{dry}}; \qquad \mu_{dry} = \sqrt{\frac{2\alpha_{dry}}{\omega}} \tag{5.17}$$

$$\alpha_{wet} = \frac{\lambda_{wet}}{\rho_{wet} c_{wet}}; \qquad \mu_{wet} = \sqrt{\frac{2\alpha_{wet}}{\omega}} \tag{5.18}$$

where:

a_{dry} is the thermal diffusivity of the wall material in dry condition;

μ_{dry} is the thermal wave penetration depth of the wall material in dry condition;

a_{wet} is the thermal diffusivity of the wall material in wet condition;

μ_{wet} is the thermal wave penetration depth of the wall material in wet condition.

The following relation 5.19 represents the behavior of the thermal wave as a function of depth x and time t:

$$T(x,t) \propto Ae^{-\frac{x}{\mu}}\cos(\omega t - \frac{x}{\mu}) \tag{5.19}$$

μ assumes the value μ_{dry} or μ_{wet} depending on moisture conditions. The amplitude of the thermal wave is exponentially decreased and its phase is linearly delayed, depending on μ, that on its turn depends on the water content as in Eq. 5.17 and 5.18. Comparing the reference values, shown in Table 5.5, it is evident that, despite variations on thermal conductivity and mass density, the specific heat plays a key role in the thermal wave propagation mechanism governed by thermal diffusivity (a). Since the heat capacity (ρc) of water is sensibly greater than the heat capacity of the considered construction materials, the resulting hypothesis is that the thermal waves that pass through the wet material should be attenuated (have a lower amplitude) and phase shifted compared to the thermal wave passing though the dry material.

Material	**λ** **[W m^{-1} K^{-1}]**	**ρ** **[kg m^{-3}]**	**c** **J kg^{-1} K^{-1}]**	**C** **[kJ K^{-1} m^{-3}]**	**α** **[m^2 s^{-1}]**
Clay bricks – dry[1]	0.5	1800	840	1512	3.31 E-07
Clay bricks – 10% water content[2]	0.56	1900	1016	1903	2.90E-07
Clay bricks – 20% water content[2]	0.62	2000	1174	2348	2.64E-07

Clay bricks – 40% water content[2]	0.74	2200	1448	3185	2.32E-07
Marble – dry[1]	2.8	2600	800	2080	1.35E-06
Marble – 5% water content[2]	2.85	2650	864	2290	1.24E-06
Pietra Serena (sandstone) – dry[1]	2.45	2540	811	2060	1.19E-06
Pietra Serena (sandstone) - 5% water content[2]	2.5	2590	876	2269	1.10E-06
Water[3]	0.6	1000	4182	4182	1.43E-07

Table 5.5: Thermophysical properties of common construction materials: 1 values measured at CNR-ITC lab; 2 values computed by Eq. 5.15 - 5.18, 3 values taken from literature [22]

5.6.3 Moisture timed images – mathematical model

The wall structure has been simply modeled in small scale to proportionally replicate the real phenomena, in bricks, assuming the thermophysical properties of this material from the values of Table 5.5and a thickness equal to 0.05 m.

In order to model four different moisture contents at constant thickness, part of the voids volume has been progressively replaced with water, moving from dry condition to saturation (40% water content) as in Table 5.5:

Clay bricks – dry (represents the ideal dry wall),

Clay bricks – 10% water content;

Clay bricks – 20% water content;

and Clay bricks – 40% water content (represents the saturated wall).

The solar thermal stimulus has been scaled too and has been modeled as a periodic heat wave of period equal to 1 hour. The model has been built using Finite Element Method (FEM) [52]. The surface temperatures have been collected during the dynamic process and then analyzed using FFT algorithm extracting amplitude and phase parameters. The following picture shows the thermal behavior of the test block: the dry wall is represented in continuous black line, the three different moisture conditions are

represented in dashed gray lines. Figure 5.20 shows the evolution of surface temperatures over two modeled periods.

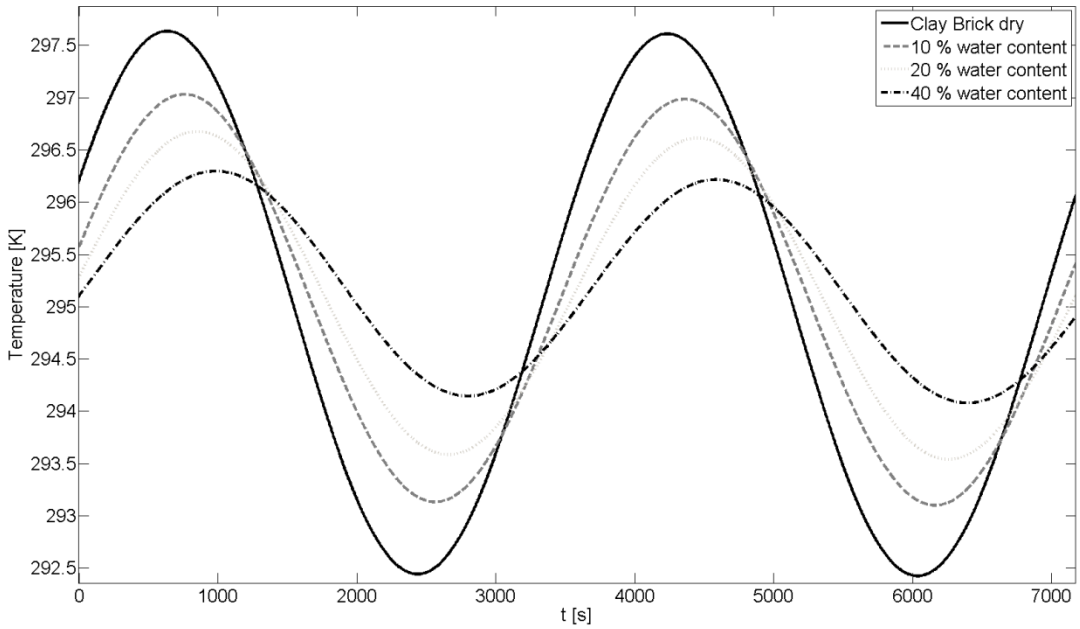

Figure 5.20: Surface temperatures evolution of the modeled clay brick specimen with different water contents. As expected, both dry and wet wall surface temperatures oscillate with the same period of the imposed stimulus. The wet material waves have lower amplitude than the dry one and are delayed in phase according to the increasing water content.

The temperature profiles, as seen in Figure 5.20, are usually represented in time domain. Applying the Discrete Fourier Transform to the time evolution of every pixel it is possible to consider the data in frequency domain according to the following Eq. 5.20:

$$F_u = \frac{1}{N}\sum_{u=0}^{N-1} h(t)\, exp^{(-\frac{j2\pi ut}{N})} = Re(F_u) + jIm(F_u) \qquad (5.20)$$

where:

u is the frequency;

N is number of images of the thermal sequence;

j is the imaginary unit;

Re is the real part of the transform;

Im is the imaginary part of the transform.

Amplitude (*A*) and Phase (*Φ*) are obtained as follows in Eq. 5.21:

$$A_u = \sqrt{Re(F_u)^2 + Im(F_u)^2}; \qquad \phi_u = tan^{-1}(\frac{Im(F_u)}{Re(F_u)}) \tag{5.21}$$

The following Table 5.6 summarizes the results (A and Φ) of the FFT algorithm applied on the modeled data.

Material	Amplitude [a.u.]	Phase [rad]
Clay bricks	2588	0.196
Clay bricks – 10% water content	1933	0.416
Clay bricks – 20% water content	1522	0.584
Clay bricks – 40% water content	1045	0.824

Table 5.6: Amplitude and Phase values at different moisture contents show a different behavior of dry and wet simulated walls. The obtained amplitude and phase values are coherent with the theoretical expectations and so this method potentially distinguishes dry from wet conditions.

The obtained *A* and *Φ* values are represented in table 2 for the third frequency component of the Fourier Transform, which is the most important component as it is the first harmonic of the analyzed signal. As expected the presence of water determines lower amplitude and a phase shift in respect to the wave describing the dry condition.

5.6.4 Moisture timed images – data collection

The aIRview system was set to operate in indoor environment at the Novalesa Abbey. The system was monitoring three inside walls of St. Eldrad's chapel (South, West and North), every 15 minutes for more than one week. This sampling rate is considered more than adequate according to the sampling theorem, being the acquisition frequency much greater than the Nyquist frequency for sampling phenomena that can be described as a continuous signal with a period equal to 24 hours. The infrared system was placed in the center of the building, at about 2.5 m from the South wall.

Figure 5.21: This picture shows the South wall decoration damaged in the lower part. On the right the robotized system is looking at the special reference targets placed near the wall.

In small buildings like St. Eldrad chapel this represents a common problem because at this short distance the typical lens available for infrared cameras, that are generally characterized by a quite limited field of view, make difficult to acquire the whole wall surface. The robotized system allows to move the camera and to scan the surface of interest at a proper pixel resolution. In this application the surface is essentially Lambertian and the average emissivity is around 0.90 (evaluation done according to [34]). Thermal data of the inside surfaces are integrated with local microclimatic information provided by the aIRview system itself and two data loggers monitoring the thermohygrometric conditions inside the room. External data such as temperature, relative humidity and solar radiation are supplied by Regional Agency for the Protection of the Environment of Piemonte (ARPA), measured with a weather station and other air temperature and relative humidity probes.

After processing the data produced by aIRview as FFT amplitude and phase of the South wall, it is possible to clearly distinguish three different horizontal areas, positioned at different heights (A, M and B) as seen in Figure 4. In particular, the areas labeled A and B show common characteristics, much different from the central M. The limits of horizontal separation between A and M, and between M and B correspond to the most damaged areas of the painted surface, characterized by a strong presence of efflorescence. This occurrence indicates that such areas could be evaporative fronts and this is compatible with the presence of capillary rise phenomena.

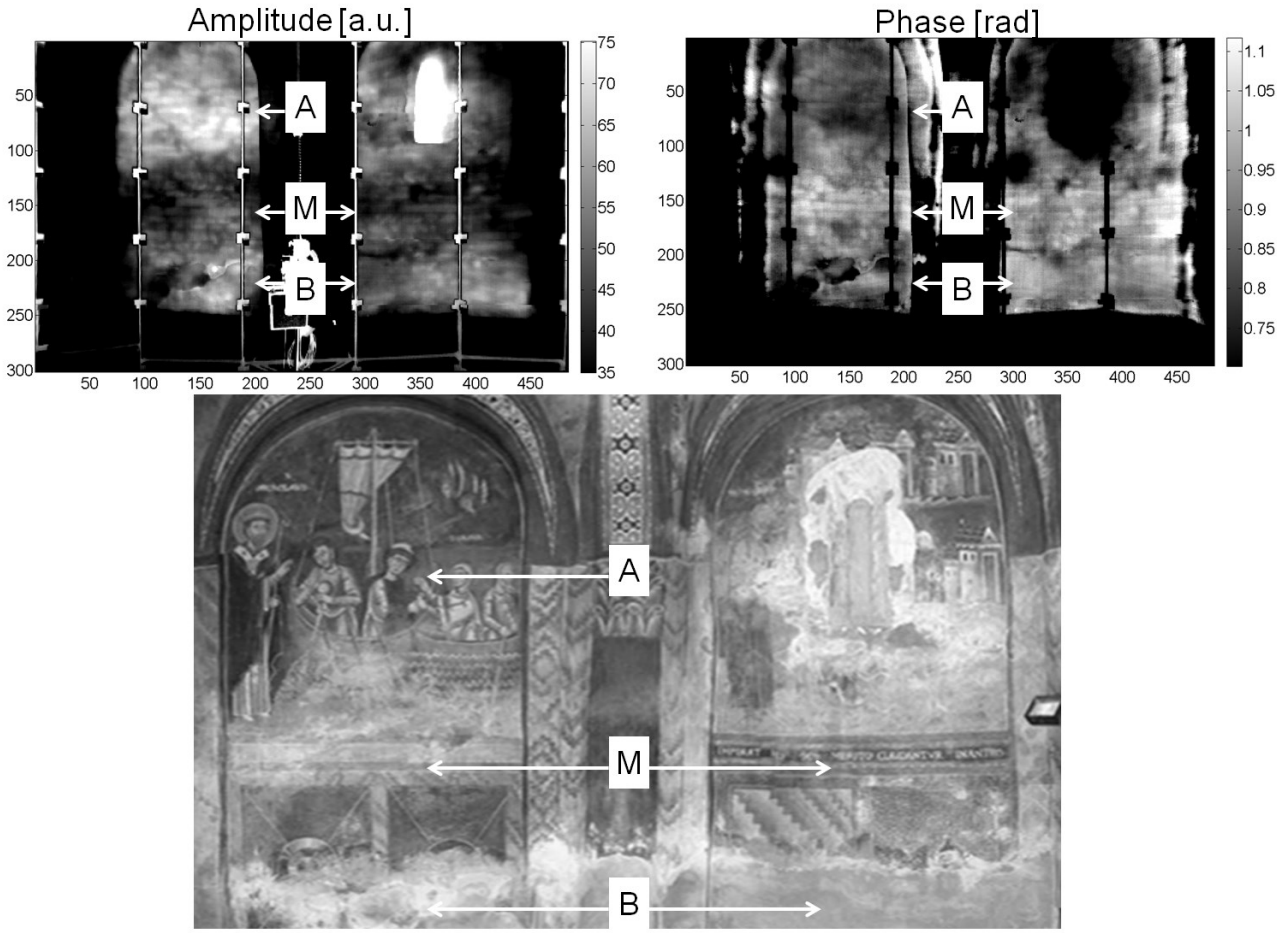

Figure 5.22: Amplitude (left) and Phase (right) images. The results show three different horizontal areas, positioned at different heights (A, M and B) with different behavior, not related to the surface coating visible in the photograph (bottom).

According to the mathematical model and the FEM simulation results, the Amplitude and Phase images allow to advance the hypothesis that M area corresponds to wetter wall condition compared to the adjacent A and B. The average values of the areas are compared in Table 5.7. The higher area on the right side of the wall is excluded from the analysis due to its reduced thickness with respect to the rest of the wall.

Area	Amplitude [a.u.]	Phase [rad]
A	54.4	0.822
M	44.4	0.963
B	62.2	0.843

Table 5.7: Amplitude and Phase values show that area M are attenuated and phase shifted with respect to the A and B areas. This can be attributed to higher moisture content, as described in the previous sections.

The early outcomes of this long term project show how timed acquisitions of wide areas can be useful to study certain phenomena, that are otherwise impossible to detect with static or time limited acquisitions. The chosen case study was particularly challenging due to its peculiar context that required reliable hardware. However, by analyzing South (damaged) wall as FFT amplitude and phase images, it has been possible to advance hypotheses that explain the decay mechanism related to moisture presence.

These technique could be improved by a complementary measurement campaign to be conducted in the summer season, during thermal stable weather conditions and sunny days, that could provide even more reliable results that will help to understand the phenomena that cause the damage. Furthermore seasonal measurement campaigns could give information about possible changes in the pattern of the moistened areas and regarding the repeatability of the presented experimental procedure. Future work should also include more sophisticated comparisons with software simulation that will take into account real recorded data as input and local microclimatic information (i.e. air moisture contribution from tourists and air flows from leaking windows).

5.7 References

[1] BS EN 13187: 1999 - Thermal performance of buildings – Qualitative detection of thermal irregularities in building envelopes – Infrared method. BSI London, 1999.

[2] T.W. Hughes, Thermal imaging and the fourth amendment:Kyllo v. U.S., Am J Crim Just. 26 (n.d.) 43–60. doi:10.1007/BF02886856.

[3] A. Bortolin, G. Cadelano, G. Ferrarini, P. Bison, F. Peron, X. Maldague, High-resolution survey of buildings by lock-in IR thermography, in: Thermosense: Thermal Infrared Applications XXXV, 2013: pp. 870503-870503–9. doi:10.1117/12.2016592.

[4] B. Lehmann, K. Ghazi Wakili, T. Frank, B. Vera Collado, C. Tanner, Effects of individual climatic parameters on the infrared thermography of buildings, Applied Energy. 110 (2013) 29–43. doi:10.1016/j.apenergy.2013.03.066.

[5] S. Van De Vijver, M. Steeman, N. Van Den Bossche, K. Carbonez, A. Janssens, The influence of environmental parameters on the thermographic analysis of the building envelope, in: 12th International Conference on Quantitative InfraRed Thermography (QIRT 2014), 2014.

[6] American society for testing and materials ASTM C1060 – 11a - Standard practice for thermographic inspection of insulation installations in envelope cavities of frame buildings, 2011.

[7] C. Tanner, B. Lehmann, T. Frank, K.G. Wakili, Vorschlag zur standardisierten Darstellung von Wärmebildern mit QualiThermo, Bauphysik. 33 (2011) 345–356. doi:10.1002/bapi.201110801.

[8] A. Colantonio, G. McIntosh, The Differences Between Large Buildings and Residential Infrared Thermographic Inspections Is Like Night and Day, in: Alberta, 2007: p. 13.

http://www.nbec.net/documents/THEDIFFERENCEBETWEENLARGEBUILDINGSANDRESIDENTIALINFRAREDTHERMOGRAPHICINSPECTIONSISLIKENIGHTA.pdf.
[9] NBN EN 13187 - Thermal performance of buildings – Qualitative detection of thermal irregularities in building envelopes – Infrared method - BIN Brussels, 1999.
[10] G. Dall'O', L. Sarto, A. Panza, Infrared Screening of Residential Buildings for Energy Audit Purposes: Results of a Field Test, Energies. 6 (2013) 3859–3878. doi:10.3390/en6083859.
[11] C.A. Balaras, A.A. Argiriou, Infrared thermography for building diagnostics, Energy and Buildings. 34 (2002) 171–183. doi:10.1016/S0378-7788(01)00105-0.
[12] L. Eads, R. Epperly, J. Snell, Thermography: Practical guide, ASHRAE Journal. (2010) 51–55.
[13] P.A. Fokaides, S.A. Kalogirou, Application of infrared thermography for the determination of the overall heat transfer coefficient (U-Value) in building envelopes, Applied Energy. 88 (2011) 4358–4365. doi:10.1016/j.apenergy.2011.05.014.
[14] T. Taylor, J. Counsell, S. Gill, Energy efficiency is more than skin deep: Improving construction quality control in new-build housing using thermography, Energy and Buildings. 66 (2013) 222–231. doi:10.1016/j.enbuild.2013.07.051.
[15] R. Albatici, A.M. Tonelli, Infrared thermovision technique for the assessment of thermal transmittance value of opaque building elements on site, Energy and Buildings. 42 (2010) 2177–2183. doi:10.1016/j.enbuild.2010.07.010.
[16] M. Behaneck, Bauthermografie-Praxis: Tipps & Tricks für Einsteiger, (2011) 44–49.
[17] VATh Bundesverband für Angewandte Thermografie, Bauthermografie: zur Planung, Durchführung und Dokumentation infrarotthermografischer Messungen an Bauwerken oder Bauteilen von Gebäuden, 2011.
[18] G. Dall'O', Green Energy Audit of Buildings, Springer London, London, 2013. http://link.springer.com/10.1007/978-1-4471-5064-0 (accessed August 23, 2016).
[19] TheCH (Association Suisse de thermographie). Standard de qualité bâtiment., 2010.
[20] E. Barreira, S.S. de Freitas, V.P. de Freitas, J.M.P.Q. Delgado, Infrared thermography application in building diagnosis: A proposal for test procedures., in: Industrial and Technological Applications of Transport in Porous Materials, Springer US, 2013: pp. 91–117.
[21] L. Charlier, Utilisation de la thermographie pour la détermination des déperditions thermiques d'un bâtiment, Université de Liège, 2007.
[22] RESNET Residential energy services network, Interim guidelines for thermographic inspections of buildings, 2012.
[23] C. Pearson, Thermal Imaging of Building Fabric. BSRIA guide 39, (2011).
[24] ASTM E1862 –97 - Standard Test Method for Measuring and Compensating for Reflected Temperature Using Infrared Imaging Radiometers, 2002.
[25] F. Asdrubali, G. Baldinelli, F. Bianchi, A quantitative methodology to evaluate thermal bridges in buildings, Applied Energy. 97 (2012) 365–373. doi:10.1016/j.apenergy.2011.12.054.
[26] M.B. Dufour, D. Derome, R. Zmeureanu, Analysis of thermograms for the estimation of dimensions of cracks in building envelope, Infrared Physics & Technology. 52 (2009) 70–78. doi:10.1016/j.infrared.2009.01.004.
[27] ENERGY STAR Certified Homes, Version 3 (Rev. 07). Inspection Checklists for National Program Requirements, (2013). https://www.energystar.gov/ia/partners/bldrs_lenders_raters/downloads/Inspection_Checklists.pdf.

[28] Agenzia per l'Energia Alto Adige - Casa Clima, Criteri Casaclima per l'esecuzione delle prove di tenuta all'aria, (2015). http://www.agenziacasaclima.it/files/content/139738_16446_2_0/critericc-bdt-kriterienkha-bdt-v1.0.pdf.
[29] M.T. Klein, C. Ibarra-Castanedo, X.P. Maldague, A. Bendada, A straightforward graphical user interface for basic and advanced signal processing of thermographic infrared sequences, in: Proc. SPIE 6939, Thermosense XXX, 2008. doi:10.1117/12.776781.
[30] G. Ferrarini, G. Cadelano, A. Bortolin, Automatic thermographic scanning with the creation of 3D panoramic views of buildings, in: 2016. doi:10.1117/12.2225083.
[31] G. Cadelano, P. Bison, A. Bortolin, G. Ferrarini, F. Peron, M. Girotto, M. Volinia, Monitoring of historical frescoes by timed infrared imaging analysis, Opto-Electronics Review. 23 (2015) 102–108.
[32] E. Grinzato, Humidity and air temperature measurement by quantitative infrared thermography, Quantitative InfraRed Thermography Journal. 7 (2010) 55–72. doi:10.3166/qirt.7.55-72.
[33] D. Anguelov, C. Dulong, D. Filip, C. Frueh, S. Lafon, R. Lyon, A. Ogale, L. Vincent, J. Weaver, Google Street View: Capturing the World at Street Level, Computer. 43 (2010) 32–38. doi:10.1109/MC.2010.170.
[34] R. Madding, Emissivity measurement and temperature correction accuracy considerations, in: Thermosense: Thermal Infrared Applications XXI, SPIE, Orlando, 1999.
[35] P. Bison, A. Bortolin, G. Cadelano, G. Ferrarini, K. Furlan, E. Grinzato, Geometrical correction and photogrammetric approach in thermographic inspection of buildings, in: 11th International Conference on Quantitative InfraRed Thermography, Naples, 2012. doi:10.21611/qirt.2012.285.
[36] S. Lagüela, L. Díaz−Vilariño, D. Roca, H. Lorenzo, Aerial thermography from low-cost UAV for the generation of thermographic digital terrain models, Opto-Electronics Review. 23 (2015) 78–84. doi:10.1515/oere-2015-0006.
[37] M. Petroff, Pannellum, 2016. https://mpetroff.net/2016/01/pannellum-2-2/.
[38] E. Grinzato, P. Bison, G.. Cadelano, F. Peron, R-value estimation by local thermographic analysis, in: R.B. Dinwiddie, M. Safai (Eds.), 2010: p. 76610H. doi:10.1117/12.850729.
[39] A. Bortolin, G. Cadelano, G. Ferrarini, P. Bison, F. Peron, S. Trevisani, IR thermography and geophysical survey applied to the retrofit of an ancient church, in: Ankara, 2014.
[40] P. Bison, A. Bortolin, G. Cadelano, G. Ferrarini, F. López, X. Maldague, Comparison of image processing techniques for the on-site evaluation of damaged frescoes, in: Thermosense: Thermal Infrared Applications XXXVI, 2014. doi:10.1117/12.2053782.
[41] P. Bison, A. Bortolin, G. Cadelano, G. Ferrarini, L. Finesso, F. Lopez, X. Maldague, Evaluation of frescoes detachments by partial least square thermography, in: Bordeaux, 2014. doi:10.21611/qirt.2014.109.
[42] A. Bortolin, P. Bison, G. Cadelano, G. Ferrarini, S. Fortuna, Measurement of thermophysical properties coupled with LCA assessment for the optimization of a historical building retrofit, J. Phys.: Conf. Ser. 655 (2015) 12011. doi:10.1088/1742-6596/655/1/012011.
[43] G. Ferrarini, P. Bison, A. Bortolin, G. Cadelano, M. Girotto, U. Mazzali, F. Peron, M. Volinia, Energy survey of a historical building by infrared thermography, Atti Della Fondazione Giorgio Ronchi. 69 (2014).

[44] E. Grinzato, G. Cadelano, P. Bison, A. Petracca, Seismic risk evaluation aided by IR thermography, in: 2009. doi:10.1117/12.818610.
[45] D. Camuffo, E. Pagan, A. Bernardi, F. Becherini, The impact of heating, lighting and people in re-using historical buildings: a case study, Journal of Cultural Heritage. 5 (2004) 409–416. doi:10.1016/j.culher.2004.01.005.
[46] D. Camuffo, Microclimate for Cultural Heritage - Conservation, Restoration and Maintenance of Indoor and Outdoor Monuments, Elsevier, 2013.
[47] H.E. Silva, F.M.A. Henriques, Microclimatic analysis of historic buildings: A new methodology for temperate climates, Building and Environment. 82 (2014) 381–387. doi:10.1016/j.buildenv.2014.09.005.
[48] UNI 11085:2003 Beni culturali-Materiali lapidei naturali ed artificiali-Determinazione del contenuto d'acqua: Metodo ponderale., 2003.
[49] E. Rosina, E. Grinzato, Infrared and Thermal Testing for Conservation of Historic Buildings, Materials Evaluation. 59 (2001) 942–954.
[50] E. Grinzato, N. Ludwig, G. Cadelano, M. Bertucci, M. Gargano, P. Bison, Infrared thermography for moisture detection: A laboratory study and in-situ test, Materials Evaluation. 69 (2011) 97–104.
[51] E. Grinzato, G. Cadelano, P. Bison, Moisture map by IR thermography, Journal of Modern Optics. 57 (2010) 1770–1778. doi:10.1080/09500341003731597.
[52] Comsol Multiphysics Version 4, 2011.

6 Measuring heat fluxes in buildings: new methods for performance evaluation

In this chapter, based on published works [1–4], new methods for the performance evaluation of the building envelope and HVAC system by infrared thermography are proposed. Firstly, the thermal bridges are investigated with the aim of quantifying the thermal losses. Successively, the steady state thermal transmittance of a wall is evaluated with different techniques. The envelope investigation is closed with the evaluation of the dynamic building behavior of insulating materials, a laboratory technique that can be extended on-site. The last section deals with the measurement of radiant heating systems performance.

6.1 Evaluation of thermal bridges

The current trend in construction technologies, strongly imposed by the standards, is to create buildings with a high level of insulation. The target value of thermal transmittance, the thermal property of the wall elements that defines the heat transfer between the building and the outer environment, is constantly decreasing over time. In this framework the energy demand is highly influenced also by the presence of thermal bridges, that are the areas of the envelope where the heat transfer is higher with respect to the reference value. Thermal bridges are caused by: different thermal conductivities of neighboring materials; voids, misalignment, and discontinuities of the materials; geometrical reasons such as changes in thickness or difference between internal and external areas. Depending on the building structure, the presence of thermal bridges could increase the heating demand from 5% up to 30% [5,6]. Another noteworthy drawback of the anomalous temperature distribution in the thermal bridge region is the increased risk of mold growth [7].

The on-site measurement of thermal transmittance usually relies on the heat flow meter method, as described by the ISO 9869 standard [8], that prescribes a long term monitoring campaign under strict climatic conditions to obtain a good outcome. The ideal condition would be a steady-state thermal situation with a significant temperature difference between the inner and the outer environment, as the main source of uncertainty are the operative conditions, when temperature and heat flux are unstable

due to a non-stationary regime [9]. The on-site quantification of thermal bridges requires the same conditions but is still a more open question, as a standardized methodology has not been defined at the moment. Up to now, the best efforts to measure the impact of thermal bridges relied on the application of infrared thermography [10].

However, the usual thermographic survey of a building is performed by an operator that takes few spot thermal images of the areas of interest. Long-term thermographic building surveys have been performed only in experimental cases [11–14], even if they could lead to results that are not obtainable with single spot measurements. This is related to technical and practical issues that could be typical of surveys (e.g. the limited availability of the building for the survey in terms of space and time, or the limited control on energy system operation), or distinctive issues related to thermography, such as the impossibility of leaving the instrument unattended or the need to compensate its long-term thermal drift.

Therefore many buildings surveys are performed under partially unsteady or dynamic thermal conditions, without any possible alternative. In many cases this is due also by the climate, as in several regions a stable temperature difference between inside and outside is available only in a small time window during the year or even not available at all. In other cases, is simply due to the presence of people inside the building, that frequently operate unsteady regulation of the conditioning system.

This study on thermal bridges is therefore designed to conduct a combined on-site long-term measurement of the thermal transmittance and of a thermal bridge on a wall structure, applying for the former the standard setup with contact probes and for the latter an IRT technique. The studied wall was a corner of an office, subject to realistic indoor conditions (on-off heating during business hours). The idea is taking advantage of the long term transmittance measurement, that necessarily lasts more days, to improve the accuracy of a spot thermographic measurement of the thermal bridge at different times of the day. This evaluation relies on the mathematical model of the building

6.1.1 Mathematical model

The structure of an envelope component is defined by the number, the specifications (thermophysical properties), and the order (stratigraphy) of its different layers. Opaque elements of the building envelope, such as walls or roofs, are usually the sum of two or

more layers that have different characteristics in order to execute distinct functions: finishing the external surfaces, assuring the structural integrity, or guaranteeing the thermal insulation.

From a thermal standpoint, the wall behavior is designed to decrease the heat exchange from the indoor environment to the outdoor and to shift and attenuate the thermal wave going from the outdoor to the building ambient. The former target is typical of the winter season, where the difference between outdoor and indoor temperature is usually constant during the day, while the latter is distinctive of the summer season, where the outdoor temperature trend could show wide daily oscillations. Therefore in the winter season it is possible to observe steady state thermal conditions, while in summer season it is typically noticed a dynamic building behavior. This is however a general remark that has to be checked against the climatic data of the location under survey.

The main parameter that outlines the energy performance of a building envelope in steady state conditions is the thermal transmittance (U-value), that is defined as the ratio between the heat flux density through the observed structure and the difference in environmental temperatures on both sides of the structure. When analyzing a multi-layer wall in one dimensional steady-state thermal regime, the U-value [W m^{-2} K^{-1}] is described by the following Equation 6.1 :

$$U = \frac{1}{\frac{1}{h_i} + \sum_j \frac{t_J}{\lambda_j} + \frac{1}{h_o}} \qquad (6.1)$$

where:

- h_i and h_o are respectively the indoor and outdoor values of the heat exchange coefficients [W m^{-2} K^{-1}];

- t is the thickness [m];

- λ is the thermal conductivity of the *j-th* layer [W m^{-1} K^{-1}].

This one dimensional model is not valid for all the building components: in regions where thermal bridges occur and the flow is multi-dimensional, the heat transfer is increased. The most common features are envelope corners or joints between walls and floors, where the flow becomes two-dimensional.

To assess the effect of the thermal bridge the ψ factor [15] is defined as in Equation 6.2:

$$\psi = L_{2D} - \sum_{j=1}^{N_j} U_j l_j \tag{6.2}$$

where:

- U_j is the thermal transmittance of the 1D component j separating the two environments being considered;

- l_j is the length within the 2D geometrical model over which the value Uj applies,

- N_j is the number of 1D components;

- L_{2D} is the thermal coupling coefficient obtained from a 2D calculation of the component separating the two environments being considered.

The ψ value could be calculated creating a numerical model or referring to a thermal bridge atlas [16]. Another relevant method for a two dimensional analysis is the calculation of the temperature factor f_{Rsi} for the internal surface at point (x,y) as in Equation 6.3:

$$f_{Rsi}(x,y) = \frac{T_{si(x,y)} - T_e}{T_i - T_e} \tag{6.3}$$

where:

- T_{si} is the surface temperature [K];

- T_i is the internal temperature [K];

- T_e is the external temperature [K];

6.1.2 Numerical modeling of a wall

The case study is an outer corner of an office building located in Northern Italy. The building dates back to the 1970 and has a very simple dual layer structure, typical of that construction era: a precast concrete layer and a plasterboard internal layer, as described in Table 6.1. The plasterboard layer has been reinstalled in 2014. The calculated thermal conductance of the wall is 2.38 W m^{-2} K^{-1}.

Layer	**Thickness [m]**	**Thermal conductivity [W m^{-1} K^{-1}]**
Concrete	0.16	0.58
Plasterboard	0.03	0.21

Table 6.1: Elements of the two-layer wall model

The external steel structure does not affect the considered corner. A linear thermal bridge has a uniform cross-section along one of the three orthogonal axes [15]. The study of this linear thermal bridge is therefore focused on its cross-section, that is used for a two-dimensional model. The internal length is set equal to 1 m. The numerical simulation is based on the Comsol software [17], that is verified against the standard procedure for thermal bridge modeling. The steady state conditions are chosen, imposing a heat exchange coefficient equal to 7.7 W m^{-2} K^{-1} and a temperature of 293.15 K on the inner surface and a heat exchange coefficient equal to 25 W m^{-2} K^{-1} and a temperature of 283.15 K on the outer surface. The results of Figure 6.1 show the temperature distribution across the section, that describes the impact of the thermal bridge, and the temperature profile on the inner surface, that allows the calculation of the f_{Rsi} value, that ranges from 0.78 in the undisturbed region to 0.62 in the middle of the corner. Another measure is the length of the area affected by the thermal bridge, that is equal to 0.45 m.

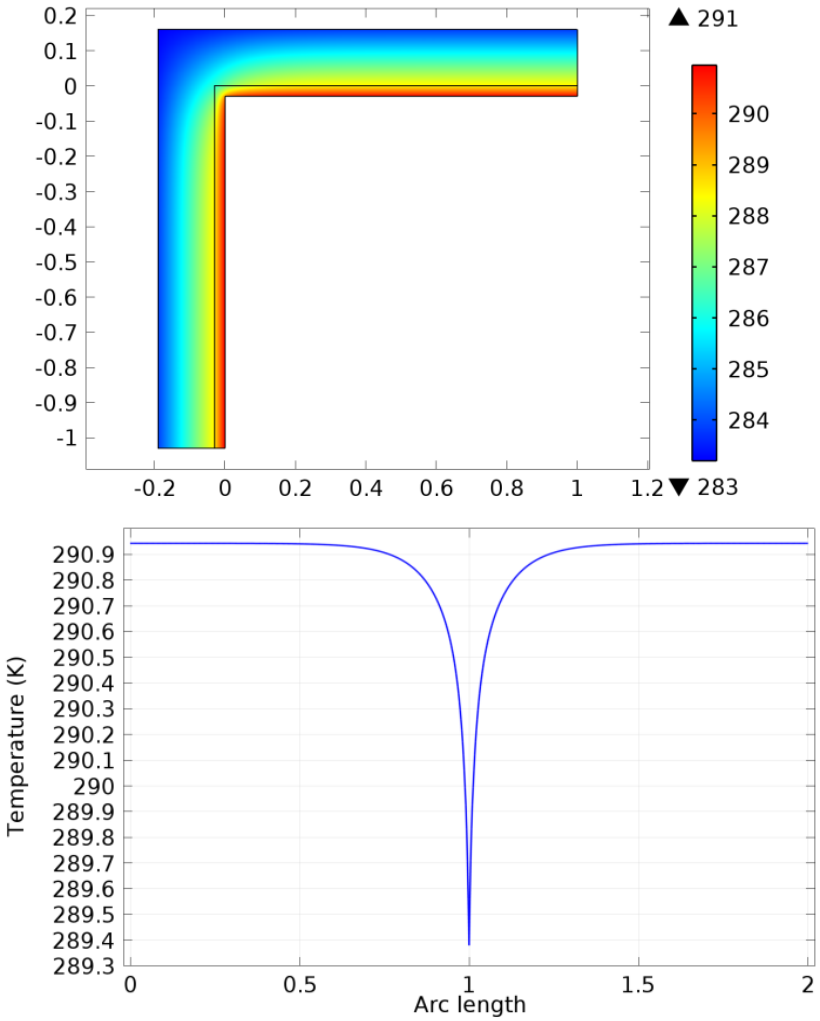

Figure 6.1: Two dimensional temperature distribution on the cross section of the thermal bridge (upper image) and surface temperature on the inner side of the wall (lower image).

6.1.3 Experimental setup

The on-site measurement was conducted during twelve days in March 2015, when the climatic conditions are switching from winter to spring. The fan-coil heating system was operational with a scheduled office time (06:30 – 19:00 from Monday to Friday) and the setpoint was raised as much as possible to increase the heat flux. The corner has one side facing southwest (left side) and another facing northwest (right side), the former is shaded by trees. The apparatus for the thermal transmittance measurement is placed on the left side wall, as shown in Figure 6.2, and is made by two surface and two air temperature probes, placed inside and outside the building, and a heat flux meter. Another air temperature probe is connected to a thermographic target, in order to compensate for the absolute temperature measurement uncertainty of the thermal camera [18].

Figure 6.2: Image of the surveyed corner as seen by the thermal camera. The left wall is facing southwest and the right one is facing northwest. On the left wall are installed the thermal conductivity measurement apparatus and the air temperature thermographic reference.

A thermal camera (FLIR SC 660, spectral response 7,5µm - 13,5µm, NETD <30 mK, 640 x 480 pixel) is placed in the room looking at the corner, acquiring an image every 5 minutes. The data acquisition rate of the camera is synchronized with the heat flux measurement apparatus. The measured emissivity value of the plasterboard surface is 0.9 ± 0.04.

6.1.4 Results

Data obtained from the thermal transmittance measurement are shown in Figure 6.3. The conditions reflect a building in use with few flexibility on the heating control strategy. The heating setpoint control has a strong influence on the internal temperature trends. The middle region with the heating on-off (Monday-Friday) was selected for the calculation of the thermal parameters.

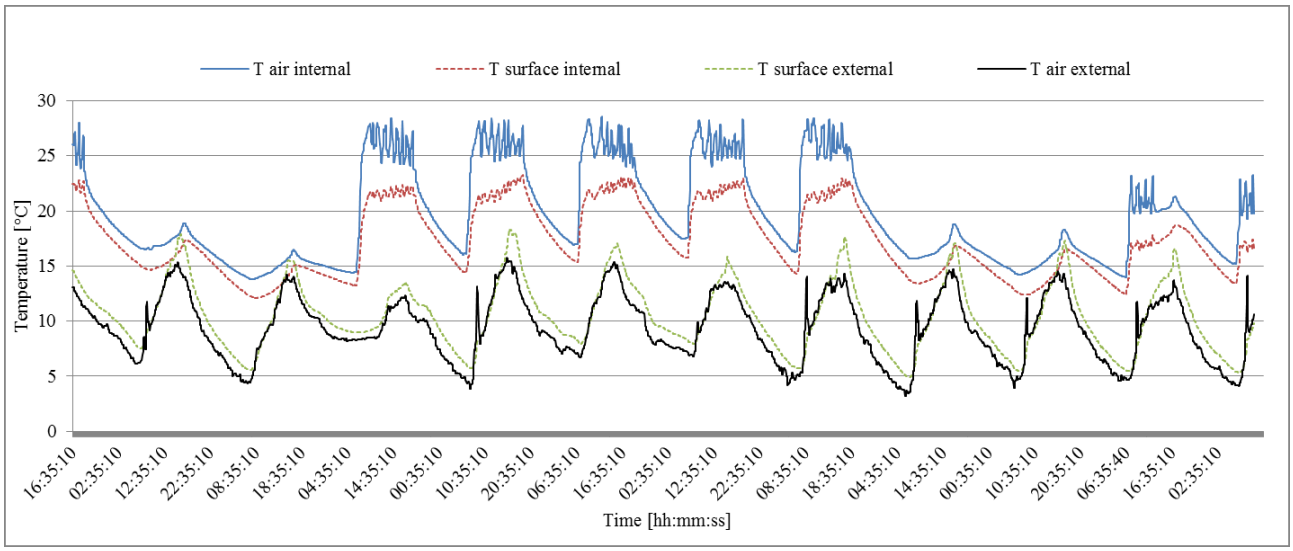

Figure 6.3: Measured temperatures over the survey period. The Monday-Friday heating pattern is clearly visible in the middle of the diagram, reflected by the internal air and surface temperature cycles.

The measured thermal conductance value of the wall, using the average method [8], is 2.2 ± 0.18 W m^{-2} K^{-1}, close to the calculated one. The instantaneous values of the thermal conductance are extremely unstable, due to the unsteady thermal conditions. However these values are comparable to the average one in the region before the heating shutdown, from 17:00 to 19:00 each day.

The thermal sequence was corrected from a thermal standpoint, on the basis of the target reference, and from a geometrical one. Each image was rectified through control points in order to account for the perspective distortion and was rescaled to the original size, obtaining straightened thermal images were one pixel corresponds to one centimeter. Selected temperature maps are shown in Figure 6.4, showing the wall status before the heating start, after the heating slope, before the end of the heating period, and after the end of the heating period. The measured walls show a good temperature homogeneity in the regions not affected by the thermal bridge, but is also visible a small thermal gradient due to the air conditioning system. The region on the upper right (window and frame) is displayed in the thermal images but it is not included in the measurement process.

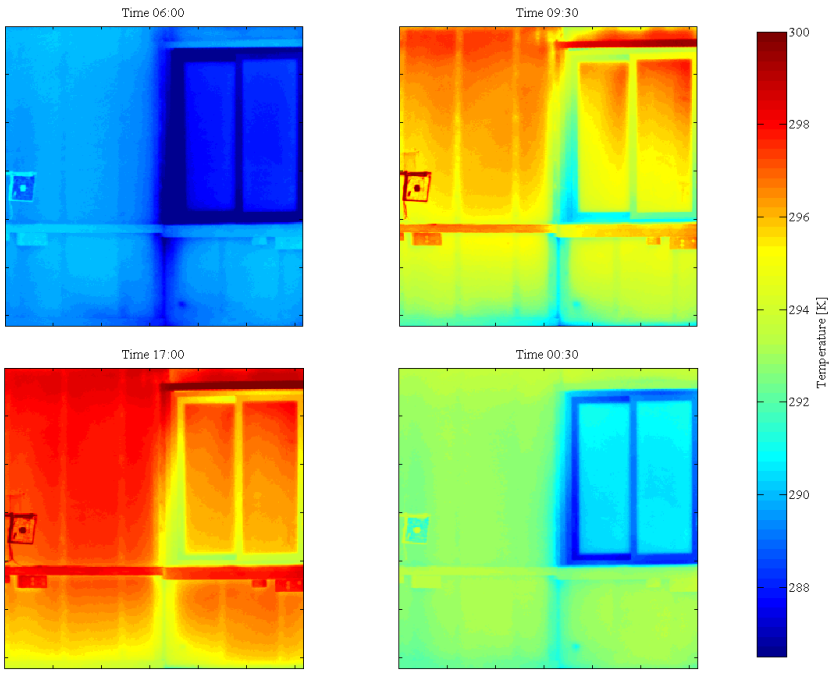

Figure 6.4: Thermal maps at different time of the day show that the temperature trend are influenced by the unstable thermal conditions.

The thermal bridge area is clearly visible in the lower part of the images. The temperature profile equivalent to the simulated cross section was chosen at the height of 0.5 m. After the geometrical correction it is possible to verify that the area affected by the thermal bridge is equal to 0.45 m, as in the simulated case. Equation 6.3 allows to calculate the f_{Rsi} factor for each point of the surface, as shown in the next Figure 6.5 for a timestamp in the late afternoon.

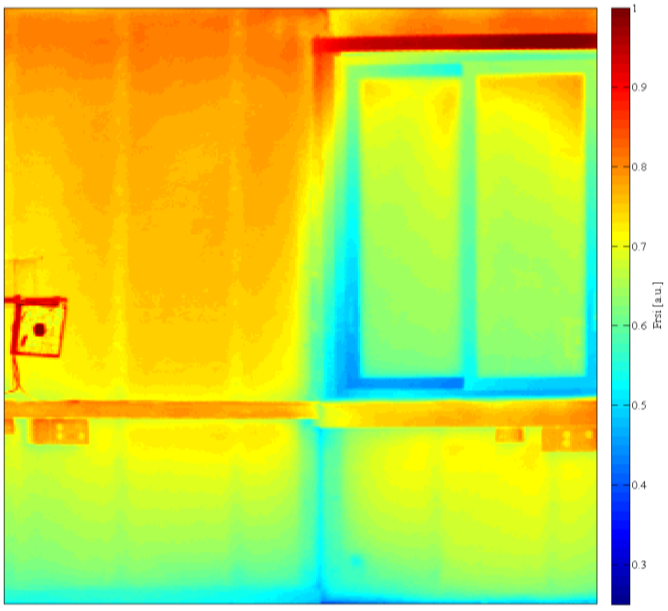

Figure 6.5: f_{Rsi} map before the heating shutdown. The obtained values are close to the simulated ones.

The measured f_{Rsi} values are far from the simulated values (0.78 in the undisturbed region to 0.62 in the middle of the corner) when the heating is off, but are observed at the end of the heating period. This is highlighted by the plot of the f_{Rsi} of Figure 6.6, where the trends over time of an undisturbed point and of a point in the middle of the thermal bridge are displayed. As seen also for air temperature trends, the values are affected by the heating setpoint control.

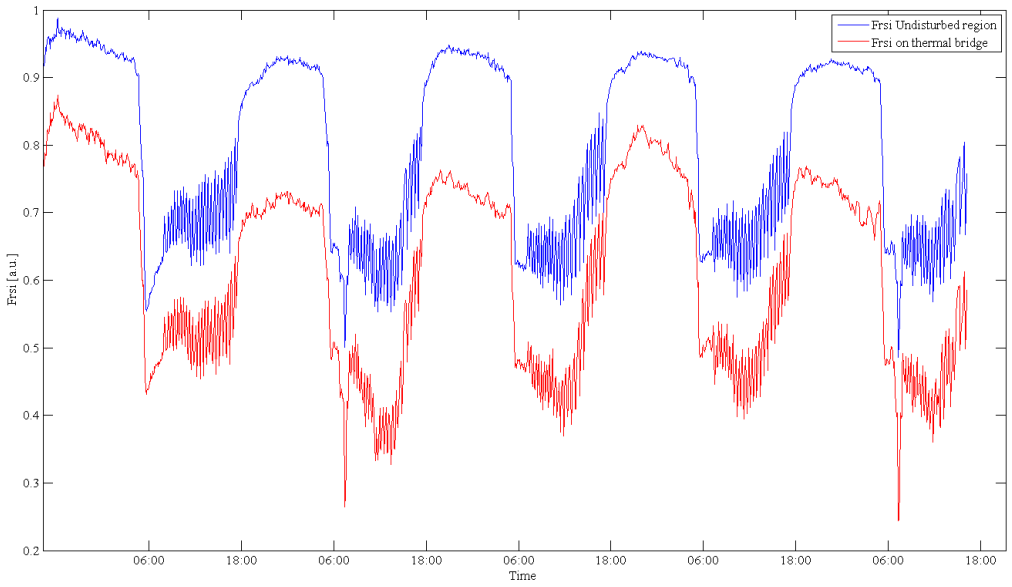

Figure 6.6: . f_{Rsi} maps at different time of the day. The unsteady thermal conditions leave a small timeframe where the simulated values are close to the measured ones.

A significant underestimation of the thermal bridge is made if the values are taken when the heating is off or at the beginning of the heating cycle. The error is instead lower than 10% if a correct timeframe is selected, based on the data acquired by the heat flux meter.

The proposed experimental setup with a thermal camera acquisition of multiple days is not applicable in most real cases. However, the heat flux meter setup is becoming more and more viable and affordable over time. A long-term heat flux measurement, as needed by the standard, could therefore help the infrared inspection in selecting the best time for a single shot measurement. While the on-site characterization of thermal transmittance is well regulated, the quantification of thermal bridges is still open to improvements. The obtained results have shown that the length of the thermal bridge could be assessed correctly and also the f_{Rsi} value is measurable, if the correct timing is chosen. Future work will reproduce the measurement on different wall configurations and will try to integrate also climate forecasting to preview the optimal inspection timing.

6.2 Evaluation of thermal transmittance

The evaluation of thermal transmittance (U-value) is of great interest, as this parameter has a major influence on the thermal behavior of the building and, consequently, on its energy consumption. Several thermographic strategies were proposed by different authors [19,20]; the following relies on an accurate one-side thermographic measurement complemented by an air temperature measurement.

6.2.1 Simplified physical model

In case of steady thermal state, the heat flux across the building envelope could be evaluated according to the following Equation 6.4:

$$\frac{Q}{S} = q = h_i(Ta_i - Tw_i) = h_i\, \Delta Ta_i w_i = \frac{\lambda}{l}\Delta Tw_{i,o} = h_o \Delta Tw_o a_o \qquad (6.4)$$

where:

q is the thermal flux [W m^{-2}];

Q is the thermal power [W];

S is the surface [m];

h is the heat exchange coefficient [W m^{-2} K^{-1}];

T_a is the air temperature [°C];

T_w is the wall temperature [°C];

Δ Is a temperature difference [°C];

λ is the thermal conductivity [W m^{-1} K^{-1}];

l is the thickness of the wall [m];

the subscripts i and o stand respectively for inner and outer.

The convective heat transfer inside the room can be considered natural and buoyancy drives the air motion.

The convective flux can be estimated as follows in Equation 6.5:

$$q^c = \alpha_i(T_a - T_w) = \alpha_i \Delta T a_i w_i \quad (6.5)$$

where:

q^c is the convective heat flux [W m^{-2}];

α is the convective heat exchange coefficient [W m^{-2} K^{-1}].

Supposing that heat exchange coefficient is constant across the space, the thermal transmittance is therefore given by the next Equation 6.6:

$$U(x,y) = h_i \frac{Ta_i(x,y) - Tw_i(x,y)}{\overline{Ta_i} - \overline{\overline{Ta_o}}} \quad (6.6)$$

where:

- *U(x,y)* is the thermal transmittance for each point in the (x,y) space [W m^{-2} K^{-1}]

- *T(x,y)* is the temperature for each point in the (x,y) space [°C];

- T_{ai} is the space-averaged inner air temperature [°C];

- T_{ao} is the time-averaged outer air temperature [°C].

6.2.2 Experimental setup

A jacket – type climatic chamber is part of CNR-ITC facilities in Padova, a more accurate description is presented in the following 6.4.1. The controlled air volume, around 130 m^3, is maintained at a desired temperature through a dedicated HVAC unit. Inside this room an insulated chamber has been installed, with an inside volume equal to 40 m^3. This inner room has been built with sandwich panels typical of the cold storage. Two radiant systems, one in the floor and another in the ceiling, and a set of ten thermal dummies enable the user to set accurately the air temperature of the room. One of the walls of this room is the object of the analysis, more specifically the one with the entry door and the eastern orientation. The wall is 70 mm thick and is made by a polyurethane layer inserted between two fiberglass layers as described in Table 6.2.

Layer	Thickness [m]	Thermal conductivity [W m^{-1} K^{-1}]
Fiberglass	0.001	0.22
Polyurethane	0.068	0.023
Fiberglass	0.001	0.22

Table 6.2: Materials of the measured walls.

The entry door has the same stratigraphy but a thicker polyurethane layer that is equal to 0.1 m. The measured area of the wall is equal to 7.65 m^2, including the door. Emissivity of these kind of walls has been evaluated in [10].

A broad network of sensors has been installed inside the rooms with a dedicated datalogging system developed in Labview environment. PT 100 contact temperature probes have been installed inside and outside every wall of the inner room. Moreover twelve PT 100 air temperature probes have been positioned in different points of the rooms and two thermal heat flux meters have been placed, one on the west wall and another on the ceiling.

6.2.3 Results

The test can last several days, as the calculated thermal transmittance of the wall is very low. Considering a global heat transfer coefficient equal to 7.7 W m^{-2} K^{-1}, the obtained value for transmittance is around 0.3 W $m^{-2}K^{-1}$. The air temperature of the inner and outer rooms are regulated in order to keep, in steady state, a difference of at least 10 K between each other.

The thermographic apparatus captures several thermal images, that are geometrically corrected and mosaicked (Figure 6.7), where each pixel corresponds to one centimeter.

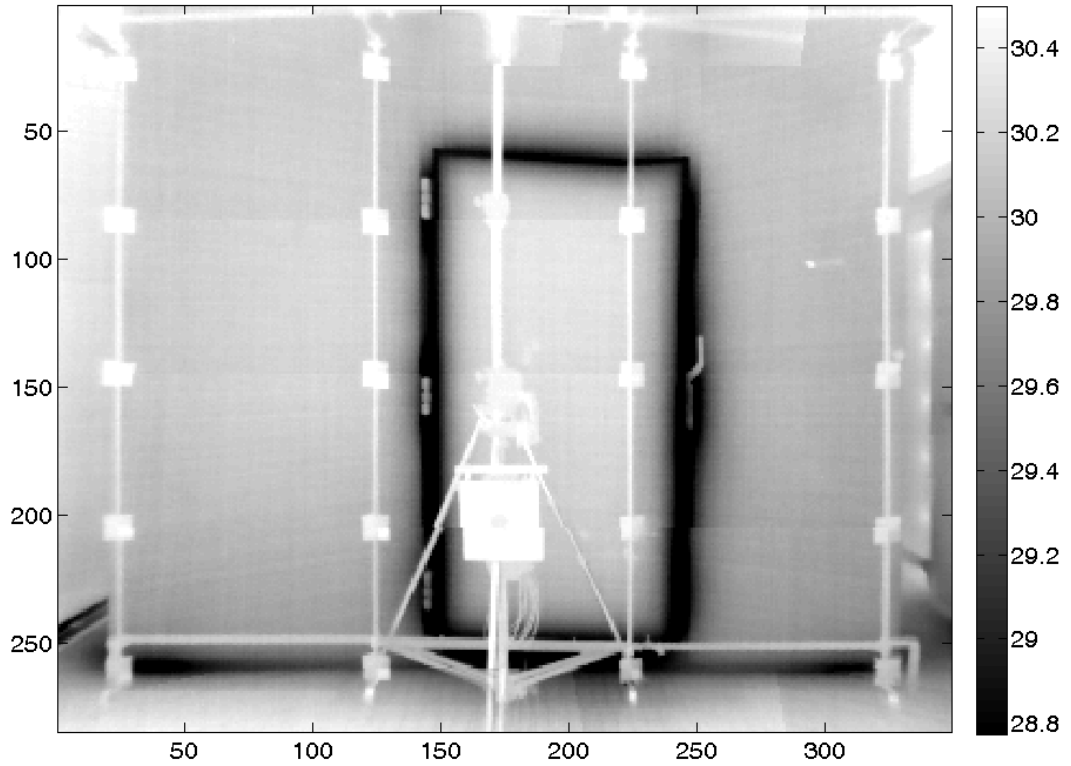

Figure 6.7: Thermal mosaic of the surface temperature of the wall.

This process is based on a special grid of infrared targets that is installed near the wall. The grid allows also the mapping of the air temperature (Figure 6.8).

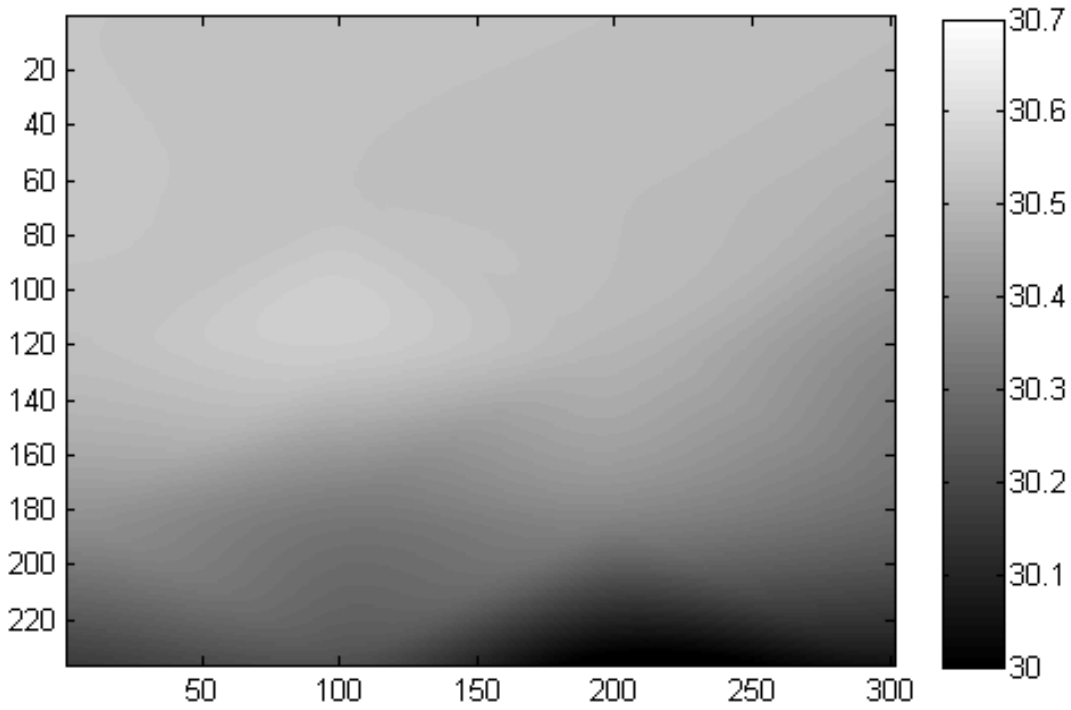

Figure 6.8: Distribution of air temperature on a virtual surface near the wall.

The calculation of the thermal transmittance value derives from the physical model presented in the previous chapter. The distributed mapping shows all the variation of this value along the wall (Figure 6.9).

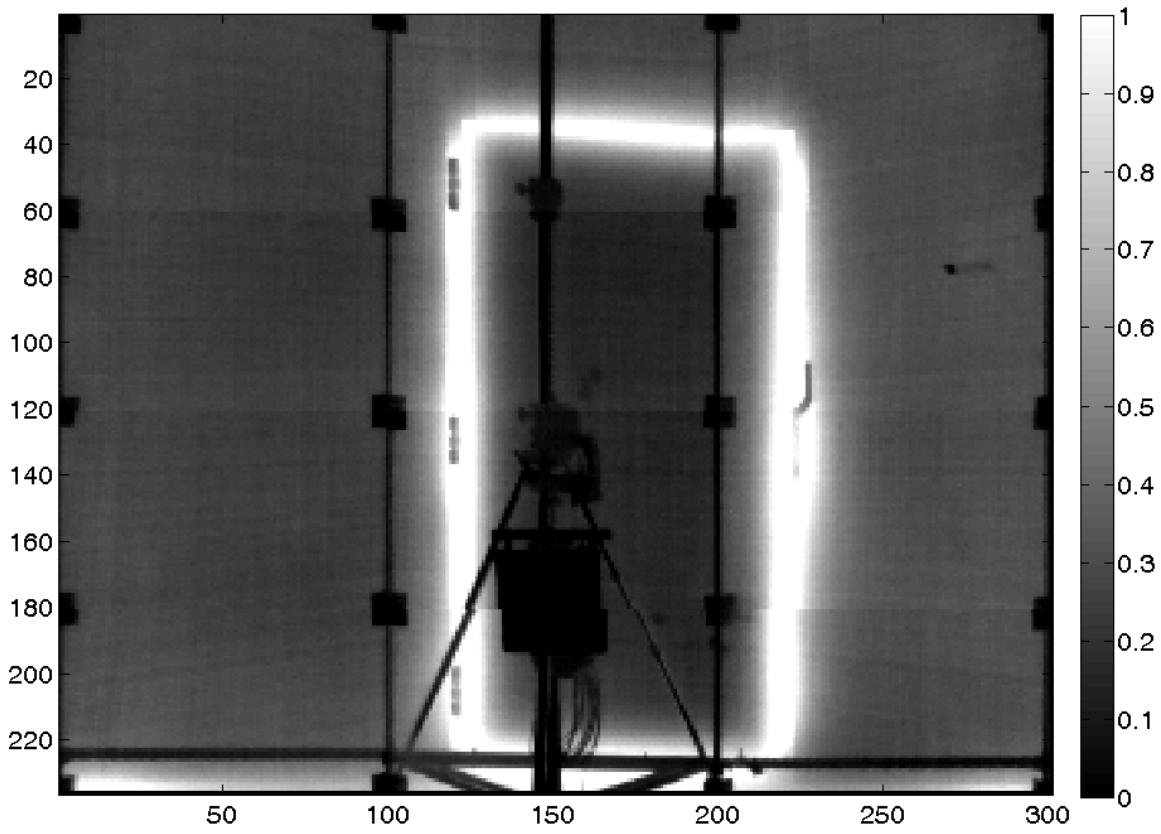

Figure 6.9: Map of thermal transmittance derived from the thermographic measurements.

One of the main advantages of infrared thermography is the possibility to locate and quantify anomalies and thermal bridges. Therefore in order to compare this technique to the heat flux meter, that is substantially a spot measure, an area of the map has been selected excluding the door and thermal bridges. The comparison of results (Table 6.3) shows that the heat flux meter overestimates the calculation value, whereas the thermographic method underestimates it.

Technique	U - Value [W m^{-2} K^{-1}]	Difference from calculation [W m^{-2} K^{-1}]
Calculation	0.30	0
Heat flux meter	0.36	+ 0.057
Infrared Thermography	0.27	- 0.027

Table 6.3: Comparison of results for thermal transmittance of the wall.

The thermal properties of walls, especially transmittance, are fundamental for the evaluation of the overall building performance. The on-site measurement of thermal transmittance is usually carried on with the heat flux meter method. This paper has shown that infrared thermography advanced methods can give accurate results of this parameter and add significant information about the localization and magnitude of defects and thermal bridges.

6.3 Evaluation of dynamic building behavior

The insulating layer has a role also in periodic thermal conditions, typical of the summer season. The periodic thermal stimulus that stresses the outer side of a wall reaches the inner surface of the wall, delayed and attenuated depending on the structure of the wall. In this case the main physical parameters are the thermal diffusivity and the thickness of the wall, that affect the periodic thermal transmittance and the time shift as defined by the standard [21]. The type and the position of the insulating material inside the wall stratigraphy can improve both energy efficiency [22] and thermal comfort [23]. The dynamic thermal behavior of well insulated buildings has a significant impact both on heating and cooling energy demand [24]. However the energy savings predicted during the design stage should always be checked with an on-site survey. Significant discrepancies from theoretical values (up to 30%) can be found after the application of the energy saving strategies due to several reasons, ranging from incorrect design to poor workmanship [25], even when applying the best practices [26]. The on-site steady state thermal behavior of the building is frequently measured thanks

to its well-established standard procedure. On the contrary, the verification of the dynamic behavior is usually neglected, due to the lack of a feasible procedure.

This work is aimed to fill the gap, proposing a method that could survey wide areas of the walls and could be applicable also on-site, based on Infrared Thermography. In the field of non - destructive evaluation, infrared thermography is commonly used to determine the thermal diffusivity of materials [27,28], the basic thermal parameter that affects the dynamic behavior of walls, with different experimental layouts [29]. However the standard techniques are available for very small specimen and some theoretical and practical barriers must be overcame in order to measure thick, wide, and multilayered building walls.

The proposed experimental setup is aimed to reproduce the real environmental conditions of an external wall during a daily temperature swing. A lamp generates a sinusoidal thermal stimulus on the back of a wall specimen. A thermal camera measures directly the temperature oscillation on the front of the specimen and indirectly (looking at a thermal mirror) the temperature oscillation on the back of the specimen. The temperature lag is then derived as the difference between the times where the temperature peaks occur on the surfaces. The feasibility of the proposed procedure was preliminary assessed by a mathematical analysis.

6.3.1 Mathematical model

During the summer season, a wall is usually stimulated by the sun, that could be considered as a periodic heat source. The Fourier analysis of this stimulus would lead to the identification of the first main sinusoidal component, with a period equal to 24 hours (Figure 6.10). The temperature variation on the stimulated (outer) side of the wall is transferred through the wall to the internal surface, that shows a periodic temperature oscillation that is time-shifted and attenuated with respect to the original signal.

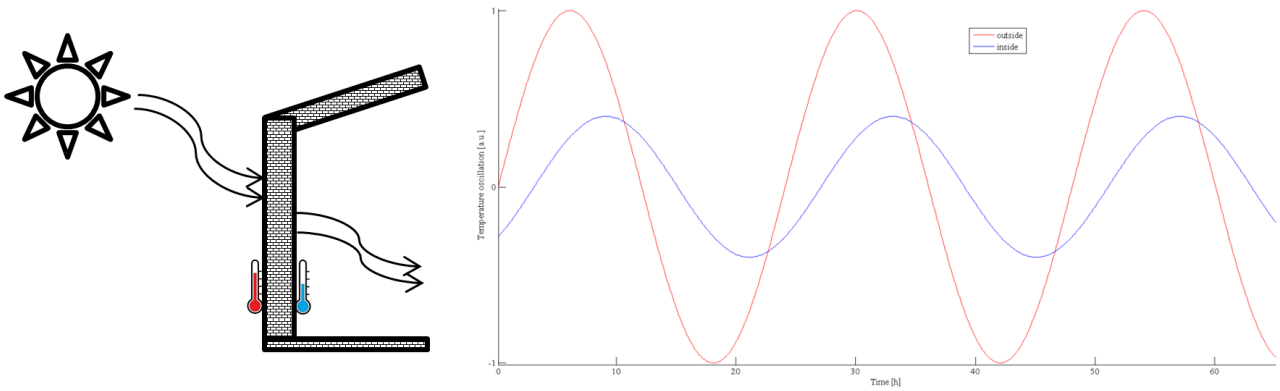

Figure 6.10: The periodic thermal stimulus of the sun on the outer surface of the wall (red temperature probe) is visible, with a time-shift and an attenuation, as a periodic temperature variation on the inner side of the wall (blue temperature probe).

This problem is usually modeled with a one-dimensional equation [21,30] as in the following Equation 6.7:

$$\frac{\partial^2 T(x,t)}{\partial x^2} = \frac{1}{\alpha}\frac{\partial T(x,t)}{\partial t} \tag{6.7}$$

where:

- T is the temperature at position x [K];

- t is the time [s];

- α is the thermal diffusivity [$m^2 s^{-1}$].

The relation 6.8 that gives the value of the thermal conductivity is:

$$\alpha = \frac{k}{\rho c_p} \tag{6.8}$$

where:

- k is the thermal conductivity [W m^{-1} K^{-1}];

- ρ is the volumic mass [kg m^{-3}];

- c_p is the specific heat [J kg^{-1} K^{-1}].

The heat flux at any position x and time t is given by Equation 6.9:

$$q(x,t) = -k\frac{\partial T(x,t)}{\partial x} \tag{6.9}$$

In both equations, k, ρ, and c_p are assumed to be constant. This equation could be solved using the Laplace transform, that changes this partial differential equation into an ordinary differential equation.

Considering only the temperature and heat flux at the surfaces of the wall of thickness ℓ, it is possible to rewrite the boundary terms. $T_1(s)$ and $T_2(s)$ are equal to $T(0,s)$ and $T(l, s)$, which are the transform of the temperature at the inner and outer surfaces respectively. $q_1(s)$ and $q_2(s)$ are equal to $q(0,s)$ and $q(l, s)$, which are the transform of the heat flux at the inner and outer surfaces respectively.

The values of $T_1(s)$ and $q_1(s)$, where s is a complex number, are the following Equations 6.10 and 6.11:

$$\mathrm{T}_1(s) = \left(\cosh(\ell\sqrt{s/\alpha})\right) T_2(s) + \left(\frac{1}{k\sqrt{s/\alpha}}\sinh\left(\ell\sqrt{s/\alpha}\right)\right) q_2(s) \tag{6.10}$$

$$\mathrm{q}_1(s) = \left(\mathrm{k}\sqrt{s/\alpha}\,sinh\left(\ell\sqrt{s/\alpha}\right)\right) T_2(s) + \left(\cosh\left(\ell\sqrt{s/\alpha}\right)\right) q_2(s) \tag{6.11}$$

For notational convenience, we may now define new variables as follows in Equations 6.12:

$$\begin{aligned} \mathrm{A}(s) &= \cosh(\ell\sqrt{s/\alpha}) \\ \mathrm{B}(s) &= \frac{1}{k\sqrt{s/\alpha}}\sinh\left(\ell\sqrt{s/\alpha}\right) \\ C(s) &= \mathrm{k}\sqrt{s/\alpha}\,sinh\left(\ell\sqrt{s/\alpha}\right) \\ D(s) &= \cosh\left(\ell\sqrt{s/\alpha}\right) \end{aligned} \tag{6.12}$$

With these new variables, Eq. 6.10 and 6.11 become Eq. 6.13 and 6.14:

$$\mathrm{T_1(s)} = \mathrm{A(s)T_2(s)} + \mathrm{B(s)q_2(s)}, \mathrm{B(s)} \neq 0 \tag{6.13}$$

$$\mathrm{q_1(s)} = \mathrm{C(s)T_2(s)} + \mathrm{D(s)q_2(s)} \tag{6.14}$$

We can rewrite these equations in matrix form as Equation 6.15:

$$\begin{bmatrix} T_1(s) \\ q_1(s) \end{bmatrix} = \begin{bmatrix} A(s) & B(s) \\ C(s) & D(s) \end{bmatrix} \begin{bmatrix} T_2(s) \\ q_2(s) \end{bmatrix} = [Z] \begin{bmatrix} T \\ q \end{bmatrix} \tag{6.15}$$

where *Z* is the transfer matrix of the single layer.

For a multilayer building component, the overall transfer matrix is the product of each layer matrix as in Eq. 6.16:

$$\mathrm{Z} = \mathrm{Z_N} \cdot \mathrm{Z_{N-1}} \ldots . \mathrm{Z_3} \cdot \mathrm{Z_2} \cdot \mathrm{Z_1} \tag{6.16}$$

where Z_1, Z_2, Z_i,..., Z_N, are the transfer matrices of the different layers, beginning from layer 1. Layer 1 is conventionally the internal layer.

The transfer matrix from environment to environment through the building component is given by Eq. 6.17:

$$\mathrm{Z_{tot}} = \mathrm{Z_{b2}} \cdot \mathrm{Z} \cdot \mathrm{Z_{b1}} \tag{6.17}$$

where Z_{b1} and Z_{b2} are the transfer matrices of the boundary layers, given by Eq. 6.18:

$$Z_b = \begin{bmatrix} 1 & -R_s \\ 0 & 1 \end{bmatrix} \tag{6.18}$$

where R_s is the surface resistance [m^2 K W^{-1}] of the boundary layer, that includes both convection and radiation. Values of this parameter are available in [31].

Each element of the *Z* matrix is therefore a complex number that could indicate the effect of a temperature or flow heat variation on a surface caused by the stimulation of the opposite surface or the time delay between cause and effect. The time delay Δt_{ij}

between the maximum of an effect and its corresponding cause is calculated from the phase-shift φ_{ij} of the transfer matrix element Z_{ij}, as in the following Equation 6.19:

$$\Delta t_{ij} = \frac{\tau}{2\pi}\varphi_{ij} = \frac{\tau}{2\pi}\arg(Z_{ij}) \quad (6.19)$$

where τ is the period [s].

6.3.2 Materials and methods

Two kind of samples were prepared for the experimental measurement. The first one was a single slab of plasterboard sizing 0.64 m^2. The size was chosen to facilitate the preliminary testing and optimization of the experimental layout. A further limit on the specimen width was established by the size of the thermal conductivity apparatus. The plasterboard slab was also a part of the second specimen, where a layer of insulating material was sandwiched within two plasterboard slabs. Three insulating materials were tested: Aerogel, Expanded Polystyrene (EPS), Polyurethane. The thickness and thermal properties (thermal conductivity, specific heat, volumic mass) of the different materials were measured in laboratory and are reported in Table 6.4. The thermal conductivity was measured with a Taurus TLP 800 guarded hot-plate device [32]. The specific heat of small material samples was measured with a Setaram Differential Scanning Calorimeter [33]. The volumic mass was measured with the buoyancy method [34]. The thickness was measured with a Mitutoyo 500 Caliper. The uncertainty values are obtained from the standard deviation of multiple measurements and through the propagation of errors [35,36]. The thermal properties are required to calculate accurately the phase-shift of the specimens.

Material	**Thermal conductivity [W m^{-1} K^{-1}]**	**Specific heat [J kg^{-1} K^{-1}]**	**Volumic mass [kg m^{-3}]**	**Thickness [m]**
Plasterboard	0.227 ±0.007	1000 ±50	820 ±20	0.0125 ±0.0001

Aerogel	0.0187 ±0.0006	1200 ±70	175 ±5	0.0050 ±0.0001
EPS	0.040 ±0.002	1140 ±70	17 ±1	0.0600 ±0.0001
Polyurethane	0.0259 ±0.0005	1530 ±40	44 ±2	0.0500 ±0.0001

Table 6.4: Thermal properties of the tested materials. Uncertainty values are obtained from the standard deviation of multiple measurements and through the propagation of errors.

Different layouts were considered for the experiment, as shown in Table 6.5. The easiest setup consists in installing two contact temperature probes (e.g. thermocouples or resistance temperature detectors), one on the front surface and one on the back surface of the specimen. This is the less expensive configuration, as only two low-cost probes and a datalogger are required. It could be limited in the outcome, as the installation of contact probes is frequently critical from a thermal (creation of a contact resistance between the probe and the surface, measurement on a single point) and practical standpoint: in several cases (e.g. cultural heritage, listed buildings) this configuration is not allowed. Different approaches involve infrared thermography, that as an optical contactless technique could overcome most of the previous issues. The first thermographic procedure consists in a thermal camera measuring at the same time the temperature oscillation on the front and on the back surface, thanks to a thermal mirror that reflects the signal of the back surface. This was the selected layout, as a differential temperature measurement with a single camera optimizes the reliability of the infrared measurement. Limitations in positioning the setup are evident, but the number of places where this test could be performed in a traditional building is high (e.g. near every window), taking care of the possible impact of thermal bridges. The analysis of mock-up walls in laboratory environment is not affected by these limitations. The setup is more expensive but can provide a higher number of measurement points than the contact surface sensor, reaching a similar performance if the comparison is based on the ratio between measurement point and costs. The last thermographic setup that was analyzed consists in two thermal cameras, one looking at the front and one at the back surface of the wall. This setup would give the highest number of measurement points but was discarded due to its excessive costs and to the practical difficulties in positioning the outside camera and synchronizing it to the indoor one.

Method	Surface sensors	Thermography and mirror	Thermography dual camera
Equipment	Two temperature probes, datalogger	One thermal camera	Two thermal cameras
Experimental layout	One probe on inner surface, one on outer, both connected to datalogger	Thermal camera measuring the inner surface and the mirror	One thermal camera for the inner surface, one for the outer, synchronized
Advantages	Ease of setup, low costs	Ease of processing, one sensor measurement, area measurement	Wider area measurement, few positioning limitations
Disadvantages	Spot measurement, thermal inertia of the probes	Medium costs, positioning limitations	Higher costs, difficult processing

Table 6.5: Comparison of possible experimental layouts. The proposed solution is the best tradeoff between the obtainable results and the technical feasibility.

For the selected layout (single camera), the thermal source was a 1 kW lamp that was controlled with a customized software. The lamp delivered a sinusoidal heating on the back surface of the sample with an amplitude equal at most to the 60% of the lamp power and with a maximum period of 2 hours. A FLIR SC660 thermal camera (spectral response 7,5μm - 13,5μm, NETD <30 mK, 640 x 480 pixel) was placed towards the front size of the sample, looking also at a thermally reflective mirror (aluminum foil). The reflective mirror was placed in a direction that optimized the reflected temperature of the back surface of the specimen (Fig. 2).

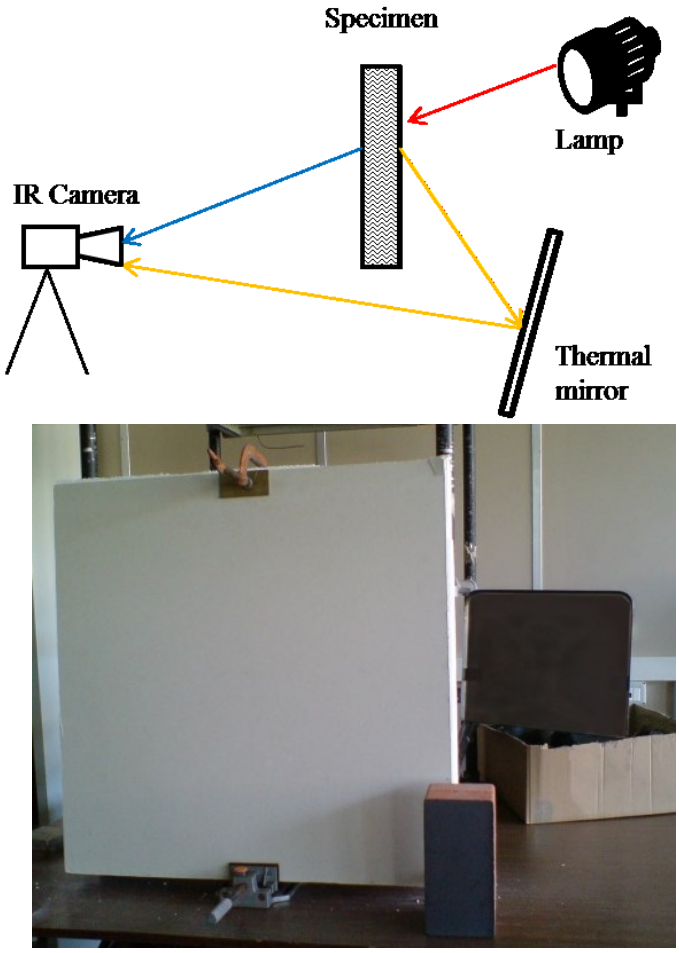

Figure 6.11: Diagram of the experimental setup and photography as seen by the thermal camera (front surface). The white specimen (plasterboard) is heated by a modulated lamp placed behind it. The oscillation of the back surface temperature over time is reflected by the mirror element and acquired by the thermal camera.

The data acquisition began with some images before the thermal stimulation (cold images). Four markers were placed on the front and back surfaces in order to verify the camera alignment and focus. The markers were used also to define the measurement area. Successively the lamp was turned on and the data were acquired for at least three entire periods where the mean amplitude value was stable. The ambient temperature of the test room was maintained constant (±1.5 °C) during the experiment.

6.3.3 Results

Four specimens were tested with a sinusoidal thermal stimulation; each experiment was repeated three times. The first test was aimed to verify the experimental setup with a fast acquisition. The following tests were aimed to verify the procedure on samples that resembled a real internal wall. The period and the intensity of the heating wave, and the camera acquisition framerate were chosen depending on the specimen. The temperature profile of the central area on front and back layer were extracted from the

thermal sequence. The data were centered, scaled and fitted with a sinusoidal model [37]. The time-shift was calculated on the last period as the time difference between the maximum value recorded on the front and on the back surface of the sample (Eq. 6.20).

$$\Delta t_{meas} = t\left(T_{max,front}\right) - t\left(T_{max,back}\right) \tag{6.20}$$

The temperature measurement was therefore differential, exploiting at best the possibilities of the thermal camera. This modality facilitates the experimental setup, as the knowledge of the absolute temperature value is not needed, avoiding difficult calibration procedures. Moreover the thermal reflective element could be made with low cost materials (e.g. aluminum foils). The measured temperature evolution over a complete thermal cycle is illustrated in Figure 6.12.

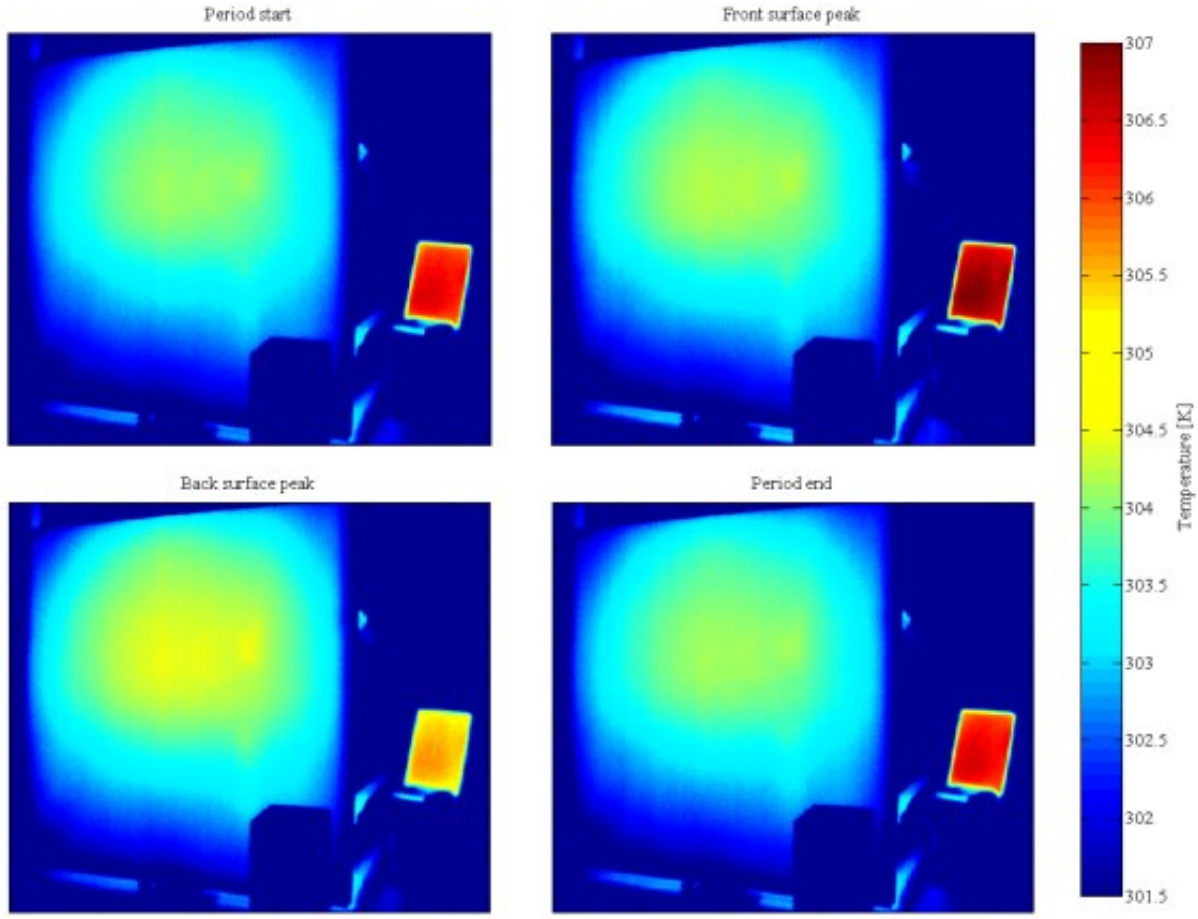

Figure 6.12: Thermal images during the main steps of the sinusoidal thermal oscillation. After the initial image of the cycle, taken at the middle of the heating cycle (Period start), the temperature on the reflecting mirror reaches its maximum value (Front surface peak). The signal is then visible, with attenuation and delay, on the opposite surface (Back surface peak). Afterwards the sample returns to the initial condition (Period end, that is equal to Period start).

A first experiment was performed with a stimulation period equal to 5 minutes on a plasterboard slab and compared to the calculated time shift, as shown in Table 6.6.

The thermal camera sampling rate was lower than the 0.5% of the expected time-shift, in order to make the time sampling error negligible. Higher rates would lead to an excessive amount of data. The sampling rate was equal to 2 Hz for the first experiment and to 0.33 Hz for the others.

Sample	**Measured time-shift [min]**	**Calculated time-shift [min]**
Plasterboard	143 ± 2	151 ± 6

Table 6.6: Measured versus calculated time-shift values on a plasterboard slab with a stimulation period equal to 10 minutes.

The uncertainty value of the measured time-shift were obtained from the standard deviation of multiple measurements. The uncertainty value of the calculated time-shift was based on the experimental uncertainty of the measured thermal properties (thermal conductivity, specific heat, volumic mass, thickness). A worst-case procedure was applied, taking the highest errors on the measures and calculating the corresponding time-shift value. This approach is conservative and could lead to overestimate the error.

The second experiment was performed on sandwiches made by two external plasterboard slabs and one internal insulating layer. The results obtained with a stimulation period equal to 2 hours are reported in Table 6.7.

Sample	**Measured time-shift [h]**	**Calculated time-shift [h]**
Plasterboard +Aerogel +Plasterboard	0.36 ± 0.02	0.40 ± 0.03
Plasterboard +EPS +Plasterboard	0.44 ± 0.02	0.44 ± 0.04

Plasterboard +Polyurethane +Plasterboard	0.63 ± 0.04	0.66 ± 0.05

Table 6.7: Measured versus calculated time-shift values on Plasterboard sandwiches with a stimulation period equal to 2 hours.

The results show an increasing trend in time-shift, that is consistent with the mathematical model. The best agreement is obtained for EPS and Polyurethane that are delivered in rigid slabs, easing the experimental layout.

The experimental results demonstrate the potential of the proposed technique in the perspective of an on-site survey, where thick walls and solar power will lead both to higher time-shifts and temperature oscillations than the ones measured in this work, increasing the accuracy of the measurement. The knowledge of the building dynamic thermal behavior through an on-site measurement will improve the construction sector in two ways. Firstly the verification of the theoretical value will emphasize the design phase, where the architects and engineers involved in the project should take great care in choosing the correct wall stratigraphy. In the second instance the construction companies will receive a direct feedback on their work.

6.4 Evaluation of radiant heating systems

A detailed analysis of a building should encompass also an investigation of the HVAC system. From a thermographic standpoint, an interesting application is the study of radiant heating and cooling systems. Radiant heating and cooling systems have been applied to domestic heating since ancient times [38] and are currently a common alternative to radiators and fan coils. Two main categories are available, defined on the heat transfer medium: hydronic systems and electrical ones. This work is focused on hydronic systems, that have the highest market share in Italy, but the methods and procedures that will be described in the next sections may be applied, with adjustments, also to electrical systems, that currently represent a market niche.

6.4.1 Radiant system testing facility

Since 2010, the ITC-CNR laboratory in Padova hosts a test facility for radiant heating and cooling systems. The experimental apparatus was extended after its creation and it can

now test both small prototypes (inside a climatic chamber) and real scale installations, inside an industrial building. The climatic chamber that is used for prototype testing is an air jacket-type test room, with an internal volume of 130 m^3, that contains a smaller room sizing 40 m^3(in agreement with the EN 14240 specifications [39]). The outer room is controlled by a dedicated air treatment unit that supplies hot or cold air through the jacket. Outside the room, a two circuit hot and cold water generation system is installed. The generation system and the room are arranged to test both floors and ceilings, in summer or winter conditions. For summer conditions, 10 thermal dummies [39] are available to generate the heat load required by the standard. The following Figure 6.13 shows the thermal dummies during a radiant ceiling testing.

Figure 6.13: Thermal dummies inside the test room during the performance measurement of a radiant cooling system.

A centralized data acquisition system, based on a custom software developed in Labview environment, connects the different sensors listed in Table 6.8 and in Table 6.9.

Measurement type	Sensor	Number of probes
Water temperature	Platinum RTD	12
Water flow	Magnetic flow meter	2
Electrical power	Voltage and current meter	1
Pressure	Manometer	4

Table 6.8: Sensors installed on the hydronic system.

The water temperature probes are placed in various point of both the hydraulic circuits, as shown in the following Figure 6.14. Two temperature probes are always installed as near as possible to the inlet and outlet of the tested specimen.

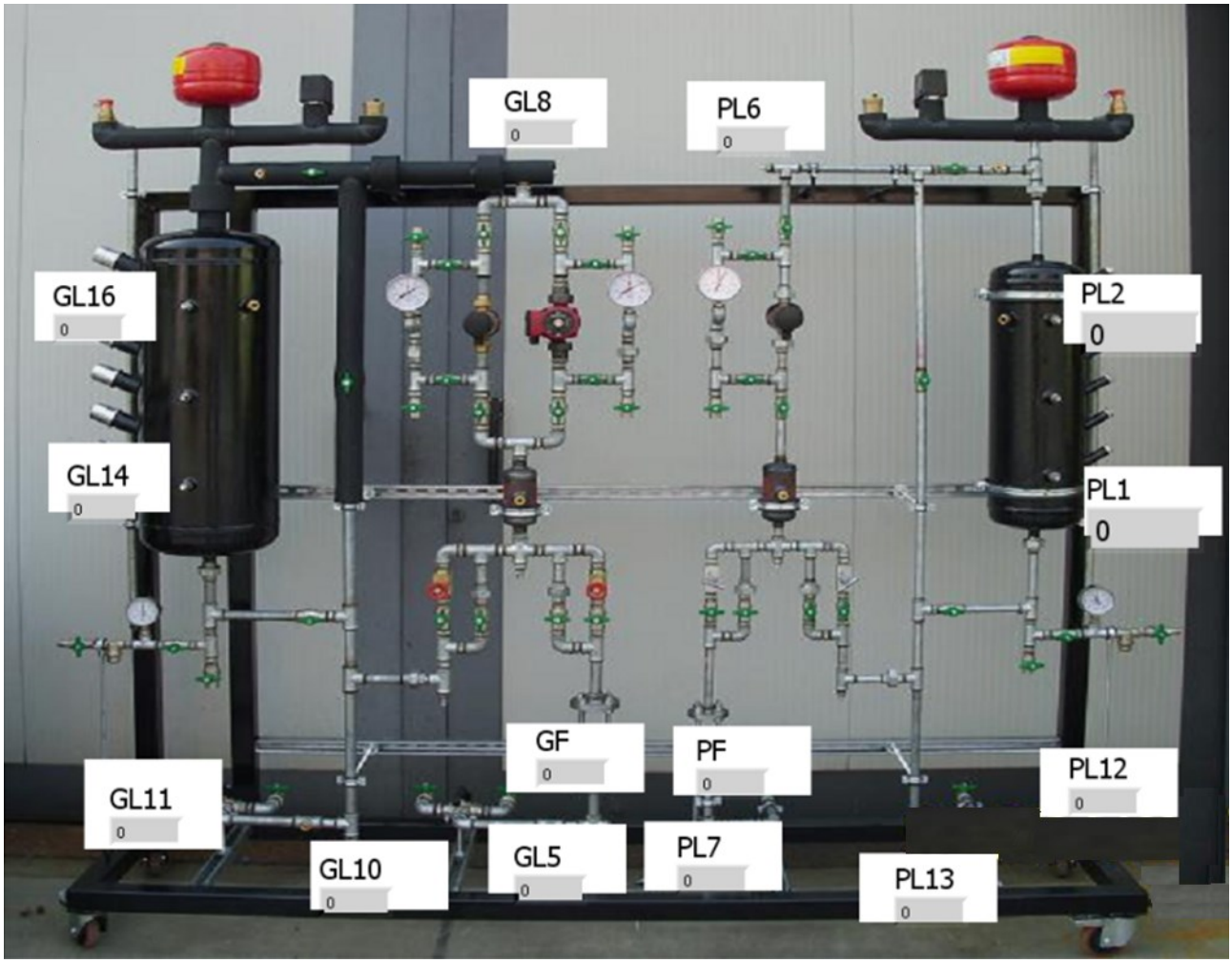

Figure 6.14: User interface (basic version) of the custom data acquisition software. The two hydraulic circuits are named “G” and “P” respectively.

Measurement type	Sensor	Number of probes
Water temperature	Platinum RTD	2
Surface temperature	Platinum RTD	14
Air temperature	Platinum RTD	12
Mean Radiant temperature	Globe thermometer	2
Air humidity	Hygrometer	1
Air velocity	Hot-film anemometer	4
Heat flux	Heat flux meter	3

Table 6.9: Sensors installed on the tested system and in the test chamber.

The sensors listed above are usually positioned inside the chamber in the following configuration:

- 6 surface temperature sensors for the internal walls, one on each side of the test chamber;

- 6 surface temperature sensors for the external walls, one on each side of the test chamber;

- 4 air temperature probes placed on a pole in the middle of the chamber, positioned at different heights (typically 0.1, 0.7, 1.1, 2.4 m above the floor);

- 4 air temperature probes placed on a pole near to a corner of the chamber, positioned at different heights (typically the same of the previous pole);

- 4 air temperature probes outside the test chamber, one for each side of the chamber;

- 1 surface temperature probe above the test module;

- 1 surface temperature probe below the test module;

- 1 globe thermometer on the pole in the middle of the chamber (typically 1.1 m above the floor);

- 1 globe thermometer on the pole near to a corner of the chamber (typically the same of the previous one);

- 1 hygrometer, placed on one side of the room;

- 4 anemometers placed on the pole in the middle of the chamber, positioned at different heights (typically the same of the air temperature sensors)

- 1 heat flux meter above the test module;

- 1 heat flux meter below the test module;

- 1 heat flux meter on one wall of the chamber;

6.4.2 Steady state measurement of thermal output

The steady state measurement of thermal output can be performed in heating or cooling mode. In the first case, the reference is the EN 14037 standard [40], while in the second case the reference is the EN 14240 standard [39]. In both cases, the first step is choosing a water flow value, that is kept constant for the entire test. Typical water flow values are in the range from 0.4 to 4 l min^{-1}. Another value that is kept constant for the entire test is the reference temperature of the room, that is equal to 20°C for heating and 26°C for cooling testing. Different temperatures may be chosen for special applications. The water inlet temperature of the tested system is another variable: usually three different temperatures are chosen to perform a ramp. The goal is pivoting the temperature ramp around a value near to 35°C for heating and 18°C for cooling, but the exact values are chosen on the expected performance of the tested system.

The total thermal power exchanged between the tested module and the chamber is derived from the enthalpy balance of the system, as in Equation 6.21:

$$Q = m\, c_p (T_i - T_o) \tag{6.21}$$

where:

- Q is the total exchanged thermal power [W];

- m is the water mass flow rate [kg s^{-1}];

- c_p is the water specific heat [J kg^{-1} K^{-1}];

- T_i is the inlet temperature of the tested system;

- T_o is the outlet temperature of the tested system.

The mass flow rate is derived from the measured volumetric flow rate with the following Equation 6.22:

$$m = \rho f \tag{6.22}$$

where:

- ρ is the water density [kg m^{-3}];

- f is the volumetric flow rate [m^3 s^{-1}].

An alternative method to obtain the net heat flux exchanged between the tested module and the room is based on infrared thermography, as shown by the following Equation 6.23:

$$q_n = h(T_m - T_r) \tag{6.23}$$

where:

- q_n is the net heat flux exchanged between the tested system and the environment [W m^{-2}];

- h is the heat exchange coefficient [W m^{-2} K^{-1}];

- T_m is the mean temperature of the tested system [°C];

- T_r is the reference temperature of the room [°C];

Different values are proposed in the literature for the heat exchange coefficient [41–43]; in this work the values of [44] were selected.

6.4.3 Results on a geopolimeric panel

The results of the experimental procedure are presented for an innovative radiant ceiling specimen containing geopolymeric material. Geopolymers [45] are ceramic-like materials in their structures and properties that are obtained at low temperatures. The term geopolymer includes a broad range of materials that were developed in the last decades. The synthetic creation of these materials has in fact a wide flexibility in terms of components and processes, allowing a great variety of applications in the construction sector. Geopolymers may be utilized as a replacement for concrete, inside fire resistance coating, as a binder, and as a waste immobilization solution [46].

In this work a geopolymeric sample was created with a structure similar to traditional plasterboard ceiling panels, the most common layout for radiant ceiling. The hydraulic layout was created using a traditional piping system (10 mm PEX tubes) arranged in a serpentine. The tube was partially embedded inside a 50 mm thick insulating EPS layer. The geopolymer finishing layer had a maximum height of 10 mm and was assembled using three geopolymeric tiles, for an overall panel width equal to 500 mm and length equal to 1 m. The radiant ceiling prototype is depicted in the following Figure 6.15.

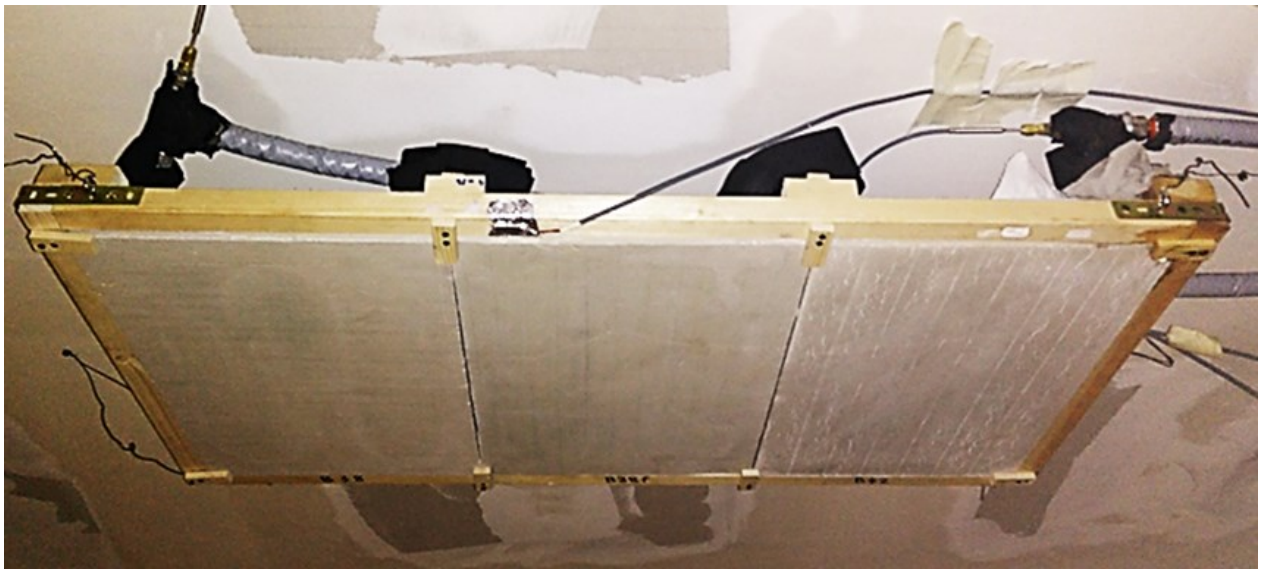

Figure 6.15: Image of the geopolimeric radiant panel installed inside the test room.

The steady state measurement of thermal output was conducted using the thermal chamber and the experimental apparatus described in the previous sections. The global thermal output of the panel, based on Equation 6.21, was equal to 44 W m^{-2} with an inlet temperature equal to 17.8 °C and a room temperature equal to 26.1 °C. During this test, the surface temperature of the panel was measured with a thermographic camera, as shown in the next Figure 6.16.

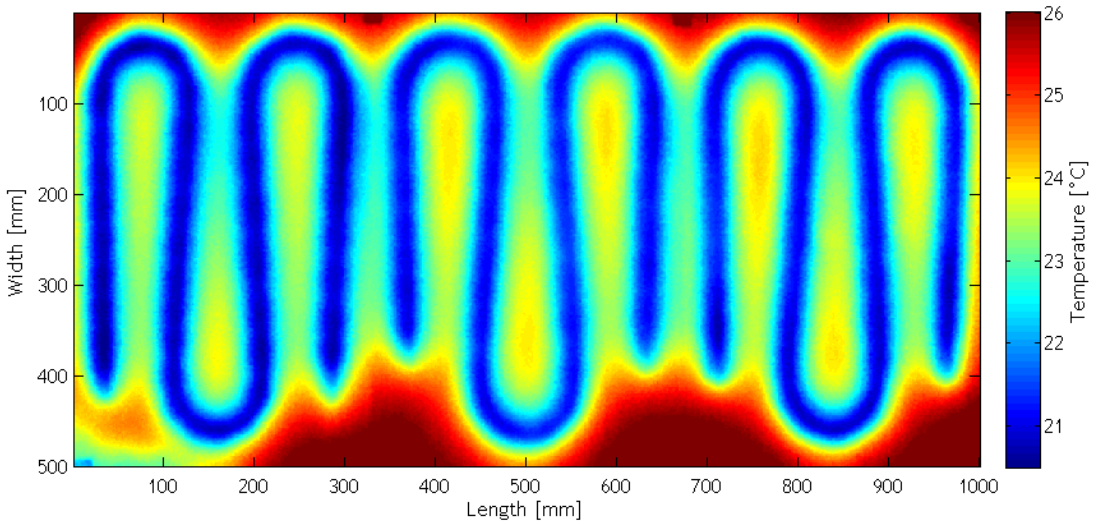

Figure 6.16: Surface temperature map of the geopolimeric radiant panel during the heating test (Inlet temperature equal to 18 °C)

This value allowed the calculation of the net thermal output of the panel through Equation 6.23. The obtained value was equal to 36 W m^{-2}, that is quite close to the value measured with the enthalpy balance if the backward losses and the non-active areas of the panel are taken into account. The thermal map is useful also to verify the quality of the panel. At a first glance it is possible to clearly identify the piping layout and a more detailed analysis reveals some areas that have a higher thermal resistance than the surrounding ones. This is highlighted by Figure 6.17, that shows a temperature profile of an horizontal line across the middle of the panel.

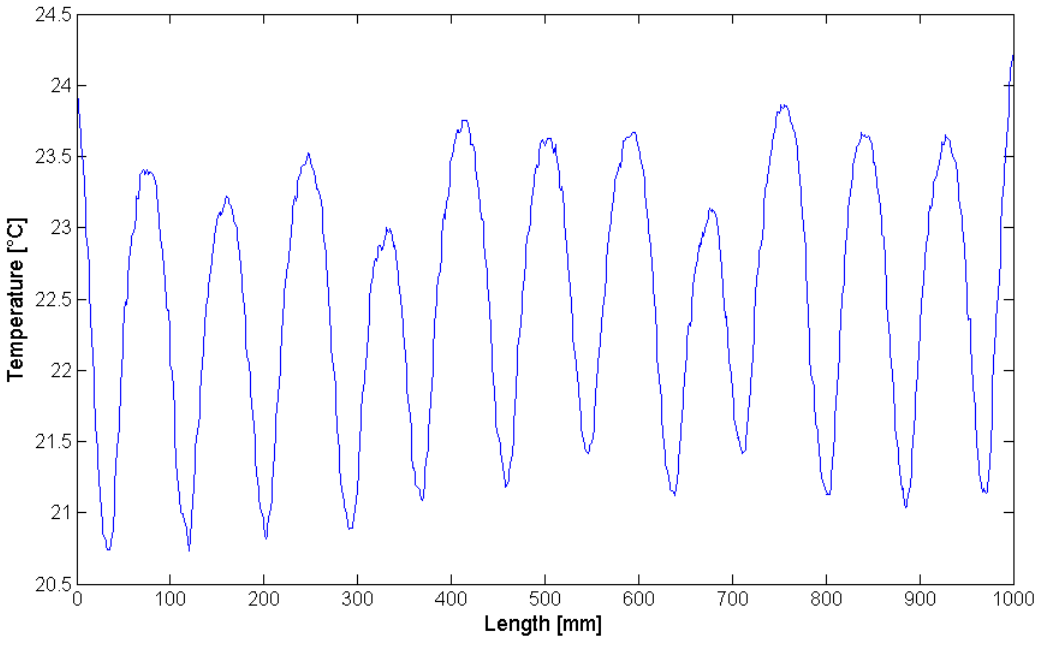

Figure 6.17: Temperature profile over the middle horizontal line (width = 250 mm) of the geopolimeric radiant panel.

As expected, the temperature trend is gradually increasing from the inlet to the outlet. However it is possible to note that the increase is not monotonic and some spots have significantly different values. This is a signal of possible issues in the manufacturing of the panel, such as a poor adhesion between the pipe and the surrounding layers or an incorrect layering of the pipes, that results in an increased thickness of the covering layer.

6.5 References

[1] G. Ferrarini, P. Bison, A. Bortolin, G. Cadelano, M. De Carli, Thermographic measurement of thermal bridges in buildings under dynamic behavior, in: Proceedings of SPIE - The International Society for Optical Engineering, Baltimore, 2016. doi:10.1117/12.2225082.

[2] A. Bortolin, G. Ferrarini, P. Bison, G. Cadelano, Thermal performance measurement of the building envelope by infrared thermography, Atti Della Fondazione Giorgio Ronchi. 69 (2014).

[3] M. Natali, A. Bortolin, G. Ferrarini, G. Cadelano, M. De Carli, S. Tamburini, P. Bison, Pannelli radianti geopolimerici, in: VIII Giornata Di Studio - Gruppo Di Lavoro Geopolimeri, Padova, 2015.

[4] G. Ferrarini, P. Bison, A. Bortolin, G. Cadelano, Thermal response measurement of building insulating materials by infrared thermography, Energy and Buildings. 133 (2016) 559–564. doi:10.1016/j.enbuild.2016.10.024.

[5] T.G. Theodosiou, A.M. Papadopoulos, The impact of thermal bridges on the energy demand of buildings with double brick wall constructions, Energy and Buildings. 40 (2008) 2083–2089. doi:10.1016/j.enbuild.2008.06.006.

[6] H. Ge, V.R. McClung, S. Zhang, Impact of balcony thermal bridges on the overall thermal performance of multi-unit residential buildings: A case study, Energy and Buildings. 60 (2013) 163–173. doi:10.1016/j.enbuild.2013.01.004.

[7] G.H. dos Santos, N. Mendes, P.C. Philippi, A building corner model for hygrothermal performance and mould growth risk analyses, International Journal of Heat and Mass Transfer. 52 (2009) 4862–4872. doi:10.1016/j.ijheatmasstransfer.2009.05.026.

[8] ISO 9869-1:2014 - Thermal insulation -- Building elements -- In-situ measurement of thermal resistance and thermal transmittance -- Part 1: Heat flow meter method, (2014).

[9] G. Ficco, F. Iannetta, E. Ianniello, F.R. d'Ambrosio Alfano, M. Dell'Isola, U-value in situ measurement for energy diagnosis of existing buildings, Energy and Buildings. 104 (2015) 108–121. doi:10.1016/j.enbuild.2015.06.071.

[10] F. Asdrubali, G. Baldinelli, F. Bianchi, A quantitative methodology to evaluate thermal bridges in buildings, Applied Energy. 97 (2012) 365–373. doi:10.1016/j.apenergy.2011.12.054.

[11] A. Bortolin, G. Cadelano, G. Ferrarini, P. Bison, F. Peron, X. Maldague, High-resolution survey of buildings by lock-in IR thermography, in: Thermosense: Thermal Infrared Applications XXXV, 2013: pp. 870503-870503–9. doi:10.1117/12.2016592.

[12] P. Bison, A. Bortolin, G. Cadelano, G. Ferrarini, E. Grinzato, Comparison of some thermographic techniques applied to thermal properties characterization of porous materials, in: Proc of 11th International Conference on Quantitative Infrared

Thermography-QIRT2012. Naples, Italy, 2012. http://www.ndt.net/article/qirt2012/papers/QIRT-2012-364.pdf (accessed May 27, 2015).
[13] E. Grinzato, G. Cadelano, P. Bison, Moisture map by IR thermography, Journal of Modern Optics. 57 (2010) 1770–1778. doi:10.1080/09500341003731597.
[14] G. Cadelano, P. Bison, A. Bortolin, G. Ferrarini, F. Peron, M. Girotto, M. Volinia, Monitoring of historical frescoes by timed infrared imaging analysis, Opto-Electronics Review. 23 (2015) 102–108.
[15] ISO 10211:2007 - Thermal bridges in building construction -- Heat flows and surface temperatures -- Detailed calculations, 2007.
[16] A. Capozzoli, A. Gorrino, V. Corrado, A building thermal bridges sensitivity analysis, Applied Energy. 107 (2013) 229–243. doi:10.1016/j.apenergy.2013.02.045.
[17] Comsol Multiphysics Version 4, 2011.
[18] E. Grinzato, Humidity and air temperature measurement by quantitative infrared thermography, Quantitative InfraRed Thermography Journal. 7 (2010) 55–72. doi:10.3166/qirt.7.55-72.
[19] E. Grinzato, P. Bison, G.. Cadelano, F. Peron, R-value estimation by local thermographic analysis, in: R.B. Dinwiddie, M. Safai (Eds.), 2010: p. 76610H. doi:10.1117/12.850729.
[20] I. Nardi, D. Paoletti, D. Ambrosini, T. De Rubeis, S. Sfarra, U-value assessment by infrared thermography: A comparison of different calculation methods in a Guarded Hot Box, Energy and Buildings. 122 (2016) 211–217. doi:10.1016/j.enbuild.2016.04.017.
[21] ISO 13786:2007, Thermal performance of building components -- Dynamic thermal characteristics -- Calculation methods, (2007).
[22] E. Kossecka, J. Kosny, Influence of insulation configuration on heating and cooling loads in a continuously used building, Energy and Buildings. 34 (2002) 321–331. doi:10.1016/S0378-7788(01)00121-9.
[23] C. Di Perna, F. Stazi, A.U. Casalena, M. D'Orazio, Influence of the internal inertia of the building envelope on summertime comfort in buildings with high internal heat loads, Energy and Buildings. 43 (2011) 200–206. doi:10.1016/j.enbuild.2010.09.007.
[24] N. Aste, A. Angelotti, M. Buzzetti, The influence of the external walls thermal inertia on the energy performance of well insulated buildings, Energy and Buildings. 41 (2009) 1181–1187. doi:10.1016/j.enbuild.2009.06.005.
[25] L.E. Fedoruk, R.J. Cole, J.B. Robinson, A. Cayuela, Learning from failure: understanding the anticipated–achieved building energy performance gap, Building Research & Information. 43 (2015) 750–763. doi:10.1080/09613218.2015.1036227.
[26] G.R. Newsham, S. Mancini, B.J. Birt, Do LEED-certified buildings save energy? Yes, but…, Energy and Buildings. 41 (2009) 897–905. doi:10.1016/j.enbuild.2009.03.014.
[27] I. Philippi, J.C. Batsale, D. Maillet, A. Degiovanni, Measurement of thermal diffusivities through processing of infrared images, Review of Scientific Instruments. 66 (1995) 182–192. doi:10.1063/1.1146432.
[28] A. Muscio, P.G. Bison, S. Marinetti, E. Grinzato, Thermal diffusivity measurement in slabs using harmonic and one-dimensional propagation of thermal waves, International Journal of Thermal Sciences. 43 (2004) 453–463. doi:10.1016/j.ijthermalsci.2003.10.005.
[29] P.G. Bison, S. Marinetti, A. Mazzoldi, E. Grinzato, C. Bressan, Cross-comparison of thermal diffusivity measurements by thermal methods, Infrared Physics & Technology. 43 (2002) 127–132. doi:10.1016/S1350-4495(02)00130-5.

[30] D.C. Hittle, R. Bishop, An improved root-finding procedure for use in calculating transient heat flow through multilayered slabs, International Journal of Heat and Mass Transfer. 26 (1983) 1685–1693. doi:10.1016/S0017-9310(83)80089-1.
[31] ISO 6946:2007, Building components and building elements -- Thermal resistance and thermal transmittance -- Calculation method, (2007).
[32] ISO 8302:1991 - Thermal insulation -- Determination of steady-state thermal resistance and related properties -- Guarded hot plate apparatus, 2013.
[33] M.J. Richardson, The Application of Differential Scanning Calorimetry to the Measurement of Specific Heat, in: K.D. Maglić, A. Cezairliyan, V.E. Peletsky (Eds.), Compendium of Thermophysical Property Measurement Methods, Springer US, 1992: pp. 519–545. doi:10.1007/978-1-4615-3286-6_18.
[34] ASNT, Technical Report c20-00. Standard test methods for apparent porosity, water absorption, apparent specifc gravity, and bulk density of burned refractory brick and shapes by boiling water., (2010).
[35] P.R. Bevington, D.K. Robinson, Data reduction and error analysis for the physical sciences, Third Edition, McGraw-Hill, New York, 2003.
[36] JCGM 100:2008, Evaluation of measurement data - Guide to the expression of uncertainty in measurement, 2008.
[37] P. Bison, G. Cadelano, E. Grinzato, Thermographic Signal Reconstruction with periodic temperature variation applied to moisture classification, Quantitative InfraRed Thermography Journal. 8 (2011) 221–238. doi:10.3166/qirt.8.221-238.
[38] R. Bean, B.W. Olesen, W.W. Kim, History of Radiant Heating & Cooling Systems, Part 1, ASHRAE Journal. (2010) 40.
[39] UNI EN 14240 Ventilation for buildings - chilled ceilings - testing and rating cooling capacity, 2005.
[40] EN 14037 Free hanging heating and cooling surfaces for water with a temperature below 120 °C, 2015.
[41] F. Causone, S.P. Corgnati, M. Filippi, B.W. Olesen, Experimental evaluation of heat transfer coefficients between radiant ceiling and room, Energy and Buildings. 41 (2009) 622–628. doi:10.1016/j.enbuild.2009.01.004.
[42] H.B. Awbi, A. Hatton, Natural convection from heated room surfaces, Energy and Buildings. 30 (1999) 233–244. doi:10.1016/S0378-7788(99)00004-3.
[43] B.W. Olesen, E. Michel, F. Bonnefoi, C. De, Heat exchange coefficient between floor surface and space by floor cooling - theory or a question of definition, in: 2000: p. PA/.
[44] UNI EN 1264 - Water based surface embedded heating and cooling systems, 2009.
[45] J. Davidovits, Geopolymers: Inorganic polymeric new materials, Journal of Thermal Analysis. 37 (1991) 1633–1656. doi:10.1007/BF01912193.
[46] B. Singh, G. Ishwarya, M. Gupta, S.K. Bhattacharyya, Geopolymer concrete: A review of some recent developments, Construction and Building Materials. 85 (2015) 78–90. doi:10.1016/j.conbuildmat.2015.03.036.

7 Building modeling: combining experimental data and simulation tools

This section, based on published works [1–3], deals with the use of building modeling tools and their integration with thermographic surveys. After a brief description of the available simulation software and of their possibilities, the San Vito alla Rivera Church is presented as a case study of interaction between thermography and numerical modeling. Then a simplified online tool for the comparison of insulating materials (ECOShopping database) is presented. The database allows to compare materials both in terms of thermal and economical performance. A further analysis on insulating materials is performed with the Life Cycle Assessment (LCA) method. Finally, the numerical simulation of radiant heating and cooling system is presented.

7.1 Integration of thermographic survey and building modeling

The term “building modeling” may encompass a wide range of software tools, dedicated to the design and investigation of the structural, energetic, acoustic, lighting characteristics of a building. Focusing on the energetic analysis, several tools are available to evaluate a building and its main components. The general term Building Information Modeling (BIM) [4] refers to software designed to follow all the phases of the building construction and aiming to embed in a single framework all the information about geometry, costs, materials, and scheduling of a building. This kind of general purpose software hosts all the information needed to create or integrate an energy model of the building. More specific software are instead dedicated to Building Energy Modeling (BEM) [5], where the aim is the quantification of the energy performance of the building, typically on a yearly basis. Other tools, that are either a support to BEM or to different standalone software, are databases. The most used databases in this sector contain information on building materials and components, and could be exploited by simulation engines that allow LCA analysis or energetic comparisons. Their typical application is during the design and optimization of a retrofit intervention. Another important branch of software is dedicated to the numerical solution of thermal and computational fluid dynamics (CFD) problems. These tools may be fundamental for the prediction of microclimate conditions and are frequently coupled with energy models to assess the performance of conditioning systems or to verify critical details of the

buildings. CFD software is frequently used also to design HVAC systems to optimize the expected performance of the systems. The following Table 7.1 summarizes the main application fields of the tools described above. It should be noted that in the future the distinction between different software will become even more difficult, as the current trend is creating wide purpose software that encapsulates all the available specific tools.

Aim	Activities	Software
Energy consumption	Simulation and analysis of the annual performance of the building envelope and of the HVAC system	BEM BIM
Retrofit optimization	Choice between different materials and components for energy saving measures	Database BEM BIM
Microclimate for comfort and conservation	Simulation and analysis of environmental parameters inside the building.	CFD BEM
HVAC system design	Simulation and analysis of the performance of HVAC system	CFD

Table 7.1: Overview of different software used for building modeling.

The simulation tools mentioned above are more and more a cornerstone of the building design process, as the design phase is nowadays recognized as critical. Unfortunately, a great part of the potential benefit deriving from the application of these tools is wasted if they are applied as standalone objects and are not integrated within the building survey. The simulation software should always be connected to the real data coming from building survey, for two basic and complementary reasons: the need to validate the simulations on-site and to feed the models with real data [6]. The latter issue is frequently underestimated, as the attention is typically focused on the quality of the model itself, neglecting the fact that any model would give unreliable results when fed with inaccurate data.

7.2 A case study: the S. Vito alla Rivera Church

The San Vito alla Rivera Church, that dates back to the XII century, is located in L'Aquila. The church has been damaged by the 2009 earthquake, especially in the facade and in the roof. After the first structural reinforcement measures, it has been possible to perform two surveys, one in winter and another in spring, as shown also in Chapter 5. This measurement campaigns have been included in a renovation procedure, that is typically formed by various steps. The procedure starts with the preliminary definition of the energy saving criteria applicable to the particular case, in terms of reducing the volume and time when the indoor conditioning is required.

The second step is the energy survey, that can be focused on the whole building or on its single components. The latter consists in a characterization of thermo-physical properties of samples of construction materials while the former has been the evaluation of the conditions of the building with techniques based on infrared thermography. The following step of the procedure is the analysis of the acquired data and their integration with thermal and fluid dynamics simulation software in order to predict the energy consumption and the comfort conditions. The integrated use of the findings and mathematical simulations allows the expansion of the conditions usually found in two typical seasons (e.g. winter or summer) to any other condition or seasonal use and consider various options of thermal loads and occupational schedule.

Of fundamental importance is the use of real data as partial input of the models as it permits to fine-tune the calculation parameters, improving the reliability of the simulation results. The successive stage is the implementation of the selected energy saving actions, that could range from simple changes to the behavior of the occupants to the complete restoration of the building. The last part of the procedure is the monitoring of the energy consumption and the experimental verification of the comfort conditions produced by the intervention, with the main objectives to optimize its operation, to verify the correctness of the implementation and possibly identify sources of errors in any of the previous stages.

The building simulation is therefore a crucial segment of the renovation procedure. An energy model of the church was built after the on-site surveys and used both to evaluate the thermal behavior of the building and to investigate an energy saving measure for the roof (as shown in Section 7.3). Two energy model are created, with the software TRNSYS and EnergyPlus - Design Builder. In the study, different environmental conditions and

occupants behaviors have been simulated in order to provide the thermal loads for the building in both summer and winter conditions.

The first simulations have been conducted without a heating system, in order to create a baseline for the comparison with experimental data.

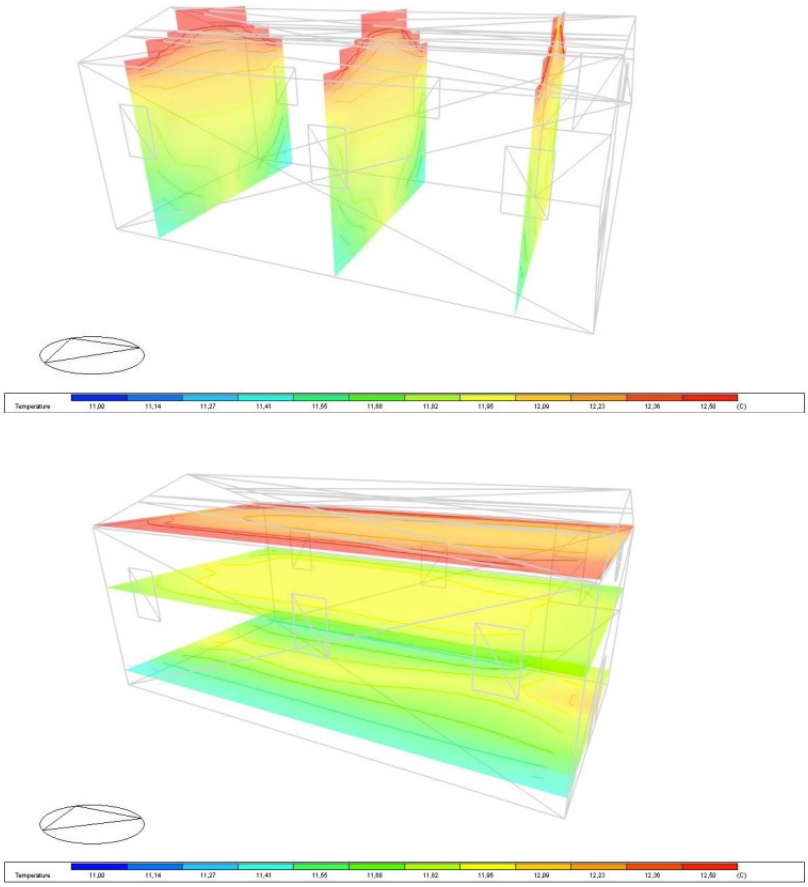

Figure 7.1: Calculation of air temperature distribution [°C] on three vertical (upper image) and horizontal (lower image) sections inside the building, in passive conditions, obtained with the Design Builder software, with boundary conditions based on experimental measurements.

The simulated temperature for the baseline case (Figure 7.1) have been compared with the experimental data coming from the infrared survey performed with the aIRview equipment described in Chapter 5, showing good agreement. The aIRview system is capable to measure also other physical quantities that are relevant to the indoor environment, such as air velocity. Figure 7.2 shows the air velocity distribution on vertical and horizontal sections, that are checked against the experimental measurement that show very low values. This baseline simulations, validated against on-site measurement, are helpful to assess the quality of yearly simulation that are the only tool able to estimate the energy performance of the building and the best intervention strategies.

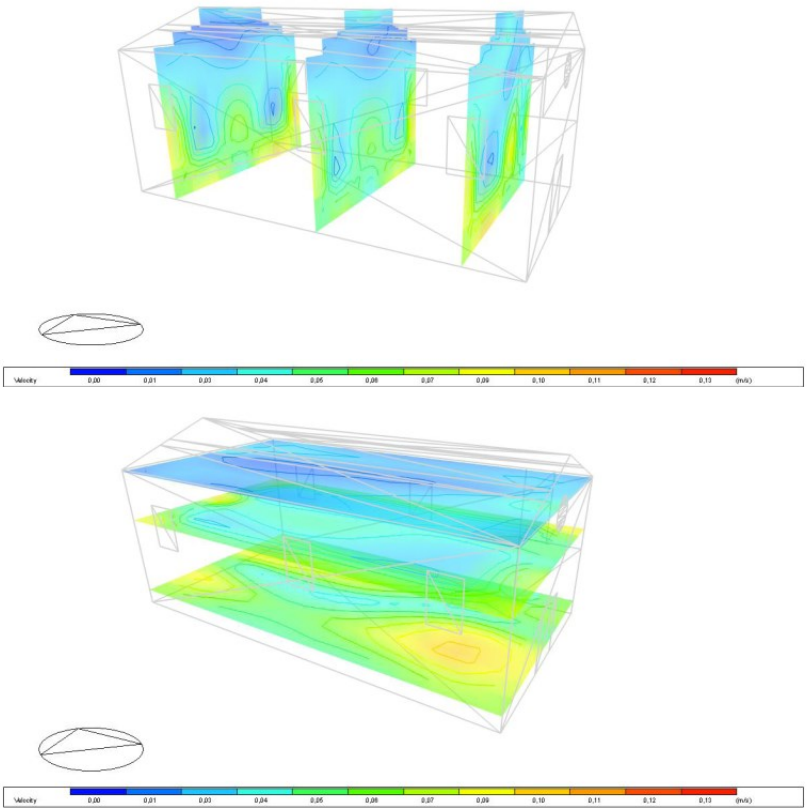

Figure 7.2: Calculation of air velocity distribution [m s^{-1}] on three vertical (upper image) and horizontal (lower image) sections inside the building, in passive conditions, obtained with the Design Builder software, with boundary conditions based on experimental measurements.

7.3 Optimal choice of insulating materials: the Life Cycle Analysis

The design phase of a building retrofit could be focused only on the energetic analysis or could follow a more holistic approach. The following study chooses the latter strategy, with the goal of underlining the limits and possibilities of the application of Life Cycle Analysis (LCA) during the modeling and evaluation of energy savings phases. This method has been applied more and more frequently as a planning tool for new buildings, however it is not commonly chosen for building retrofit and in particular for the renovation of historical buildings. In Italy the LCA method is not mandatory, therefore it has been applied only in few cases (e.g. planning competitions) and only under direct request of the customer [14,15]. The stock of Italian historical and listed buildings that needs retrofit interventions would benefit from the application of LCA, as it would lead to the use of materials with a lower environmental impact. The main barriers to the diffusion of LCA for historical building retrofit are the lack of a standardized approach and the difficulty of obtaining accurate data about the manufacturing processes and the material properties of construction elements.

The LCA method [16] was applied in two successive steps with different goals. Initially, three different insulating materials were compared to determine the one with the lowest impact for an intervention on a roof. A multiple search conducted on the ECOshopping database of insulation materials and on the EcoInvent 2.2 database [17,18] led to group all the materials in three different categories. For each category one material was chosen on the basis of an estimated on-site availability. The first group was made by traditional material with very good thermal properties and low cost, and the selected material was extruded polystyrene (XPS). The second group was made by natural materials with good thermal properties and high cost, and the selected material was cork. The last group was made by intermediate thermal properties and cost, and the selected material was wood wool. The material properties are described in the next Table 7.2, including the quantity needed to reach the target thermal transmittance of the renovated wall equal to 0.3 W m^{-2} K^{-1}.

Material	Thickness [cm]	Volumic mass [kg m^{-3}]	Thermal conductivity [W m^{-1} K^{-1}]	Quantity [kg m^{-2}]
Cork	11.6	120	0.039	13.9
XPS	10.4	35	0.034	3.6
Wood wool	26.9	400	0.090	107.6

Table 7.2: Properties of the three insulation materials compared in the LCA properties. The quantity is the amount of material required to reach the target thermal transmittance of the wall.

The software used for the LCA calculation was SimaPro 7.3 [19]. The study considered the impact due to transportation from the manufacturer to the building site and also the impact of the end-of-life disposal of the materials. The available solutions for the end-of-life are various, including recycling; this work considered the material will be incinerated after use.

The LCA study could be conducted with different methodologies. The results shown in the next figures 2-5 were respectively obtained with five methods: IMPACT 2002+ v2.11, EDIP 2003 v1.04, EPS 2000 v2.07, Re.Ci.Pe. Endpoint (E) v1.09 / Europe ReCiPe E/A, and IPCC 2007 GWP 100a v1.02 [19,20,21]. All methods have different impact categories and different weighting factors. The obtained results are represented from Figure 7.3 to Figure 7.7 as environmental damage indexes.

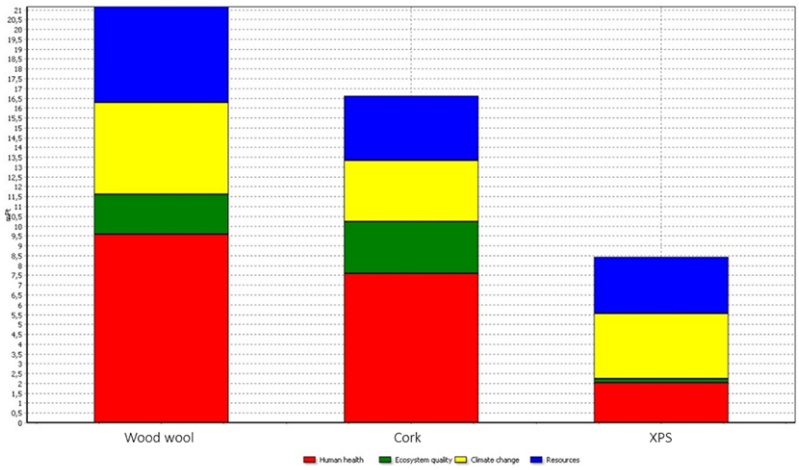

Figure 7.3: Comparison based on IMPACT 2002+ method.

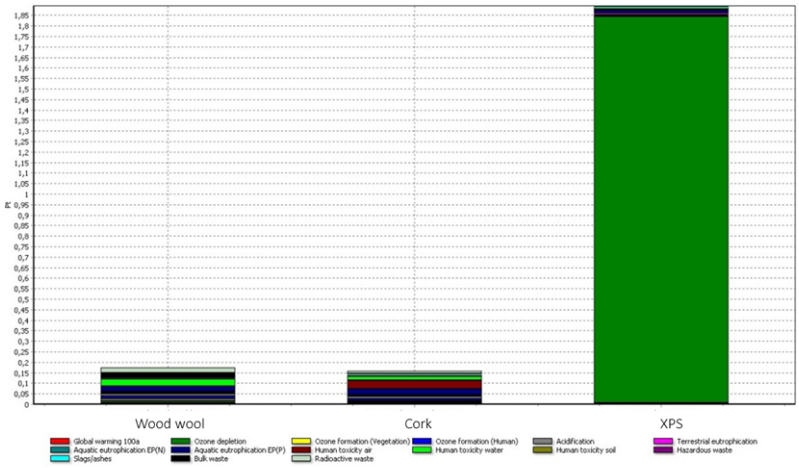

Figure 7.4: Comparison based on EDIP 2003 method

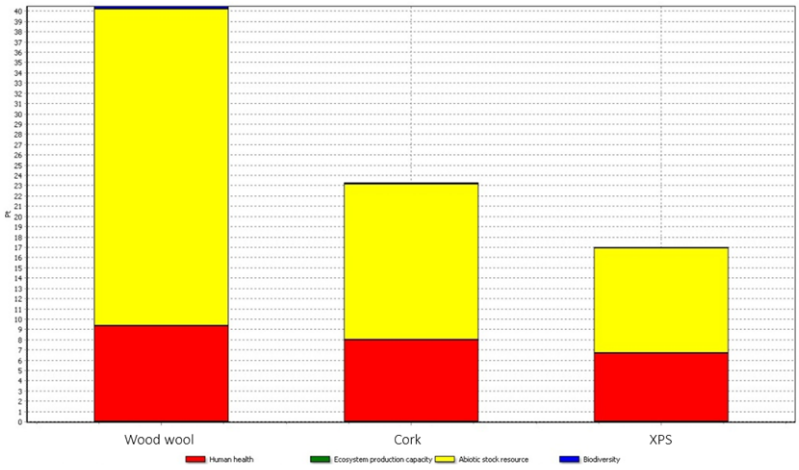

Figure 7.5: Comparison based on EPS 2000 method.

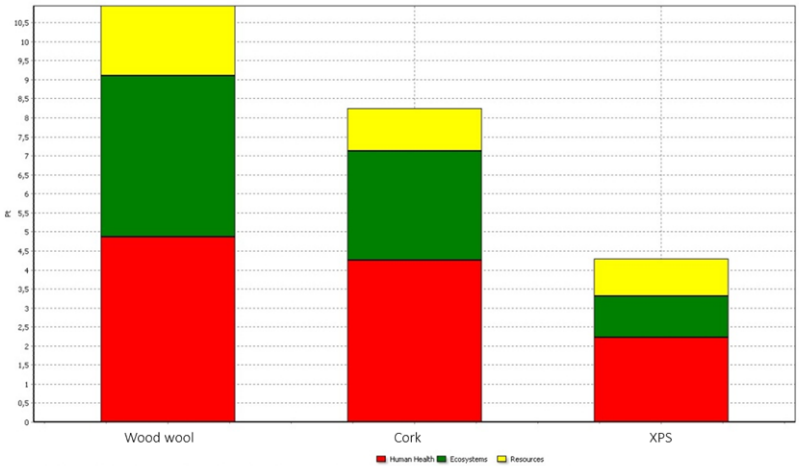

Figure 7.6: Comparison based on Re.Ci.Pe method.

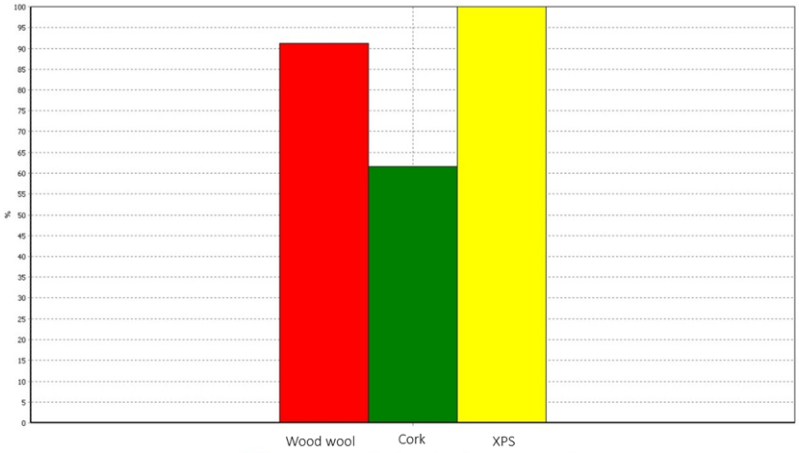

Figure 7.7: Comparison based on IPCC method.

The comparison between materials is not straightforward, as different methods give different results. Moreover the evaluation should rely only on relative comparison between materials analyzed with the same methods, as the absolute values cannot be compared between different methods.

The best material for the majority of methods was Extruded Polystyrene (on the third column) while EDIP 2003 and IPCC gave different indications. For the EDIP method, the high impact is due to the category “Ozone depletion” that represents the 96.8% of the total impact. This is caused by the use of CFC-113, a foaming agent with a very high atmospheric lifetime, during the production process. Also for the IPCC method the greatest part (81.7%) of the environmental damage is due to the presence of foaming agents, in this case HFC-134a, and to Carbon dioxide. After the choice of XPS as the insulating material for the roof, several parametric simulations were made in TRNSYS software. The thickness of the insulating layer was changed from 0 to 35 cm with a step of 5 cm. The obtained annual energy consumptions were integrated with further LCA

analysis, in order to determine if there was an optimum thickness with respect to energy consumption and material impact. The results obtained with five different LCA methods are shown in figures from Figure 7.8 to Figure 7.12.

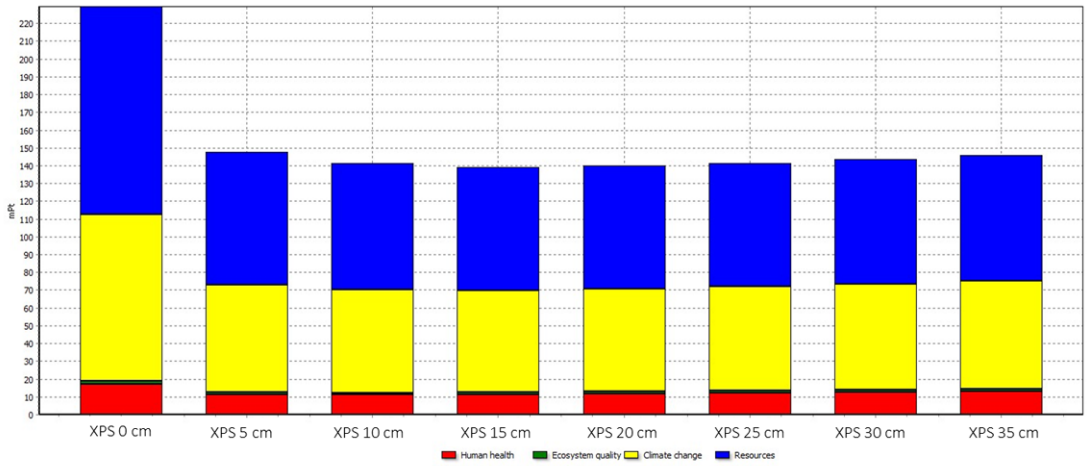

Figure 7.8: Comparison of different insulation thicknesses with the IMPACT 2002+ method

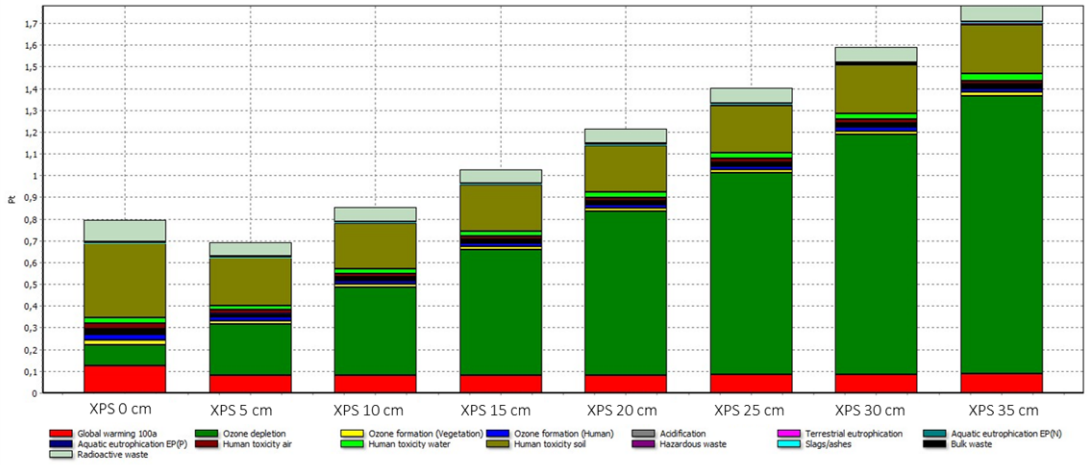

Figure 7.9: Comparison of different insulation thicknesses with the EDIP 2003 method

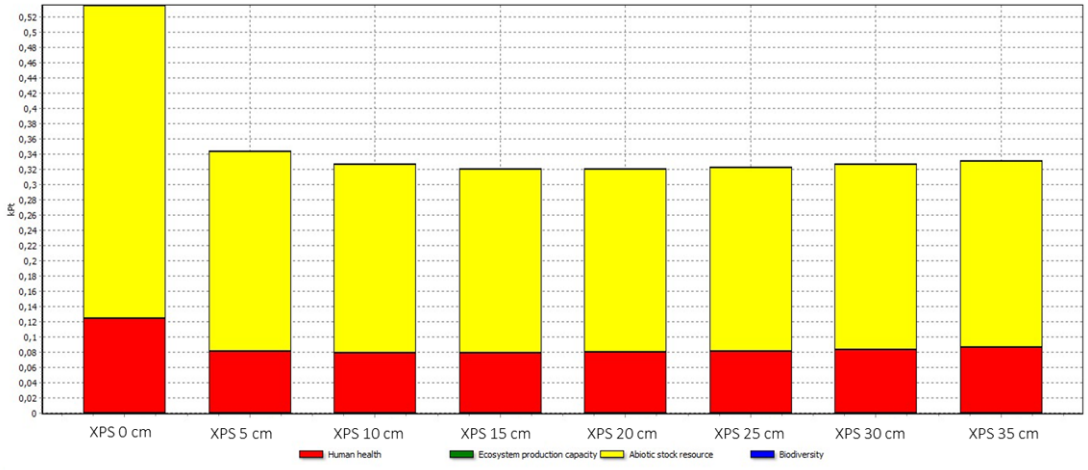

Figure 7.10: Comparison of different insulation thicknesses with the EPS 2000 method

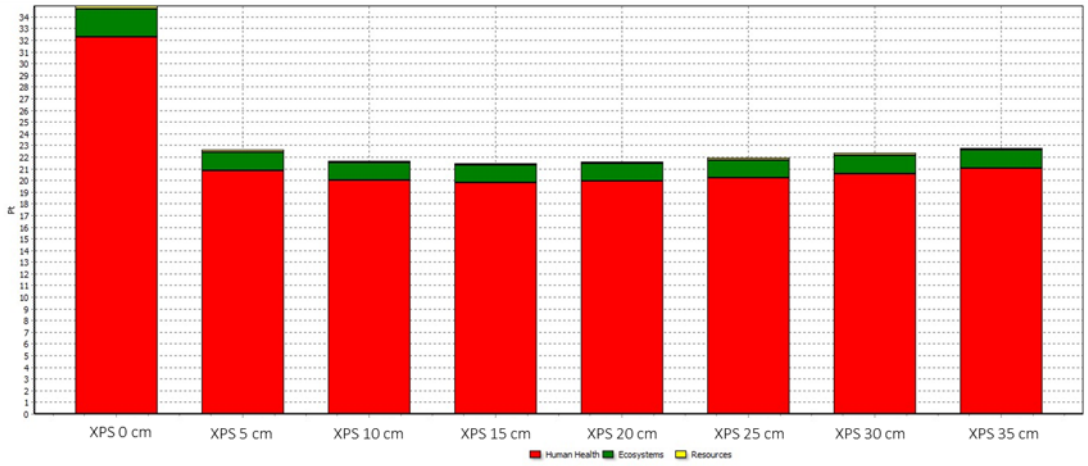

Figure 7.11: Comparison of different insulation thicknesses with the Re.Ci.Pe. method

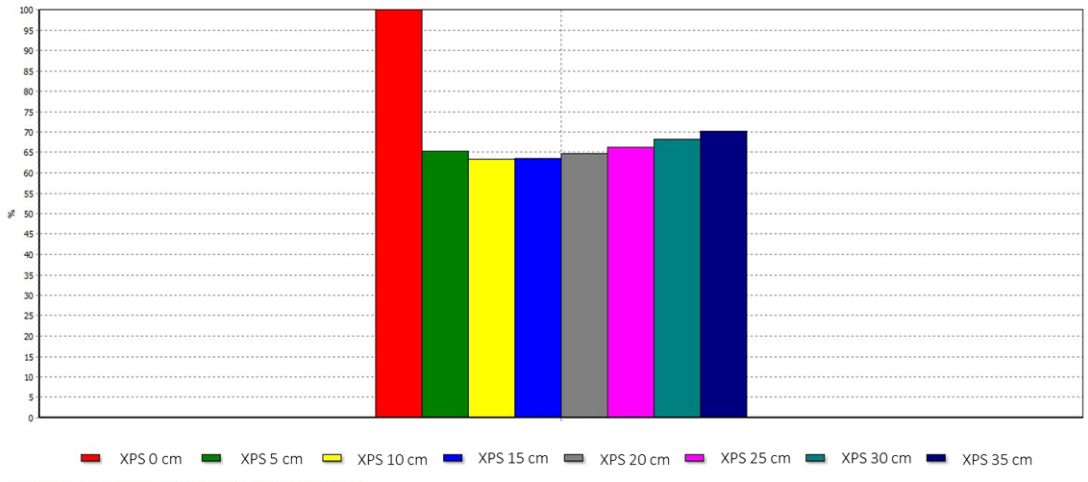

Figure 7.12: Comparison of different insulation thicknesses with the IPCC method

The effect of insulation is always positive, as even the thinner insulation is always better than the case without insulation, but an excess of insulation could be detrimental. Each method shows that the reduction of energy consumption, obtained increasing the insulation thickness, is counterbalanced by the increase of the environmental impact. Therefore an optimum thickness value could be identified and it is generally located between 5 and 15 cm, a range that contains the value of 10.4 cm that is suggested by the energy savings standards. This result is shown in Figure 7.13, where the parametric results for all the methods are reported.

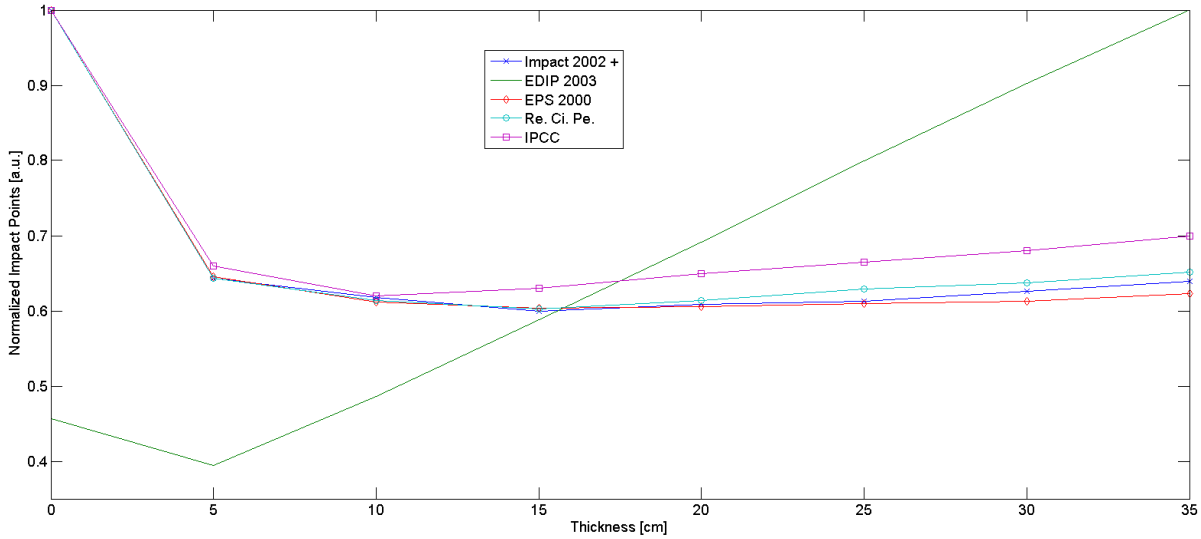

Figure 7.13: The comparison of different insulation thicknesses with all methods allows to identify the optimum thickness value.

7.4 Optimal choice of insulating materials: the ECOShopping database

Insulating materials are a key part of building analysis, as they are frequently the most effective way to improve the energy performance of a building. For this reason hundredths of commercial products are proposed by manufacturers on the market, with broadly different specifications and prices. One of the main difficulties amongst designers is the comparison between different solutions to find the best one for each specific building project. Technical specifications of insulating materials are presented by each manufacturer in a different fashion that makes practically impossible to directly compare multiple materials.

In the framework of the EU FP7th ECOShopping Project [7] a wide study was conducted on the current market of insulating material. The aim was to create a database of the insulation materials currently available in the market, based on the data declared by the manufacturers or on literary data, in order to evaluate the best solutions from an energetic and economic standpoint. The main categories of insulation properties required to make a valid comparison are shown in Figure 7.14, with an example record.

Categories	Fields	Example value	Field description
Product identification	Material	Wood fiber	Main component
	Manufacturer	Fiber Inc.	Name of the manufacturer
	Product name	Ultra Fiber Plus	Commercial name of the product
	Type	Panels	Format of the material: Flocks, Rolls, Panels or Sheets
	Inside	1	The value is 1 when the product could be applied for internal insulation, 0 if not
	Outside	1	The value is 1 when the product could be applied for external insulation, 0 if not
	Roof	1	The value is 1 when the product could be applied for roof or ceiling insulation, 0 if not
	Floor	1	The value is 1 when the product could be applied for floor insulation, 0 if not
	Wall	1	The value is 1 when the product could be applied for wall, facades or vertical surfaces insulation, 0 if not
	Link	www.insulation.com	Link to the product website or to the technical documentation
	Thickness [mm]	20	Measured in [mm]
Thermophysical properties	Thermal Conductivity [W m^{-1} K^{-1}]	0.035	Measured in [W m^{-1} K^{-1}]
	Density [Kg m^{-3}]	100	Measured in [Kg m^{-3}]
	Specific Heat [J $Kg^{-1}K^{-1}$]	1000	Measured in [J Kg^{-1} K^{-1}]
	Water vapour resistance	50	Dimensionless
	Fire Resistance Class	A	Class according to EN 13501-1:2009
Economic properties	Price [Euro m^{-2}]	10.05	Measured in [Euro m^{-2}]
Other properties	Environmental information		LCA value or Embodied Energy
	Certifications		Product certifications, if available
	Notes		Additional information on the product

Figure 7.14: Properties of a record of the walls/roof insulation database, taken from [3]

The data on insulation materials can be collected through a dedicated website, that is running at http://esdatabase.altervista.org/. On this website every user can create an account, with different privileges, that allows him to complete a form with the required

parameters for a material and create a new record in the database. A new record is hidden until an administrator verifies it and makes it public. It is possible to create custom queries to the database, for example to show all records, as in the page:

http://esdatabase.altervista.org/page_qshowall.php (Figure 7.15).

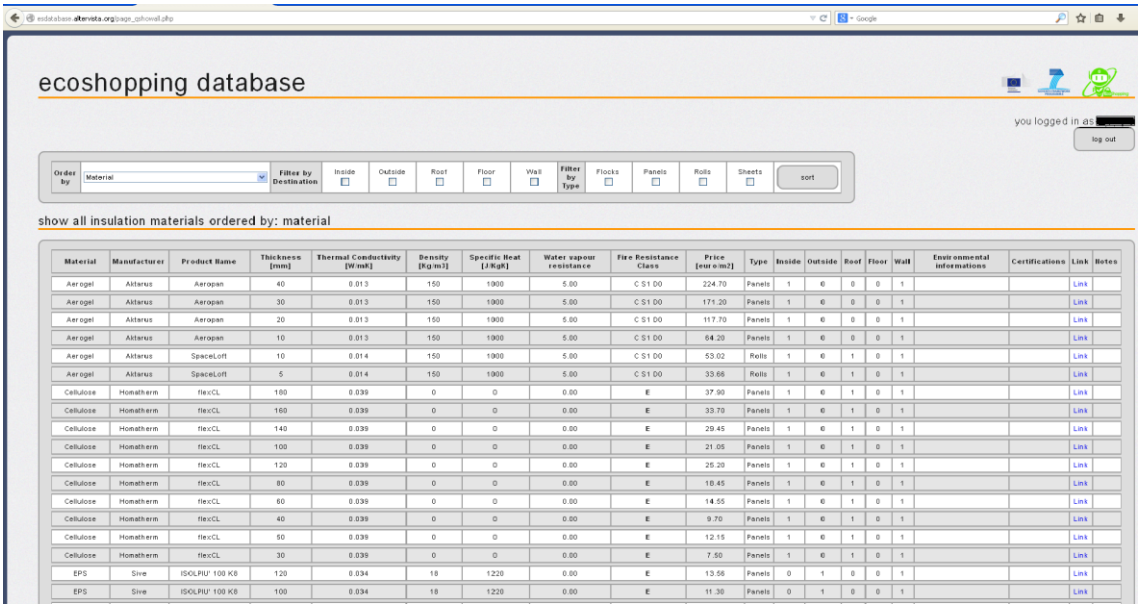

Figure 7.15: Screenshot of the database of insulating materials for walls/roofs.

A more advanced query consists in finding the least expensive material after choosing a thermal resistance value of the insulation layer. In this case the software calculates the minimum thickness required for every record in the database and then orders the products from the least to the most expensive as shown in Figure 7.16 and at the following link: http://esdatabase.altervista.org/page_qresistanceprice.php.

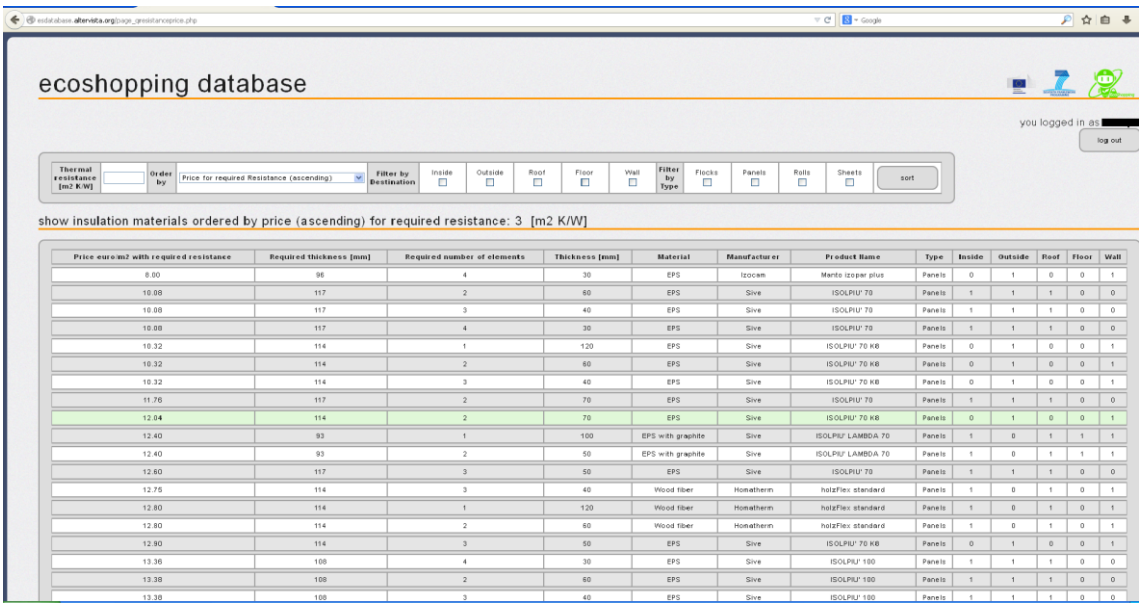

Figure 7.16: Screenshot of the database with the required thermal resistance query.

The choice of an insulation material can be made considering different parameters such as:

- Thermal resistance (or conductivity);

- Cost;

- Thickness.

A higher thermal resistance can reduce the energy demand of the building, that is usually prescribed by standards. As construction have also strict budget limitations, the cost is a fundamental parameter. A reduced wall thickness may increase the value in the real estate, overcome legal or practical restrictions in the retrofitting of existing buildings, allow a reduction of transport costs.

Exploiting the insulation database, some insulation materials have been selected fixing a thermal resistance value. Table 7.3 contains the insulation materials that guarantee the lowest cost while Table 7.4 the ones that guarantee the lowest thickness for a thermal resistance value equal to 3 $m^2 K W^{-1}$. This value has been chosen as it represents a realistic target value for a refurbishment.

Material	Thermal Conductivity [W / m K]	Minimum Thickness [mm]	Cost [Euro/m^2]
EPS	0.038	114	10.32
Wood fiber	0.038	114	12.80
Rock Wool	0.035	105	17.38

Table 7.3: Insulation material with the lowest cost for a thermal resistance value equal to 3 $m^2 K W^{-1}$.

Material	Thermal Conductivity [W / m K]	Minimum Thickness [mm]	Cost [Euro/m^2]
Aerogel	0.013	39	224.70
Thermoset	0.020	60	21.70
Expanded Polyurethane	0.023	69	28.37

Table 7.4: Insulation material with the lowest thickness for a thermal resistance value equal to 3 $m^2 K W^{-1}$.

Figure 7.17 combines the previous data in a diagram where the x axis represents the insulation thickness and the y axis the cost of the material.

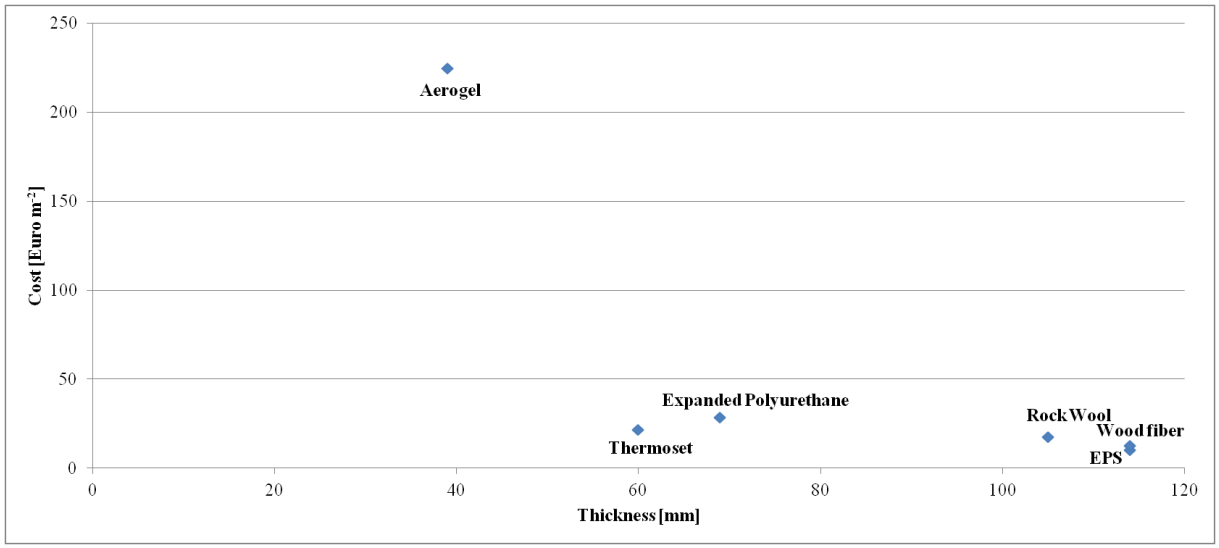

Figure 7.17: Cost versus thickness for insulation materials with a thermal resistance value equal to 3 m^2 K W^{-1}.

At the current stage of the database, the three materials that could be selected are the cheapest one, the thinnest one and a compromise between the two parameters. Expanded Polystyrene (EPS), Aerogel and Thermoset are the materials that respectively fulfill these targets.

7.4.1 Optimum thickness

A new sorting approach of the insulating materials is provided by the ”optimum thickness” query. Unlike the previous method, based on the assessment of the required value of thermal resistance, this query identifies and ranks the solutions that best optimize the cost of installation and power management with the economic benefits of a better insulation of the building envelope in terms of energy saving (and money as a consequence) [8–10]. The heat losses q per unit area of the building envelope are:

$$q = \frac{\Delta T}{R} \tag{7.1}$$

where:

- ΔT is the difference between the comfort temperature Tc and the ambient temperature Ta [K];

- R is the overall thermal resistance of the wall [m^2 K W^{-1}].

To obtain ΔT over a one-year period, the Degree-day (dd) method is used [11]; dd values can be found in literature for every geographic region [12]. R is given by the sum of the thermal resistance of the building before the retrofit (R_0) and the thermal resistance of the installed insulation layer (R_i). R_i is obtained as the ratio between the thickness l of the insulation layer and its thermal conductivity λ, both available in the database.

The total cost (C_{tot}) per unit area of the envelope insulation consists of two cost parameters, one is the energy cost (C_e) and the other is the insulation material cost (C_m). The energy cost is given as the product of the heat loss q, which depends on the overall thermal resistance of the building envelope, and the price of energy (P_e):

$$C_e = q \cdot P_e = \frac{\Delta T}{R_0 + {}^{l}/_{\lambda}} \cdot P_e \tag{7.2}$$

In this implementation the effects of inflation on P_e and the heat source efficiency over time are neglected. P_e for household or industrial profiles are available for European Union member states [13]. On its turn, the insulation material cost is given by:

$$C_m = C_i + C \cdot l \tag{7.3}$$

where

- C_i is the baseline cost (e.g. installation cost) [Euro];
- C is the unitary cost of the insulation material [Euro m^{-1}];
- l is thickness of the installed material (the variable to be optimized) [m].

The heat loss through the building envelope decreases as the insulation thickness increases with obvious future energy saving (and money as well). This at the expense of an initial higher cost to install the insulation material. Therefore, the energy saving analysis should be performed estimating the optimum insulation thickness which minimizes the total cost including the insulation material and the costs of future energy consumption:

$$C_{tot}(l) = C_e + C_m \tag{7.4}$$

The optimum thickness value is calculated by setting the derivative of C_{tot} with respect to l equal to zero, as shown in Figure 7.18.

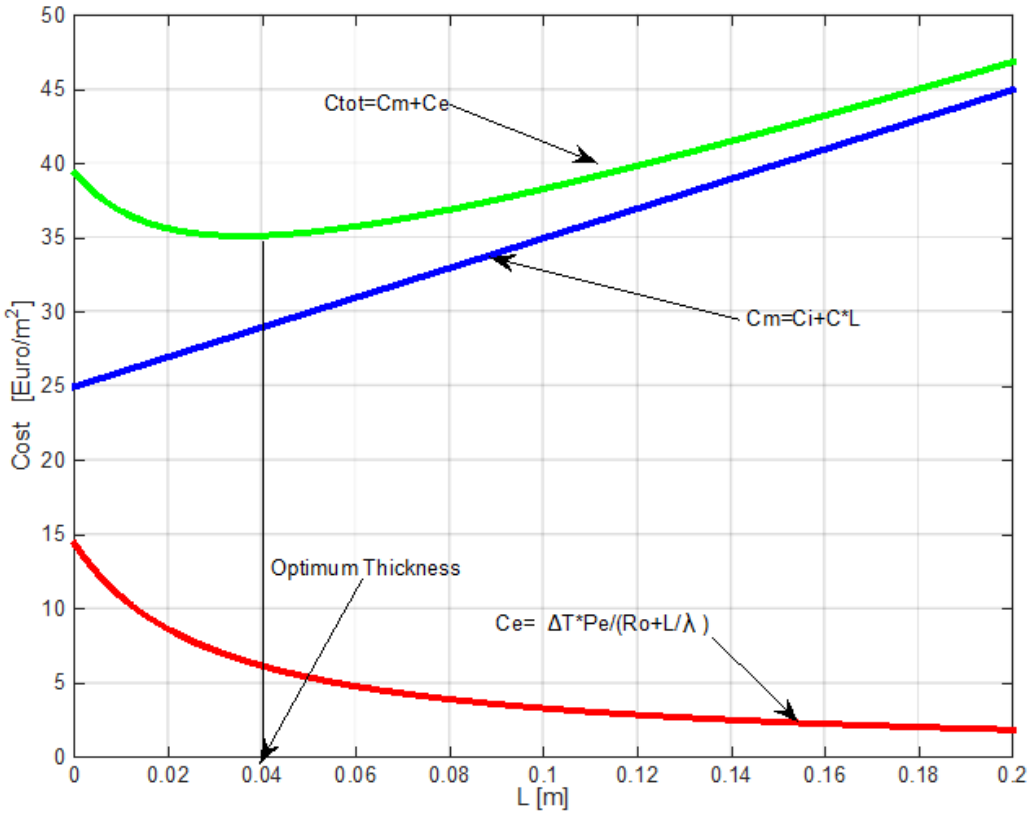

Figure 7.18: Example of computation of the optimum thickness.

The SQL query that allows this operation requires some information from the user which must be entered through the appropriate interface shown in Figure 7.19:

- P_e energy cost [€ kWh^{-1}];

- *dd* degree day [K s];

- C_i installation cost [€ m^{-2}];

- R_0 thermal resistance of the building before retrofit [m^2 K W^{-1}].

Figure 7.19: User interface for entering input data to the query OPTIMUM THICKNESS.

The obtained results can then be ranked according to:

- Optimum thickness of the insulation package (in ascending or descending order);

- Price per square meter for the insulation solution proposal (in ascending or descending order);

- Material;

- Manufacturer;

- Number of elements (i.e. panels, rolls, etc.) to be installed in order to achieve the optimum thickness.

The returned results of the query can be also filtered to show only certain categories of products, for example for of usage:

- Indoor;

- Outdoor;

- Roof;

- Floor;

- Wall.

Another feature available for this query is that it is possible to view the results not only in table form, but also as a graph of the different materials or products whose ordinate is the price per square meter for the insulation solution proposal and abscissa is the optimum thickness of the insulation package.

7.5 Simulation of the thermal performance of radiant heating and cooling systems

The use of CFD software to design HVAC systems and analyze their thermal performance is nowadays a common practice. This section is focused on radiant heating and cooling systems, described in the previous chapters. A correct design of a radiant system layout inside a building is based on the knowledge of the thermal performance of its basic elements. Several standard and guides are available to predict the thermal output of a radiant system starting from its main characteristics: materials, geometry, stratigraphy. ISO 11855 standard [20] offers 7 different categories that encompass a wide range of possible radiant systems (e.g. pipes embedded inside/outside the screed, capillary mats, Thermo Active Building Systems) offering a more or less simplified calculation method.

However, the proposed calculation methods are valid only under strict preliminary assumptions, that limit the range of input values: in several case innovative radiant systems do not comply with this limitations. In other cases new radiant systems do not

fall into any of the aforementioned categories, and also in this event the use of the simplified models is impossible.

For these reasons, the standard gives the possibility to use Finite Element Method or Finite Different Method software to calculate the steady state performance. The fundamental requisite is that the software should be verified against a reference test case proposed by standard. The test case is a floor cooling system, and the prescribed boundary conditions are:

- Room temperature below and above the structure equal to 26°C

- Water temperature equal to 18°C

- Thermal resistance at upper boundary air layer equal to 0,1429 m^2 K W^{-1}

- Thermal resistance at upper boundary air layer equal to 0,1429 m^2 K W^{-1}

In this work, several software were successfully validated against the reference test case proposed by the 11855 standard, as shown in Table 7.3.

Software	Validated against ISO 11855 standard	Transient calculation	3D calculation	Use and License
FEMM [21]	YES	NO	NO	Free, AFPL
Elmer [22]	YES	YES	YES	Free, GPL
Comsol Multiphysics [23]	YES	YES	YES	Commercial, Proprietary

Table 7.5: Comparison of Finite Element Software available for the simulation of radiant systems.

Amongst them, the Comsol software was selected to investigate the thermal performance of an innovative ceiling system with a geopolymeric layer. The system is compared with a traditional ceiling solution, with the pipe embedded inside a plasterboard layer, as shown in Figure 7.20.

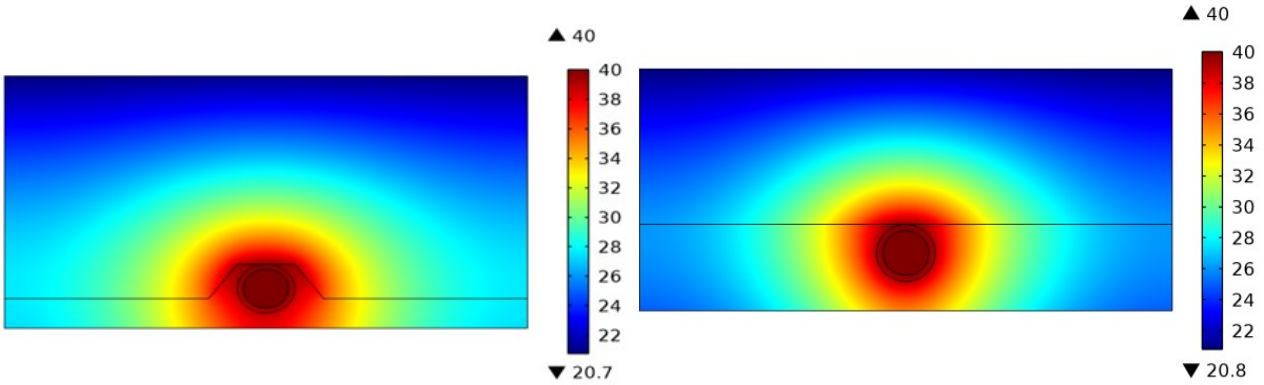

Figure 7.20: Comparison of Geopolymer system (left) and traditional system (right) temperature distribution [°C] over a 2D section in steady-state heating mode.

The comparison is conducted in steady-state conditions, both in heating and cooling mode (Figure 7.21). In heating mode, with a water temperature equal to 40°C and an environment temperature equal to 20°C, the heat flux of the geopolymeric system is equal to 71 W $m^{-2}K^{-1}$ while the innovative reaches 56.6 W $m^{-2}K^{-1}$. In cooling mode, with a water temperature equal to 16°C and an environment temperature equal to 26°C, the heat flux of the geopolymeric system is equal to 50.7 W $m^{-2}K^{-1}$ while the innovative reaches 36.6 W $m^{-2}K^{-1}$.

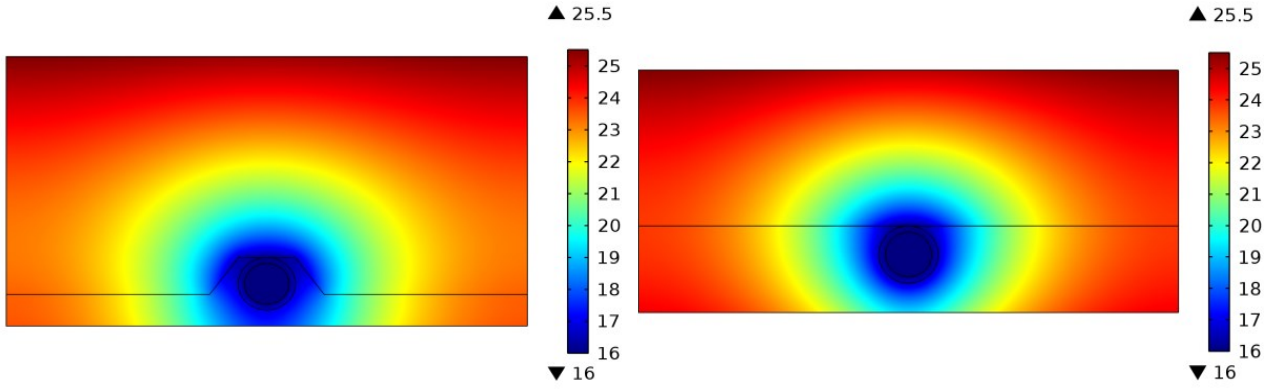

Figure 7.21: Comparison of Geopolymer system (left) and traditional system (right) temperature distribution [°C] 2D section in steady-state cooling mode.

The use of thermal simulations offers a quick and reliable way to predict the thermal outcome, that could be verified with the methods described in the previous Chapter 6.

7.6 References

[1] A. Bortolin, P. Bison, G. Cadelano, G. Ferrarini, S. Fortuna, Measurement of thermophysical properties coupled with LCA assessment for the optimization of a historical building retrofit, J. Phys.: Conf. Ser. 655 (2015) 012011. doi:10.1088/1742-6596/655/1/012011.

[2] G. Ferrarini, P. Bison, A. Bortolin, G. Cadelano, M. Girotto, U. Mazzali, F. Peron, M. Volinia, Energy survey of a historical building by infrared thermography, Atti Della Fondazione Giorgio Ronchi. 69 (2014).

[3] A. Bernardi, F. Becherini, A. Vivarelli, P. Bison, A. Bortolin, G. Cadelano, G. Ferrarini, M. Favaro, A. Galenda, M. Garrido, E. Lezak, ECOShopping Project - Deliverable 3.1 - Specification of selected types of insulation solutions based on the created database of the different conventional and most innovative insulation technologies and self-cleaning materials, (2014).

[4] C.M. Eastman, C. Eastman, P. Teicholz, R. Sacks, K. Liston, BIM Handbook: A Guide to Building Information Modeling for Owners, Managers, Designers, Engineers and Contractors, John Wiley & Sons, 2011.

[5] X. Li, J. Wen, Review of building energy modeling for control and operation, Renewable and Sustainable Energy Reviews. 37 (2014) 517–537. doi:10.1016/j.rser.2014.05.056.

[6] E. Fabrizio, V. Monetti, Methodologies and Advancements in the Calibration of Building Energy Models, Energies. 8 (2015) 2548–2574. doi:10.3390/en8042548.

[7] Ecoshopping, European FP7th Project., (2016). http://ecoshopping-project.eu/ (accessed May 5, 2016).

[8] J. Yu, C. Yang, L. Tian, D. Liao, A study on optimum insulation thicknesses of external walls in hot summer and cold winter zone of China, Applied Energy. 86 (2009) 2520–2529. doi:10.1016/j.apenergy.2009.03.010.

[9] O. Kaynakli, A review of the economical and optimum thermal insulation thickness for building applications, Renewable and Sustainable Energy Reviews. 16 (2012) 415–425. doi:10.1016/j.rser.2011.08.006.

[10] A. Hasan, Optimizing insulation thickness for buildings using life cycle cost, Applied Energy. 63 (1999) 115–124. doi:10.1016/S0306-2619(99)00023-9.

[11] Eurostat, Energy statistics - heating degree days (nrg_esdgr), (n.d.). http://ec.europa.eu/eurostat/cache/metadata/en/nrg_esdgr_esms.htm.

[12] Eurostat, Heating degree-days by NUTS 2 regions - annual data, (n.d.). http://www.eea.europa.eu/data-and-maps/data/external/heating-degree-days-annual-data.

[13] Eurostat, Electricity and natural gas price statistics, (n.d.). http://ec.europa.eu/eurostat/statistics-explained/index.php/Energy_price_statistics.

[14] S. Fortuna, P. Neri, F. Peron, Social and energy redevelopment of an old building, in: Bozen, 2013.

[15] G. Ruggieri, G. Dotelli, P. Melià, S. Sabbadini, Life cycle assessment of refurbishment strategies for historic buildings, in: W. Swan, P. Brown (Eds.), Retrofitting the Built Environment, John Wiley & Sons, 2013: pp. 113–127. http://onlinelibrary.wiley.com/doi/10.1002/9781118273463.ch9/summary (accessed October 10, 2016).

[16] EN ISO 14040:2000 - Environmental management - life cycle assessment - principles and framework, 2000.

[17] R. Frischknecht, N. Jungbluth, H. Althaus, C. Bauer, G. Doka, R. Dones, Implementation of life cycle impact assessment methods. Final report ecoinvent 2007, (2003).
[18] R. Frischknecht, N. Jungbluth, H. Althaus, G. Doka, R. Dones, R. Hischier, S. Hellweg, S. Humbert, M. Margni, T. Nemecek, M. Spielmann, Implementation of Life Cycle Impact Assessment Methods: Data v2.0. ecoinvent report No. 3, (2007).
[19] M. Goedkoop, M. Oele, A. De schryver, M. Vieira, 2008 SimaPro Data Base Manual, (2008).
[20] ISO 11855:2012 - Building environment design -- Design, dimensioning, installation and control of embedded radiant heating and cooling systems, 2012.
[21] D.C. Meeker, Finite Element Method Magnetics, 2012. www.femm.info.
[22] CSC-IT, ELMER, 2015. csc.fi/web/elmer.
[23] Comsol Multiphysics Version 4, 2011. www.comsol.com.

8 CONCLUSIONS

Buildings are currently a key issue for the worldwide research and policymaking, and this trend will undoubtedly last for the next decades, reinforced by the need of taking concrete actions against global warming. As buildings account for an important share of the overall energy consumption, it is of paramount importance to accurately quantify their impact and identify the sources of energy losses.

This work proposed and verified several technical solutions to the study of buildings that could have a positive influence on the field, both in an immediate and in a long-term phase. The methods are based on infrared thermography, that was already well known as a tool for building inspection. This work described novel thermography-based devices (aIRview and IRpano) that are aimed to extend and improve the traditional thermographic survey of buildings. One main advantage is the automation of the scan, that increases the reliability and completeness of the survey. The automation allows also the performance of long-term surveys, easing the practical realization of a time-lapsed data acquisition. This opens new possibilities for the investigation of slow physical phenomena, such as the ones related to massive walls or to the detection of moisture into wall structure.

Another distinctive feature is the possibility to obtain not only a surface temperature distribution but also the measurement of different microclimatic parameters (e.g. air temperature, air velocity, relative humidity) with a single measuring device. The cases studies reported in Chapter 5 highlight these results in the context of cultural heritage surveys, that are chosen as a particularly challenging reference case, but could be flawlessly extended to a wide range of edifices. In these way also the advances in thermal image analysis described in Chapter 4, that are tested on works of art, are ready to be extended in the next future to the study of mechanical and aerospace components, increasing the reliability of the nondestructive testing procedures.

This work tried also to enhance the already good possibilities of infrared thermography in the survey of the building envelope. New methods for the investigation of thermal bridges, thermal transmittance, and dynamic behavior of structure tackled this issues from a different viewpoint with respect to other available methods. The promising results described in Chapter 6 are a good base for a future work that should apply the methods on different test cases, in order to have a wide comparison with the standard

techniques. For all the proposed methods, a great attention was taken to the need of making new techniques feasible for on-site surveys, as this is a future trend that should be taken into account.

This work underlined also the importance of simulation tools during the design phase of building retrofit. The use of numerical models and databases has an extremely positive impact on the whole construction process, as shown in Chapter 7. The simulation accuracy is enhanced when the modeling is connected to the real data coming from surveys and the perspective is the continuous integration of mathematical model and survey data, to allow a tuning of the models that is necessary and would be impossible in other ways. This is strictly linked to one of the key challenges of the next years in the construction sector, that is the reduction of the gap between the theoretical and the real performances of buildings. This work showed how this issue could be solved from two standpoints: improving the on-site diagnostic methods and the simulation tools.